6° Brazilian Conference on Dynamics, Control and Their Applications

May 21-25, 2007
UNESP – Campus de São José do Rio Preto, SP, Brazil

Dincon'2007

FRACTIONAL ORDER DYNAMICAL SYSTEMS AND ITS APPLICATIONS

J. A. Tenreiro Machado[1], *Ramiro S. Barbosa*[1], *Isabel S. Jesus*[1], *Manuel F. Silva*[1], *Lino B. Figueiredo*[1]
Cecília M. Reis[1], *Maria G. Marcos*[1], *Luís M. Afonso*[1], *Alexandra F. Galhano*[1], *Fernando B. Duarte*[2]
Miguel L. Lima[2], *Eduardo S. Pires*[3], *Nuno M. Fonseca Ferreira*[4]

[1] Institute of Engineering of Porto, Porto, Portugal, {jtm,rsb,isj,mss,lbf,cmr,amf,mgm,lma}@isep.ipp.pt
[2] School of Technology of Viseu, Viseu, Portugal, fduarte@mat.estv.ipv.pt,lima@mail.estv.ipv.pt
[3] University of Trás-os-Montes and Alto Douro, Vila Real, Portugal, epires@marao.utad.pt
[4] Institute of Engineering of Coimbra, Coimbra, Portugal, nunomig@isec.pt

Abstract: This article illustrates several applications of fractional calculus (FC) in science and engineering. It has been recognized the advantageous use of this mathematical tool in the modeling and control of many dynamical systems. In this perspective, this paper investigates the use of FC in the following fields:

- Controller tuning;
- Electrical systems;
- Traffic systems;
- Digital circuit synthesis;
- Evolutionary computing;
- Redundant robots;
- Legged robots;
- Robotic manipulators;
- Nonlinear friction;
- Financial modeling.

Keywords: Fractional calculus, modeling, dynamics.

1. INTRODUCTION

In recent years fractional calculus (FC) has been a fruitful field of research in science and engineering [1-6]. In fact, many scientific areas are currently paying attention to the FC concepts and we can refer its adoption in viscoelasticity and damping, diffusion and wave propagation, electromagnetism, chaos and fractals, heat transfer, biology, electronics, signal processing, robotics, system identification, traffic systems, genetic algorithms, percolation, modeling and identification, telecommunications, chemistry, irreversibility, physics, control systems, economy and finance.

The FC deals with derivatives and integrals to an arbitrary order (real or, even, complex order). The mathematical definition of a derivative/integral of fractional order has been the subject of several different approaches [1-3]. For example, the Laplace definition of a fractional derivative/integral of a signal $x(t)$ is:

$$D^{\alpha}x(t) = L^{-1}\left\{ s^{\alpha}X(s) - \sum_{k=0}^{n-1} s^{k} D^{\alpha-k-1}x(t)\Big|_{t=0} \right\} \tag{1}$$

where $n-1<\alpha\le n$, $\alpha>0$. The Grünwald-Letnikov definition is given by ($\alpha \in \Re$):

$$D^{\alpha}x(t) = \lim_{h\to 0}\left[\frac{1}{h^{\alpha}} \sum_{k=0}^{\infty} (-1)^{k} \binom{\alpha}{k} x(t-kh) \right] \tag{2a}$$

$$\binom{\alpha}{k} = \frac{\Gamma(\alpha+1)}{\Gamma(k+1)\Gamma(\alpha-k+1)} \tag{2b}$$

where Γ is the Gamma function and h is the time increment. Expression (2) shows that fractional-order operators are "global" operators having a memory of all past events, making them adequate for modeling memory effects in most materials and systems.

Bearing these ideas in mind, sections 2-15 present several applications of FC in science and engineering. In section 16 we draw the main conclusions.

2. TUNING OF PID CONTROLLERS USING FRACTIONAL CALCULUS CONCEPTS

The PID controllers are the most commonly used control algorithms in industry. Among the various existent schemes for tuning PID controllers, the Ziegler-Nichols (Z-N) method is the most popular and is still extensively used for the determination of the PID parameters. It is well known that the compensated systems, with controllers tuned by this method, have generally a step response with a high percent overshoot. Moreover, the Z-N heuristics are only suitable for plants with monotonic step response.

In this section we study a novel methodology for tuning PID controllers such that the response of the compensated system has an almost constant overshoot defined by a prescribed value. The proposed method is based on the minimization of the integral of square error (ISE) between the step responses of a unit feedback control system, whose open-loop transfer function $L(s)$ is given by a fractional-order integrator and that of the PID compensated system [7].

Figure 1 illustrates the fractional-order control system that will be used as reference model for the tuning of PID controllers. The open-loop transfer function $L(s)$ is defined as ($\alpha \in \Re^{+}$):

$$L(s) = \left(\omega_c / s \right)^{\alpha} \tag{3}$$

where ω_c is the gain crossover frequency, that is, $|L(j\omega_c)| = 1$. The parameter α is the slope of the magnitude curve, on a log-log scale, and may assume integer as well noninteger values. In this study we consider $1 < \alpha < 2$, such that the output response may have a fractional oscillation (similar to an underdamped second-order system). This transfer function is also known as the Bode's ideal loop transfer function since Bode studies on the design of feedback amplifiers in the 1940's [8].

The Bode diagrams of amplitude and phase of $L(s)$ are illustrated in Fig. 2. The amplitude curve is a straight line of constant slope -20α dB/dec, and the phase curve is a horizontal line positioned at $-\alpha\pi/2$ rad. The Nyquist curve is simply the straight line through the origin, $\arg L(j\omega) = -\alpha\pi/2$ rad.

This choice of $L(s)$ gives a closed-loop system with the desirable property of being insensitive to gain changes. If the gain changes the crossover frequency ω_c will change but the phase margin of the system remains $PM = \pi(1 - \alpha/2)$ rad, independently of the value of the gain. This can be seen from the curves of amplitude and phase of Fig. 2.

The closed-loop transfer function of fractional-order control system of Fig. 1 is given by:

$$G(s) = \frac{L(s)}{1+L(s)} = \frac{1}{\left(s/\omega_c\right)^{\alpha}+1}, \quad 1<\alpha<2 \tag{4}$$

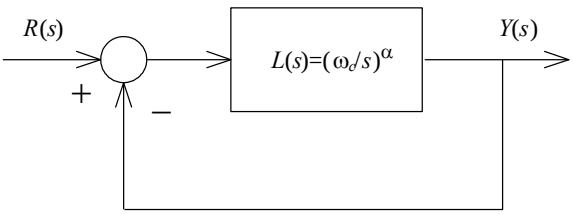

Fig. 1. Fractional-order control system with open-loop transfer function $L(s)$

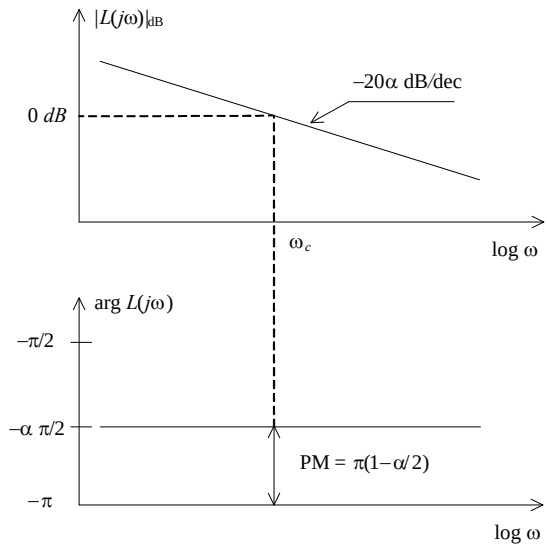

Fig. 2. Bode diagrams of amplitude and phase of $L(j\omega)$ for $1 < \alpha < 2$

The unit step response of $G(s)$ is given by the expression:

$$y_d(t) = L^{-1}\left\{\frac{1}{s}G(s)\right\} = L^{-1}\left\{\frac{\omega_c^{\alpha}}{s\left(s^{\alpha}+\omega_c^{\alpha}\right)}\right\}$$

$$= 1 - \sum_{n=0}^{\infty}\frac{\left[-(\omega_c t)^{\alpha}\right]^n}{\Gamma(1+\alpha n)} = 1 - E_{\alpha}\left[-(\omega_c t)^{\alpha}\right] \tag{5}$$

For the tuning of PID controllers we address the fractional-order transfer function (4) as the reference system [9]. With the order α and the crossover frequency ω_c we can establish the overshoot and the speed of the output response, respectively. For that purpose we consider the closed-loop system shown in Fig. 3, where $G_c(s)$ and $G_p(s)$ are the PID controller and the plant transfer functions, respectively.

The transfer function of the PID controller is:

$$G_c(s) = \frac{U(s)}{E(s)} = K\left(1+\frac{1}{T_i s}+T_d s\right) \tag{6}$$

where $E(s)$ is the error signal and $U(s)$ is the controller's output. The parameters K, T_i, and T_d are the proportional gain, the integral time constant and the derivative time constant of the controller, respectively.

The design of the PID controller will consist on the determination of the optimum PID set gains (K, T_i, T_d) that minimize J, the integral of the square error (ISE), defined as:

$$J = \int_0^{\infty}\left[y(t) - y_d(t)\right]^2 dt \tag{7}$$

where $y(t)$ is the step response of the closed-loop system with the PID controller (Fig. 3) and $y_d(t)$ is the desired step response of the fractional-order transfer function (4) given by expression (5).

To illustrate the effectiveness of proposed methodology we consider the third-order plant transfer function:

$$G_p(s) = \frac{K_p}{(s+1)^3} \tag{8}$$

with nominal gain $K_p = 1$.

Figure 4 shows the step responses and the Bode diagrams of phase of the closed-loop system with the PID for the transfer function $G_p(s)$ for gain variations around the nominal gain ($K_p = 1$) corresponding to $K_p = \{0.6, 0.8, 1.0, 1.2, 1.4\}$, that is, for a variation up to ±40% of its nominal value. The system was tuned for $\alpha = 3/2$ (PM = 45º), $\omega_c = 0.8$ rad/s. We verify that we get the same desired iso-damping property corresponding to the prescribed (α, ω_c)-values.

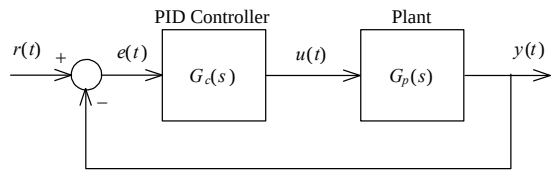

Fig. 3. Closed-loop control system with PID controller $G_c(s)$

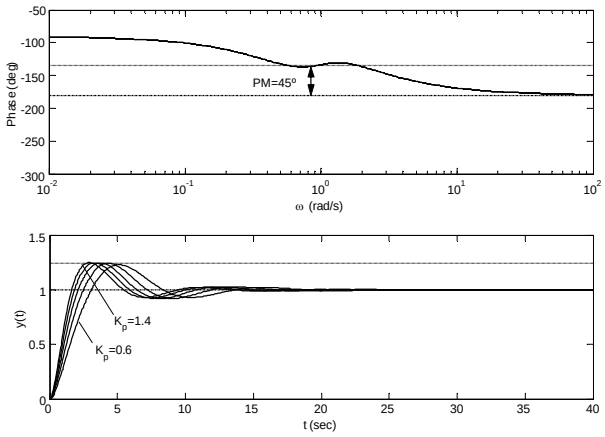

Fig. 4. Bode phase diagrams and step responses for the closed-loop system with a PID controller for $G_p(s)$. The PID parameters are $K = 1.9158$, $T_i = 1.1407$ and $T_d = 0.9040$

In fact, we observe that the step responses have an almost constant overshoot independently of the variation of the plant gain around the gain crossover frequency ω_c. Therefore, the proposed methodology is capable of producing closed-loop systems robust to gain variations and step responses exhibiting an iso-damping property. The proposed method was tested on several cases studies revealing good results. It was also compared with other tuning methods showing comparable or superior results [9].

3. FRACTIONAL PD$^{\alpha}$ CONTROL OF A HEXAPOD ROBOT

Walking machines allow locomotion in terrain inaccessible to other type of vehicles, since they do not need a continuous support surface, but at the cost of higher requirements for leg coordination and control. For these robots, joint level control is usually implemented through a PID like scheme with position feedback. Recently, the application of the theory of FC to robotics revealed promising aspects for future developments [10]. With these facts in mind, this study compares different Fractional PD$^{\alpha}$ robot controller tuning, applied to the joint control of a walking system (Fig. 5) with $n = 6$ legs, equally distributed along both sides of the robot body, having each three rotational joints (*i.e.*, $j = \{1, 2, 3\} \equiv \{\text{hip, knee, ankle}\}$) [11].

During this study leg joint $j = 3$ can be either mechanical actuated or motor actuated (Fig. 5). For the mechanical actuated case, we suppose that there is a rotational pre-tensioned spring-dashpot system connecting leg links L_{i2} and L_{i3}. This mechanical impedance maintains the angle between the two links while imposing a joint torque [11].

Figure 5 presents the dynamic model for the hexapod body and foot-ground interaction. It is considered robot body compliance because walking animals have a spine that allows supporting the locomotion with improved stability. The robot body is divided in n identical segments (each with mass $M_b n^{-1}$) and a linear spring-damper system (with parameters defined so that the body behaviour is similar to the one expected to occur on an animal) is adopted to implement the intra-body compliance [11]. The contact of the ith robot feet with the ground is modelled through a non-linear system [12], being the values for the parameters based on the studies of soil mechanics [12].

The general control architecture of the hexapod robot is presented in Fig. 6 [13]. In this study we evaluate the effect of different PD$^{\alpha}$, $\alpha \in \Re$, controller implementations for $G_{c1}(s)$, while G_{c2} is a proportional controller with gain $Kp_j = 0.9$ ($j = 1, 2, 3$). For the PD$^{\alpha}$ algorithm, implemented through a discrete-time 4th-order Padé approximation (a_{ij}, $b_{ij} \in \Re$, $j = 1, 2, 3$), we have:

$$G_{c1j}(z) \approx Kp_j + K\alpha_j \sum_{i=0}^{i=u} a_{ij}\, z^{-i} \Big/ \sum_{i=0}^{i=u} b_{ij}\, z^{-i} \qquad (9)$$

where Kp_j and $K\alpha_j$ are the proportional and derivative gains, respectively, and α_j is the fractional order, for joint j. Therefore, the classical PD^1 algorithm occurs when the fractional order $\alpha_j = 1.0$.

It is analysed the system performance of the different PD$^{\alpha}$ tuning, during a periodic wave gait at a constant forward velocity V_F, for two cases: two leg joints are motor actuated and the ankle joint is mechanical actuated and the three leg joints are fully motor actuated [11].

The analysis is based on the formulation of two indices measuring the mean absolute density of energy per traveled distance (E_{av}) and the hip trajectory errors (ε_{xyH}) during walking, according to:

$$E_{av} = \frac{1}{d}\sum_{i=1}^{n}\sum_{j=1}^{m}\int_0^T \left|\boldsymbol{\tau}_{ij}(t)\dot{\boldsymbol{\theta}}_{ij}(t)\right| dt \quad \left[\mathrm{Jm}^{-1}\right] \qquad (10a)$$

$$\varepsilon_{xyH} = \sum_{i=1}^{n}\sqrt{\frac{1}{N_s}\sum_{k=1}^{N_s}\left(\Delta_{ixH}{}^2 + \Delta_{iyH}{}^2\right)} \quad [\mathrm{m}]$$
$$\Delta_{ixH} = x_{iHd}(k) - x_{iH}(k),\ \Delta_{iyH} = y_{iHd}(k) - y_{iH}(k) \qquad (10b)$$

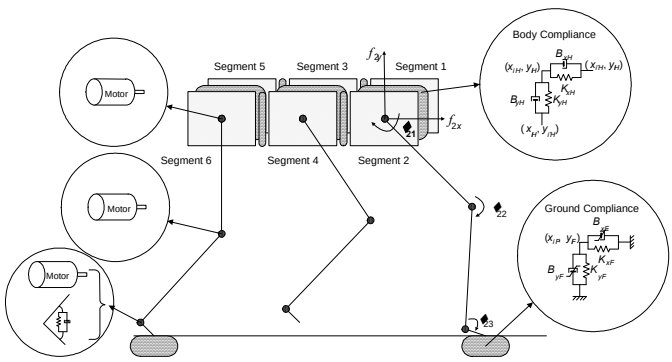

Fig. 5. Model of the robot body and foot-ground interaction

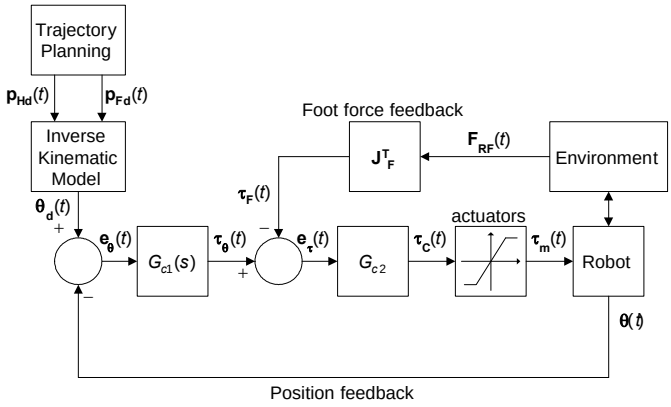

Fig. 6. Hexapod robot control architecture

To tune the different controller implementations we adopt a systematic method, testing and evaluating several possible combinations of parameters, for all controller implementations. Therefore, we adopt the $G_{c1}(s)$ parameters that establish a compromise in what concerns the simultaneous minimisation of E_{av} and ε_{xyH}. Moreover, it is assumed high performance joint actuators, with a maximum actuator torque of $\tau_{ijMax} = 400$ Nm, and the desired angle between the foot and the ground (assumed horizontal) is made $\theta_{i3hd} = -15^{\circ}$. We tune the PD$^{\alpha}$ joint controllers for different values of the fractional order α_j while making $\alpha_1 = \alpha_2 = \alpha_3$.

We start by considering that leg joints 1 and 2 are motor actuated and joint 3 is mechanical actuated. For this case we tune the FO PD$^{\alpha}$ joint controllers for different values of the fractional order α_j in the interval $-0.9 < \alpha_j < +0.9$ and $\alpha_j \neq 0.0$. Afterwards, we consider that joint 3 is also motor actuated, and we repeat the controller tuning procedure versus α_j.

For the first situation under study, we verify that the value of $\alpha_j = 0.6$ (Fig. 7), with the gains of the PD$^{\alpha}$ controller being $K_{p1} = 2500$, $K_{\alpha 1} = 800$, $K_{p2} = 300$, $K_{\alpha 2} = 100$ and the parameters of the mechanical spring-dashpot system for the ankle actuation being $K_3 = 1$, $B_3 = 2$, presents the best compromise situation in what concerns the simultaneous minimisation of ε_{xyH} and E_{av}.

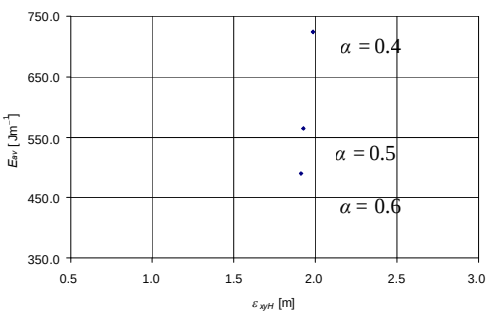

Fig. 7. Locus of E_{av} *vs.* ε_{xyH} for the different values of α in the $G_{c1}(s)$ tuning, when establishing a compromise between the minimisation of E_{av} and ε_{xyH}, with $G_{c2} = 0.9$, joints 1 and 2 motor actuated and joint 3 mechanical actuated

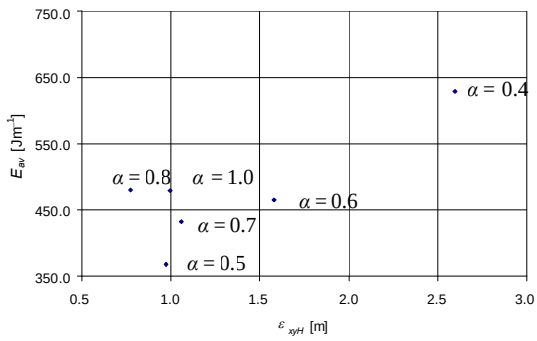

Fig. 8. Locus of E_{av} *vs.* ε_{xyH} for the different values of α in the $G_{c1}(s)$ tuning, when establishing a compromise between the minimisation of E_{av} and ε_{xyH}, with $G_{c2} = 0.9$ and all joints motor actuated

Regarding the case when all joints are motor actuated, Fig. 8 presents the best controller tuning for different values of α_j. The experiments reveal the superior performance of the PD$^{\alpha}$ controller for $\alpha_j \approx 0.5$, with $K_{p1} = 15000$, $K_{\alpha 1} = 7200$, $K_{p2} = 1000$, $K_{\alpha 2} = 800$ and $K_{p3} = 150$, $K_{\alpha 3} = 240$.

For values of $\alpha_j = \{0.1, 0.2, 0.3, 0.4\}$, the results are very poor and for $-0.9 < \alpha_j < -0.1$ and $\alpha_j = 0.9$, the hexapod locomotion is unstable. Furthermore, we conclude that the best case corresponds to all leg joints being motor actuated.

In conclusion, the experiments reveal the superior performance of the FO controller for $\alpha_j \approx 0.5$ and a robot with all motor actuated joints, as can be concluded analysing the curves for the joint actuation torques τ_{1jm} (Fig. 9) and for the hip trajectory tracking errors Δ_{1xH} and Δ_{1yH} (Fig. 10).

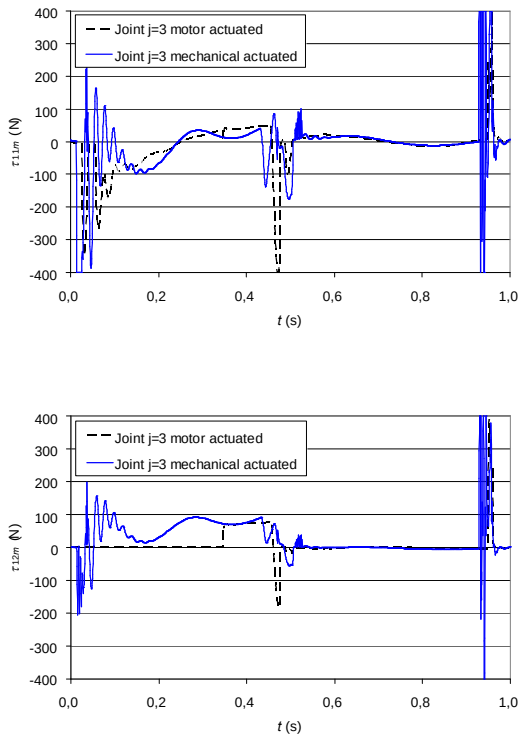

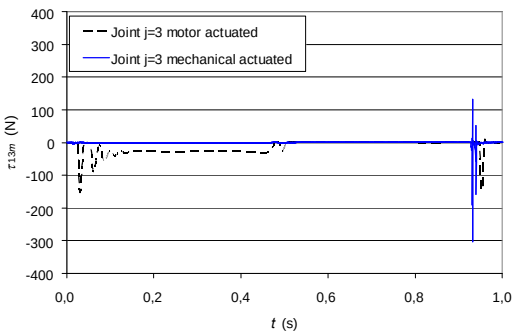

Fig. 9. Plots of τ_{1jm} *vs.* t, with joints 1 and 2 motor actuated and joint 3 mechanical actuated and all joints motor actuated, for $\alpha_j = 0.5$

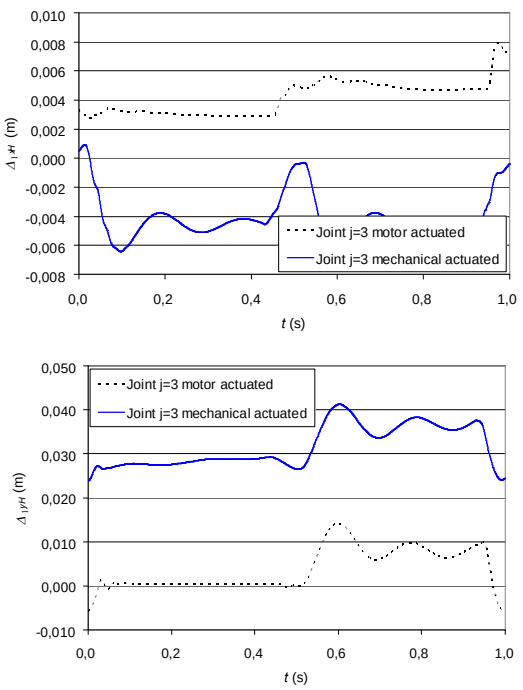

Fig. 10. Plots of Δ_{1xH} and Δ_{1yH} *vs.* t, with joints 1 and 2 motor actuated and joint 3 mechanical actuated and all joints motor actuated, for $\alpha_j = 0.5$

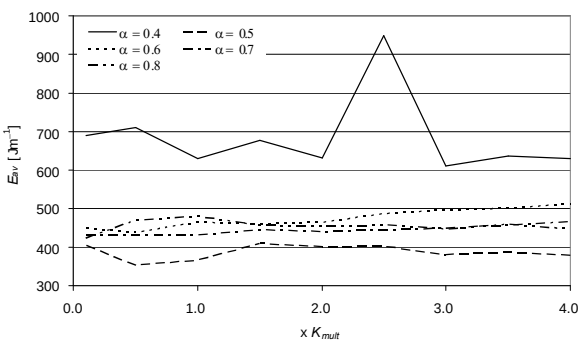

Fig. 11. Performance index E_{av} *vs.* K_{mult} for the different $G_{c1}(s)$ FO PD$^{\alpha}$ controller tuning with all joints motor actuated

Since the objective of the walking robots is to walk in natural terrains, in the sequel it is examined how the different controller tunings behave under different ground properties, considering that all joints are motor actuated. For this case, and considering the previously tuning controller parameters, the values of $\{K_{xF}, B_{xF}, K_{yF}, B_{yF}\}$ are varied simultaneously through a multiplying factor K_{mult} that is varied in the range [0.1, 4.0]. This variation for the ground model parameters allows the simulation of the ground behaviour for growing stiffness, from peat to gravel [12].

The performance measure E_{av} *versus* the multiplying factor of the ground parameters K_{mult} is presented on Fig. 11. Analysing the system performance from the viewpoint of the index E_{av}, it is possible to conclude that the best FO PD$^{\alpha}$ implementation occurs for the fractional order $\alpha_j = 0.5$. Moreover, it is clear that the performances of the different controller implementations are almost constant on all range of the ground parameters, with the exception of the fractional order $\alpha_j = 0.4$. For this case, E_{av} presents a significant variation with K_{mult}. Therefore, we conclude that the controller responses are quite similar, meaning that these algorithms are robust to variations of the ground characteristics [13].

4. SIMULATION AND DYNAMICAL ANALYSIS OF FREEWAY TRAFFIC SYSTEMS

4.1. Simulation Package

In order to study the dynamics of traffic systems it was developed the Simulator of Intelligent Transportation Systems (*SITS*). *SITS* is a software tool based on a microscopic simulation approach, which reproduces real traffic conditions in an urban or non-urban network. The program provides a detailed modelling of the traffic network, distinguishing between different types of vehicles and drivers and considering a wide range of network geometries. *SITS* uses a flexible structure that allows the integration of simulation facilities for any of the *ITS* related areas [14]. The overall model structure is represented on Fig. 12.

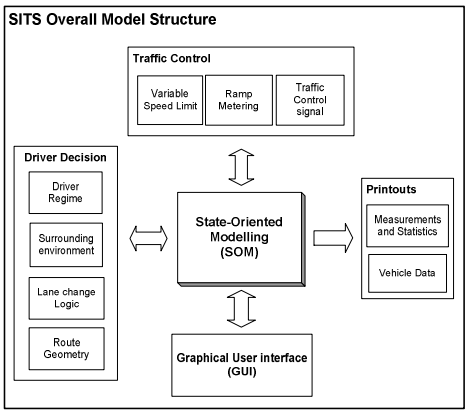

Fig. 12. SITS overall model structure

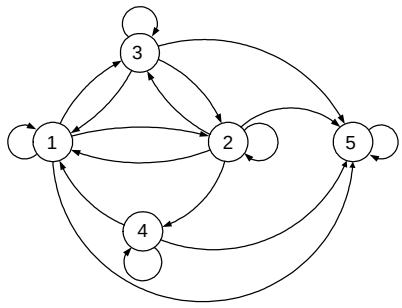

Fig. 13. SITS state diagram: 1-aceleration, 2-braking, 3-cruise speed, 4-stopped, 5-collision

SITS models each vehicle as a separate entity in the network according to the state diagram showing in Fig. 13. Therefore, are defined five states {1-aceleration, 2-braking, 3-cruise speed, 4-stopped, 5-collision} that represent the possible vehicle states in a traffic systems.

In this modelling structure, so called State-Oriented Modelling (*SOM*) [15], every single vehicle in the network has one possible state for each sampling period. The transition between each state depends on the driver behaviour model and its surrounding environment. Some transitions are not possible; for instance, it is not possible to move from state #4 (stopped) to state #2 (braking), although it is possible to move from state #2 to state #4.

Included on the most important elements of SITS are the network components, travel demand, and driving decisions. Network components include the road network geometry, vehicles and the traffic control. To each driver is assigned a set of attributes that describe the drivers behavior, including desired speed, and his profile (*e.g.*, from conservative to aggressive). Likewise, vehicles have their own specifications, including size and acceleration capabilities. Travel demand is simulated using origin destination matrices given as an input to the model.

At this stage of development the SITS implements different types of driver behaviour models, namely car following, free flow and lane changing logic [16].

4.2. Dynamical Analysis

In the dynamical analysis are applied tools of systems theory. In this line of thought, a set of simulation experiments are developed in order to estimate the influence of the vehicle speed $v(t;x)$, the road length l and the number of lanes n_l in the traffic flow $\phi(t;x)$ at time t and road coordinate x. For a road with n_l lanes the Transfer Function (*TF*) between the flow measured by two sensors is calculated by the expression:

$$G_{r,k}(s; x_j, x_i) = \Phi_r(s;x_j)/\Phi_k(s;x_i) \tag{11}$$

where k, $r = 1,2,\ldots, n_l$ define the lane number and, x_i and x_j represent the road coordinates ($0 \le x_i \le x_j \le l$), respectively
It should be noted that traffic flow is a stochastic system but, in the sequel, it is shown that the Laplace transform can be used to analyse the system dynamics.

The first group of experiments considers a one-lane road (*i.e.*, $k = r = 1$) with length $l = 1000$ m. Across the road are placed n_s sensors equally spaced. The first sensor is placed at the beginning of the road (*i.e.*, at $x_i = 0$) and the last sensor at the end (*i.e.*, at $x_j = l$). Therefore, we calculate the *TF* between two traffic flows at the beginning and the end of the road such that, $\phi_1(t;0) \in [1, 8]$ vehicles s^{-1} for a vehicle speed $v_1(t;0) \in [30, 70]$ km h^{-1}, that is, for $v_1(t;0) \in [v_{av} - \Delta v, v_{av} + \Delta v]$, where $v_{av} = 50$ km h^{-1} is the average vehicle speed and $\Delta v = 20$ km h^{-1} is the maximum speed variation. These values are generated according to a uniform probability distribution function.

The results obtained of the polar plot for the *TF* $G_{1,1}(s;1000,0) = \Phi_1(s;1000)/\Phi_1(s;0)$ between the traffic flow at the beginning and end of the one-lane road is distinct from those usual in systems theory revealing a large variability, as revealed by Fig. 14. Moreover, due to the stochastic nature of the phenomena involved different experiments using the same input range parameters result in different *TF*s.

In fact traffic flow is a complex system but it was shown [17] that, by embedding statistics and Fourier transform (leading to the concept of Statistical Transfer Function (*STF*)), we could analyse the system dynamics in the perspective of systems theory [18].

To illustrate the proposed modelling concept (*STF*), the simulation was repeated for a sample of $n = 2000$ and it was observed the existence of a convergence of the *STF*, $T_{1,1}(s;1000,0)$, as show in Fig. 15, for a one-lane road with length $l = 1000$ m $\phi_1(t;0) \in [1, 8]$ vehicles s^{-1} and $v_1(t;0) \in [30, 70]$ km h^{-1}.

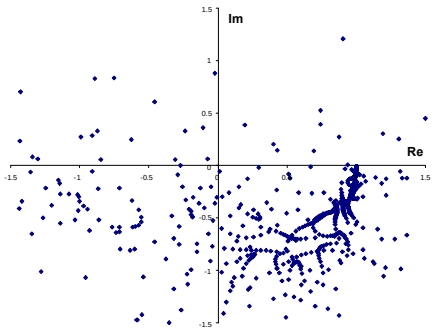

Fig. 14. The Polar Diagram of *TF* $G_{1,1}(s;1000,0)$ with $\phi_1(t;0) \in [1, 8]$ vehicles s^{-1} and $v_1(t;0) \in [30, 70]$ km h^{-1} ($v_{av} = 50$ km h^{-1}, $\Delta v = 20$ km h^{-1}, $l = 1000$ m and $n_l = 1$)

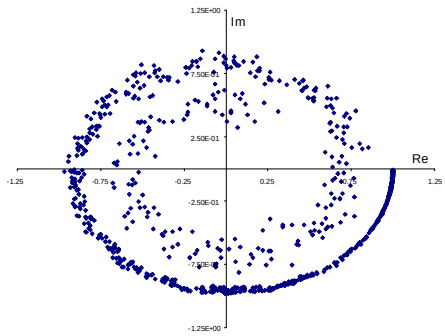

Fig. 15. The *STF* $T_{1,1}(s;1000,0)$ for $n = 2000$ experiments with $\phi_1(t;0) \in [1, 8]$ vehicles s^{-1} and $v_1(t;0) \in [30, 70]$ km h^{-1}($v_{av} = 50$ km h^{-1}, $\Delta v = 20$ km h^{-1}, $l = 1000$ m and $n_l = 1$)

The chart has characteristics similar to those of a low-pass filter with time delay, common in systems involving transport phenomena. Nevertheless, in our case we need to include the capability of adjusting the description to the continuous variation of the system working conditions. This requirement precludes the adoption of the usual integer-order low-pass filter and points out the need for the adoption of a fractional-order *TF*. Therefore, in this case we adopt a fractional-order system with time delay [1, 3].

$$T_{1,1}(s;1000,0) = \frac{k_B \; e^{-\tau s}}{\left(\frac{s}{p}+1\right)^{\alpha}} \qquad (12)$$

With this description we get not only a superior adjustment of the numerical data, impossible with the discrete steps in the case of integer-order *TF*, but also a mathematical tool more adapted to the dynamical phenomena involved. For fitting (12) with the numerical data it is adopted a two-step method based on the minimization of the quadratic error. In the first phase (k_B, p, α) are obtained through error amplitude minimization of the Bode diagram. Once established (k_B, p, α), in a second phase, τ is estimated through the error minimization in the Polar diagram.

For the numerical parameters of Fig. 15 we get $k_B = 1.0$, $\tau = 96.0$ sec, $p = 0.07$ and $\alpha = 1.5$. The parameters (τ, p, α) vary with the average speed v_{av} and its range of variation Δv, the road length l and the input vehicle flow ϕ_1. For example, Fig. 16 shows (τ, p, α) versus Δv for $v_{av} = 50$ km h^{-1}.

It is interesting to note that $(\tau, p) \to (\infty, 0)$, when $\Delta v \to v_{av}$, and $(\tau, p) \to (l\, v_{av}^{-1}, \infty)$, when $\Delta v \to 0$. These results are consistent with our experience that suggests a pure transport delay $T(s) \approx e^{-\tau s}$ ($\tau = l\, v_{av}^{-1}$), $\Delta v \to 0$ and $T(s) \approx 0$, when $\Delta v \to v_{av}$ (because of the existence of a blocking cars, with zero speed, on the road).

In a second group of experiments are analyzed the characteristics of the *STF* matrix for roads with two lanes considering identical traffic conditions (*i.e.*, $\phi_k(t;0) \in [0.12, 1]$ vehicles s^{-1}, $k = 1,2$, $l = 1000$, $\Delta v = 20$ km h^{-1}). Fig. 17 depicts the amplitude Bode diagram of $T_{1,1}(s;1000,0)$ and $T_{1,2}(s;1000,0)$ for $v_{av} = 50$ km h^{-1} (*i.e.*, $v_k(t;0) \in [30, 70]$ km h^{-1}).

We verify that $T_{1,1}(s;1000,0) \approx T_{2,2}(s;1000,0)$ and $T_{1,2}(s;1000,0) \approx T_{2,1}(s;1000,0)$. This property occurs because SITS uses lane change logic where, after the overtaking, the vehicle tries to return to the previous lane. Therefore, lanes 1 and 2 have the same characteristics leading to identical *STF* [19].

The *STF* parameter dependence is similar to the one-lane case represented previously. Fig. 18a) and 18b) show the variation of parameters (k_B, p, α) for $T_{1,1}(s;1000,0)$ *versus* v_{av} (with $\Delta v = 20$ km h^{-1}) and Δv (with $v_{av} = 50$ km h^{-1}), respectively, for $n_l = 2$.

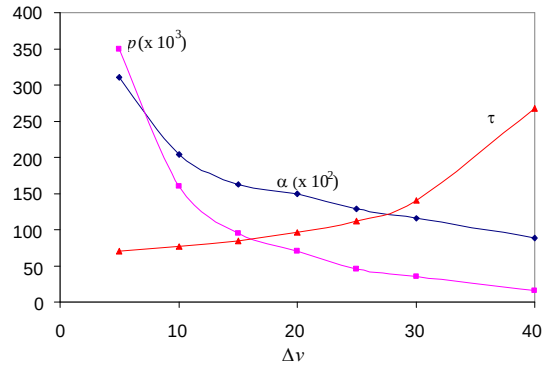

Fig. 16. Time delay τ, pole p and fractional order α *versus* Δv for an average vehicle speed $v_{av} = 50$ km h^{-1}, $n_l = 1$, $l = 1000$ m and $\phi_1(t;0) \in [1, 8]$ vehicles s^{-1}

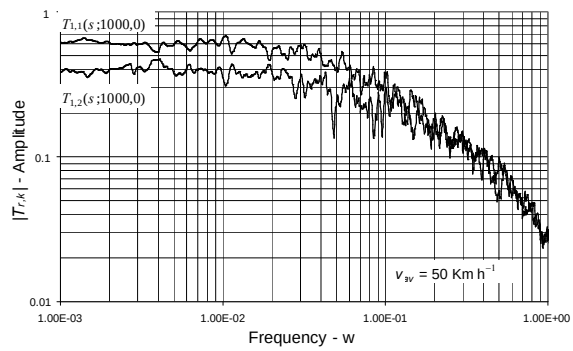

Fig. 17. Amplitude Bode diagram of $T_{r,k}(s;1000,0)$ for $v_{av} = 50$ km h^{-1}, $n_l = 2$, $l = 1000$ m, $\phi_k(t;0) \in [0.12, 1]$ vehicles s^{-1}, $\Delta v = 20$ km h^{-1}, $k = 1,2$

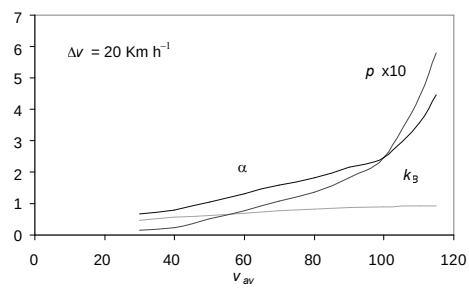

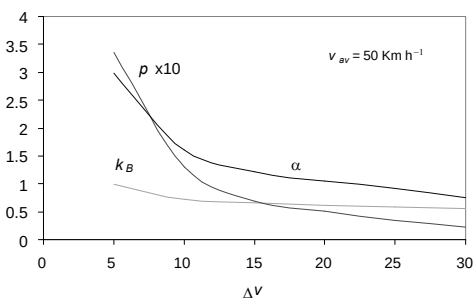

Fig. 18. Parameters (k_B, p, α) *versus* a) v_{av} and b) Δv, for $T_{1,1}(s;1000,0)$ with $n_l = 2$, $l = 1000$ m and $\phi_1(t;0) \in [0.12, 1]$ vehicles s^{-1}

We conclude that:

i. The time delay τ is independent of the number of lanes n_l (considering the same input flow $\phi_1(t;0)$).

ii. For a fixed set of parameters we have for each *STF* gain × bandwidth ≈ constant.

iii. For each row of the transfer matrix, the sum of the *STF* gains is the unit.

iv. The gains and the poles of the diagonal elements of the *STF* matrix are similar. The gain of the non-diagonal elements, that represent dynamic coupling between the lanes, are lower (due to *iii*), but the corresponding pole are higher (due to *ii*).

v. The fractional order α increases with v_{av}. Nevertheless, the higher the number of lanes the lower the low-pass filter effect, that is, the smaller the value of α.

5. FRACTIONAL DYNAMICS IN THE TRAJECTORY CONTROL OF REDUNDANT MANIPULATORS

A kinematically redundant manipulator is a robotic arm possessing more degrees of freedom (*dof*) than those required to establish an arbitrary position and orientation of the gripper. Redundant manipulators offer several potential advantages over non-redundant arms. In a workspace with obstacles, the extra degrees of freedom can be used to move around or between obstacles and thereby to manipulate in situations that otherwise would be inaccessible [20-23].

When a manipulator is redundant, it is anticipated that the inverse kinematics admits an infinite number of solutions. This implies that, for a given location of the manipulator's gripper, it is possible to induce a self-motion of the structure without changing the location of the end effecter. Therefore, the arm can be reconfigured to find better postures for an assigned set of task requirements.

Several kinematic techniques for redundant manipulators control the gripper through the rates at which the joints are driven, using the pseudoinverse of the Jacobian [22, 25]. Nevertheless, these algorithms lead to a kind of chaotic motion with unpredictable arm configurations.

Having these ideas in mind, sub-section 5.1 introduces the fundamental issues for the kinematics of redundant manipulators. Based on these concepts, sub-section 5.2 presents the trajectory control of a three *dof* robot. The results reveal a chaotic behavior that is further analyzed in sub-section 5.3.

5.1. Kinematics of redundant manipulators

A kinematically redundant manipulator is a robotic arm possessing more *dof* than those required to establish an arbitrary position and orientation of the gripper. In Fig. 19 is depicted a planar manipulator with $k \in \aleph$ rotational (R) joints that is redundant for $k > 2$. When a manipulator is redundant it is anticipated that the inverse kinematics admits an infinite number of solutions. This implies that, for a given location of the manipulator's gripper, it is possible to induce a self-motion of the structure without changing the location of the gripper. Therefore, redundant manipulators can be reconfigured to find better postures for an assigned set of task requirements but, on the other hand, have a more complex structure requiring adequate control algorithms.

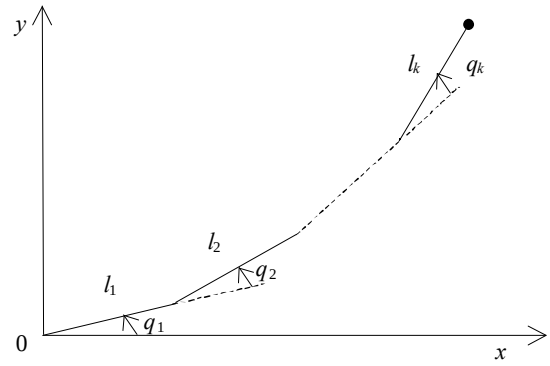

Fig. 19. A planar redundant planar manipulator with *k* rotational joints

We consider a manipulator with n degrees of freedom whose joint variables are denoted by $\mathbf{q} = [q_1, q_2, ..., q_n]^T$. We assume that a class of tasks we are interested in can be described by m variables, $\mathbf{x} = [x_1, x_2, ..., x_m]^T$ ($m < n$) and that the relation between $\mathbf{q}$ and $\mathbf{x}$ is given by:

$$\mathbf{x} = f(\mathbf{q}) \tag{13}$$

where f is a function representing the direct kinematics.

Differentiating (13) with respect to time yields:

$$\dot{\mathbf{x}} = \mathbf{J}(\mathbf{q})\dot{\mathbf{q}} \tag{14}$$

where $\dot{\mathbf{x}} \in \Re^m$, $\dot{\mathbf{q}} \in \Re^n$ and $\mathbf{J}(\mathbf{q}) = \partial f(\mathbf{q}) / \partial \mathbf{q} \in \Re^{m \times n}$. Hence, it is possible to calculate a path $\mathbf{q}(t)$ in terms of a prescribed trajectory $\mathbf{x}(t)$ in the operational space. We assume that the following condition is satisfied:

$$\max \text{ rank } \{\mathbf{J}(\mathbf{q})\} = m \tag{15}$$

Failing to satisfy this condition usually means that the selection of manipulation variables is redundant and the number of these variables m can be reduced. When condition (14) is verified, we say that the degree of redundancy of the manipulator is $n-m$. If, for some $\mathbf{q}$ we have:

$$\text{rank } \{\mathbf{J}(\mathbf{q})\} < m \tag{16}$$

then the manipulator is in a singular state. This state is not desirable because, in this region of the trajectory, the manipulating ability is very limited.

Many approaches for solving redundancy [24, 27] are based on the inversion of equation (14). A solution in terms of the joint velocities is sought as:

$$\dot{\mathbf{q}} = \mathbf{J}^{\#}(\mathbf{q})\dot{\mathbf{x}} \tag{17}$$

where $\mathbf{J}^{\#}$ is one of the generalized inverses of the $\mathbf{J}$ [26-28]. It can be easily shown that a more general solution to equation (14) is given by:

$$\dot{\mathbf{q}} = \mathbf{J}^{+}(\mathbf{q})\dot{\mathbf{x}} + \left[\mathbf{I} - \mathbf{J}^{+}(\mathbf{q})\mathbf{J}(\mathbf{q})\right]\dot{\mathbf{q}}_0 \tag{18}$$

where $\mathbf{I}$ is the $n \times n$ identity matrix and $\dot{\mathbf{q}}_0 \in \Re^n$ is a $n \times 1$ arbitrary joint velocity vector and $\mathbf{J}^+$ is the pseudoinverse of the $\mathbf{J}$. The solution (18) is composed of two terms. The first term is relative to minimum norm joint velocities. The second term, the *homogeneous solution*, attempts to satisfy the additional constraints specified by $\dot{\mathbf{q}}_0$. Moreover, the matrix $\mathbf{I} - \mathbf{J}^+(\mathbf{q})\mathbf{J}(\mathbf{q})$ allows the projection of $\dot{\mathbf{q}}_0$ in the null space of $\mathbf{J}$. A direct consequence is that it is possible to generate internal motions that reconfigure the manipulator structure without changing the gripper position and orientation [27-30]. Another aspect revealed by the solution of (17) is that repetitive trajectories in the operational space do not lead to periodic trajectories in the joint space. This is an obstacle for the solution of many tasks because the resultant robot configurations have similarities with those of a chaotic system.

5.2. Robot trajectory control

The direct kinematics and the Jacobian of a 3-link planar manipulator with rotational joints (3*R* robot) has a simple recursive nature according with the expressions:

$$\begin{bmatrix} x \\ y \end{bmatrix} = \begin{bmatrix} l_1 C_1 + l_2 C_{12} + l_3 C_{123} \\ l_1 S_1 + l_2 S_{12} + l_3 S_{123} \end{bmatrix} \tag{19a}$$

$$\mathbf{J} = \begin{bmatrix} -l_1 S_1 - \ldots - l_3 S_{123} & \ldots & -l_3 S_{123} \\ l_1 C_1 + \ldots + l_3 C_{123} & \ldots & l_3 C_{123} \end{bmatrix} \tag{19b}$$

where l_i is the length of link i, $q_{i\ldots k} = q_i + \ldots + q_k$, $S_{i\ldots k} = Sin(q_{i\ldots k})$ and $C_{i\ldots k} = Cos(q_{i\ldots k})$.

During all the experiments it is considered $\Delta t = 10^{-3}$ sec, $L_{TOT} = l_1 + l_2 + l_3 = 3$ and $l_1 = l_2 = l_3$.

In the closed-loop pseudoinverse's method the joint positions can be computed through the time integration of the velocities according with the block diagram of the inverse kinematics algorithm depicted in Fig. 20 where $\mathbf{x}_{\mathbf{ref}}$ represents the vector of reference coordinates of the robot gripper in the operational space.

Based on equation (19) we analyze the kinematic performances of the 3*R*-robot when repeating a circular motion in the operational space with frequency $\omega_0 = 7.0$ rad sec^{-1}, centre at distance $r = [x^2+y^2]^{1/2}$ and radius ρ.

Figure 21 show the joint positions for the inverse kinematic algorithm (17) for r = {0.6, 2.0} and ρ = {0.3, 0.5}. We observe that:

- For r = 0.6 occur unpredictable motions with severe variations that lead to high joint transients [31]. Moreover, we verify a low frequency signal modulation that depends on the circle being executed.
- For r = 2.0 the motion is periodic with frequency identical to ω_0 = 7.0 rad sec^{-1}.

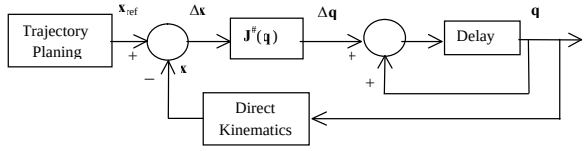

Fig. 20. Block diagram of the closed-loop inverse kinematics algorithm with the pseudoinverse

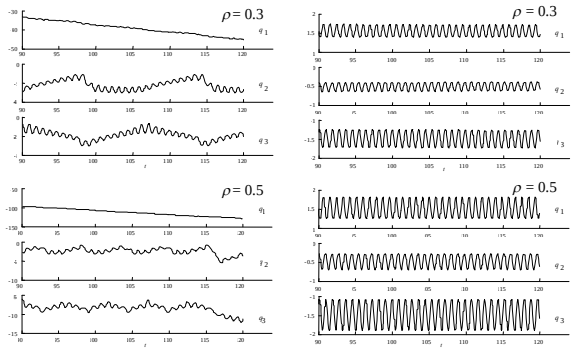

Fig. 21. The 3*R*-robot joint positions *versus* time using the pseudoinverse method for r = {0.6, 2.0} and ρ = {0.3, 0.5}

5.3. Analysis of the robot trajectories

In the previous section we verified that the pseudoinverse based algorithm leads to unpredictable arm configurations. In order to gain further insight into the pseudoinverse nature several distinct experiments are devised in the sequel during a time window of 300 cycles. Therefore, in a first set of experiments we calculate the Fourier transform of the 3*R*-robot joints velocities for a circular repetitive motion with frequency ω_0 = 7.0 rad sec^{-1}, radius ρ = {0.1, 0.3, 0.5, 0.7} and radial distances $r \in]0, L_{TOT} - \rho[$.

Figures 22-25 show $\left|F\{\dot{q}_2(t)\}\right|$ *versus* the frequency ratio ω_0/ω and the distance r where $F\{\ \}$ represents the Fourier operator. Is verified an interesting phenomenon induced by the gripper repetitive motion ω_0 because a large part of the energy is distributed along several sub-harmonics. These fractional order harmonics (*foh*) depend on r and ρ making a complex pattern with similarities with those revealed by chaotic systems. Furthermore, we observe the existence of several distinct regions depending on r.

For example, selecting in Fig. 25 several distinct cases, namely for r = {0.08, 0.30, 0.53, 1.10, 1.30, 2.00}, we have the different signal Fourier spectra clearly visible in Fig. 26. Joints 1 and 3 show similar velocity spectra.

In the author's best knowledge the *foh* are aspects of fractional dynamics [32-34], but a final and assertive conclusion about a physical interpretation is a matter still to be explored.

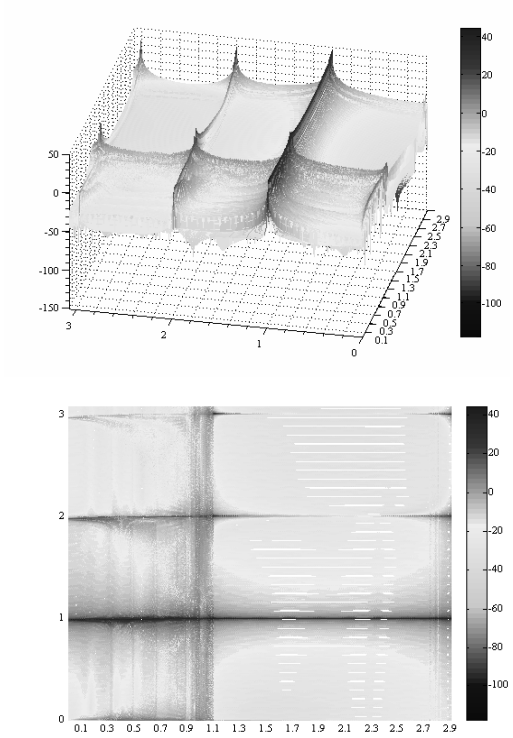

Fig. 22. $\left|F\left\{\dot{q}_2(t)\right\}\right|$ **of the 3*R*-robot during 300 cycles, vs *r* and ω/ω_0, for $\rho = 0.1$, $\omega_0 = 7.0$ rad** $\sec^{-1}$

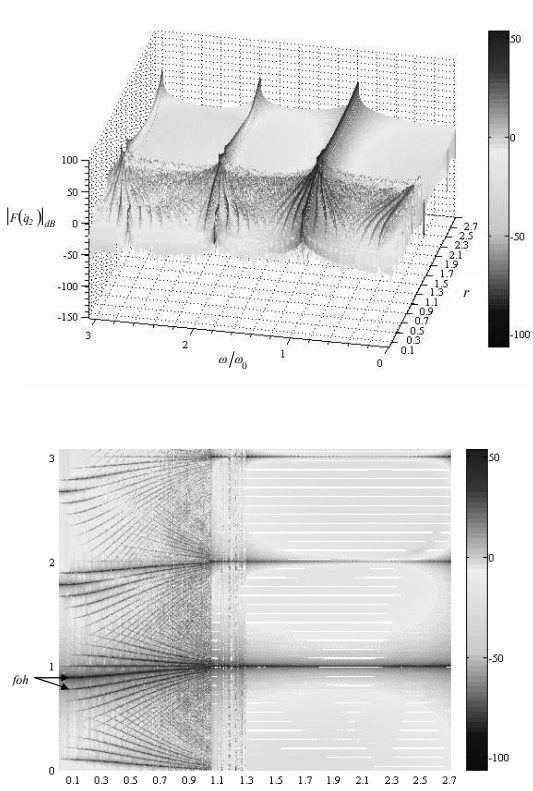

Fig. 23. $\left|F\left\{\dot{q}_2(t)\right\}\right|$ **of the 3*R*-robot during 300 cycles, vs *r* and ω/ω_0, for $\rho = 0.3$, $\omega_0 = 7.0$ rad** $\sec^{-1}$

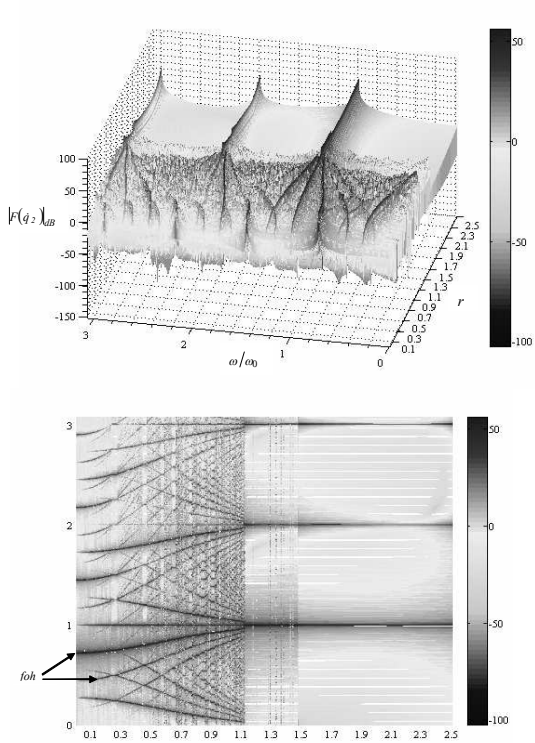

Fig. 24. $\left|F\left\{\dot{q}_2(t)\right\}\right|$ **of the 3*R*-robot during 300 cycles, vs *r* and ω/ω_0, for $\rho = 0.5$, $\omega_0 = 7.0$ rad** $\sec^{-1}$

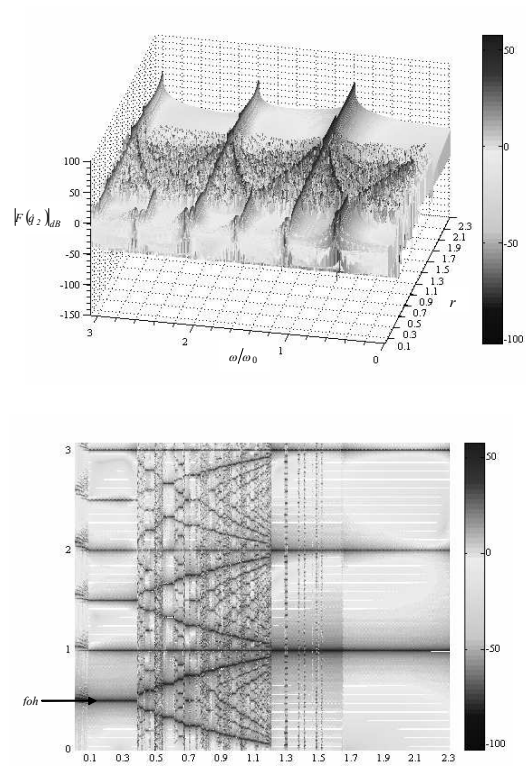

Fig. 25. $\left|F\left\{\dot{q}_2(t)\right\}\right|$ **of the 3*R*-robot during 300 cycles, vs *r* and ω/ω_0, for $\rho = 0.7$, $\omega_0 = 7.0$ rad** $\sec^{-1}$

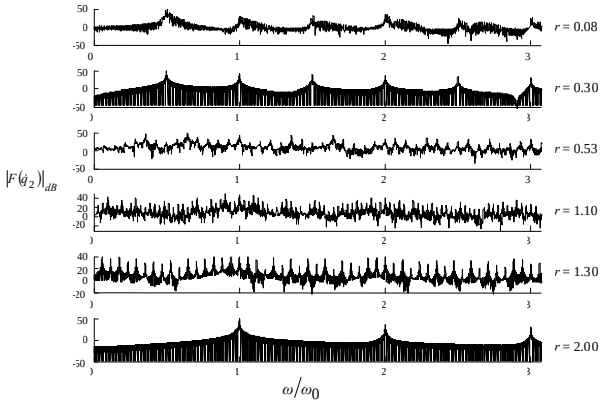

Fig. 26. $\left|F\{\dot{q}_2(t)\}\right|$ **of the 3*R*-robot during 300 cycles, vs the frequency ratio ω/ω_0, for r = {0.08, 0.30, 0.53, 1.10, 1.30, 2.00}, ρ = 0.7, ω_0 = 7.0 rad** $\sec^{-1}$

For joints velocities 1 and 3 the results are similar to the verified ones for joint velocity 2.

6. DESCRIBING FUNCTION OF SYSTEMS WITH NONLINEAR FRICTION

This section studies the describing function (DF) of systems composed of a mass subjected to nonlinear friction. The friction force is decomposed in three components namely, the viscous, the Coulomb and the static forces. The system dynamics is analyzed in the DF perspective and the reliability of the DF method is evaluated through the signal harmonic content.

6.1. Introduction

The phenomenon of vibration due to friction occurs in many branches of technology where it plays a very useful role. On the other hand, its occurrence is often undesirable, because it causes additional dynamic loads, as well as faulty operation of machines and devices. Despite many investigations that have been carried out so far, this phenomenon is not yet fully understood, mainly due to the considerable randomness and diversity of reasons underlying the energy dissipation involving the dynamic effects [35, 40, 41]. These nonlinear dynamic phenomena have been an active area of research but well established conclusions are still lacking.

In this section we investigate the dynamics of systems that contain nonlinear friction namely the Coulomb and the static forces in addition to the linear viscous, component. Bearing these ideas in mind, the section is organized as follows. Subsection 6.2 introduces the fundamental aspects of the describing function method. Subsection 6.3 studies the describing function of mechanical systems with nonlinear friction.

6.2. Fundamental concepts

In this subsection we present a summary of the DF method and its application on the prediction of limit cycles. The purpose is to analyze the controller performance in the presence of systems with nonlinear friction. Due to the nonlinear nature of the problem a possible approach would be the simulation of all possible systems which, obviously, is a time consuming and fastidious task. Therefore, the strategy taken here is to study the DF evolution in the Nyquist diagram of each controller and plant. By this way, we can study the stability and we can predict approximately the occurrence and the characteristics of limit cycles.

It is a well-known fact that many relationships among physical quantities are not linear, although they are often approximated by linear equations, mainly for mathematical simplicity. This simplification may be satisfactory as long as the resulting solutions are in agreement with experimental results. In fact, Cox [38] demonstrated that this is the case with the approximation of nonlinear systems by a DF where limit cycles can be predicted with reasonable accuracy. The DF method is not the only one tractable to limit cycle prediction; nevertheless, in the condition of limit cycle occurrence all of the methods are equivalent to the DF method [38].

Let us consider the feedback system of Fig. 27 with one nonlinear element N and a linear system $G(s)$.

Suppose that the input to a nonlinear element is sinusoidal $x(t) = X\sin(\omega t)$. In general the output of the nonlinear element is not sinusoidal, but it is periodic, with the same period as the input, containing higher harmonics in addition to the fundamental harmonic component.

If we assume that the nonlinearity is symmetric with respect to the variation around zero, the Fourier series become:

$$y(t) = \sum_{k=1}^{\infty} Y_k \cos(k\,\omega\, t + \phi_k) \tag{20}$$

where Y_k and ϕ_k are the amplitude and the phase shift of the kth harmonic component of the output $y(t)$, respectively.

In the DF analysis, we assume that only the fundamental harmonic component of the output is significant. Such assumption is often valid since the higher harmonics in the output of a nonlinear element are usually of smaller amplitude than the fundamental component. Moreover, most control systems are "low-pass filters" with the result that the higher harmonics are further attenuated.

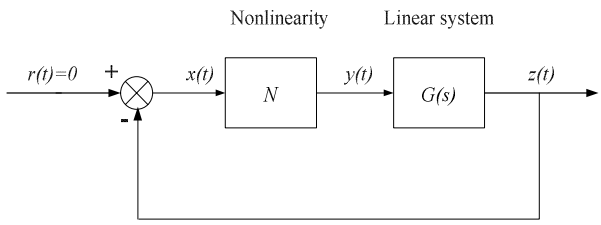

Fig. 27. Nonlinear control system

The DF, or sinusoidal DF, of a nonlinear element, $N(X,\omega)$, is defined as the complex ratio of the fundamental harmonic component of the output $y(t)$ and the input $x(t)$, that is:

$$N(X,\omega)=\frac{Y_1}{X}e^{j\phi_1} \tag{21}$$

where the symbol N represents the DF, X is the amplitude of the input sinusoid and Y_1 and ϕ_1 are the amplitude and the phase shift of the fundamental harmonic component of the output, respectively. Several DFs of standard nonlinear system elements can be found in the references [36, 37, 39].

For nonlinear systems that do not involve energy storage, the DF is merely amplitude-dependent, that is $N = N(X)$. When dealing with nonlinear elements that store energy, the DF method is both amplitude and frequency dependent, that is, $N = N(X, \omega)$. In this case, to determine the DF usually we have a numerical approach rather than a symbolic one because, in general, it is impossible to find a closed-form solution for the differential equations that model the nonlinear element. Nevertheless, it is possible to calculate the approximate analytical expressions for such DFs, namely with the aid of computer algebra packages. Once calculated, the DF can be used for the approximate stability analysis of a nonlinear control system.

Let us consider the standard control system shown in Fig. 27 where the block N denotes the DF of the nonlinear element. If the higher harmonics are sufficiently attenuated, N can be treated as a real or complex variable gain and the closed-loop frequency response becomes:

$$\frac{C(j\omega)}{R(j\omega)}=\frac{NG(j\omega)}{1+NG(j\omega)} \tag{22}$$

The characteristic equation is:

$$1+NG(j\omega)=0 \Leftrightarrow G(j\omega)=-\frac{1}{N(X,\omega)} \tag{23}$$

If (23) can be satisfied for some value of X and ω, a limit cycle is *predicted* for the nonlinear system. Moreover, since (23) applies only if the nonlinear system is in a steady-state limit cycle, the DF analysis predicts only the presence or the absence of a limit cycle and cannot be applied to the analysis of other types of time responses.

5.3. Systems with nonlinear friction

In this subsection we calculate the DF of a dynamical system with nonlinear friction with a combination of the viscous and Coulomb components and we study its properties. Let us consider a system (Fig. 28a) with a mass M, moving on a horizontal plane under the action of a force f, with a friction effect composed of two components: a non-linear Coulomb K part and a linear viscous B part (CV model), (Fig. 28b).

The equation of motion in this system is as follows:

$$M\,\ddot{x}(t)+F_f(t)=f(t) \tag{24}$$

where M is the system mass, $F_f(t)$ is the friction force and $f(t)$ the applied input force.

For the simple system of Figure 28a) we can calculate, numerically, the polar plot of $-1/N(F,\omega)$ considering as input a sinusoidal force $f(t)=F\cos(\omega t)$ applied to mass M and as output the position $x(t)$.

Figure 29 shows the function $-1/N(F,\omega)$ for several values of F when $M = 9$ Kg, $B = 0.5$ Ns/m, $K = 5$ N.

Figure 30 illustrates the log-log plots of Re{–1/N} and Im{–1/N} *vs*. the exciting frequency ω, for different values of the input force F = {10, 50, 100} N. The charts reveal that we have different results according to the excitation force F, being it more visible for the imaginary component.

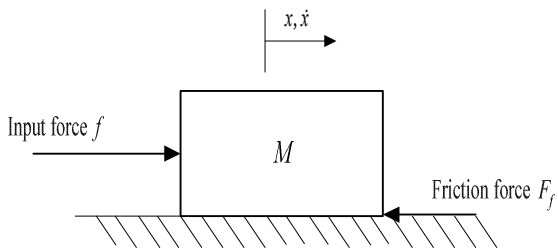

Fig. 28. a) Elemental mass system subjected to nonlinear friction

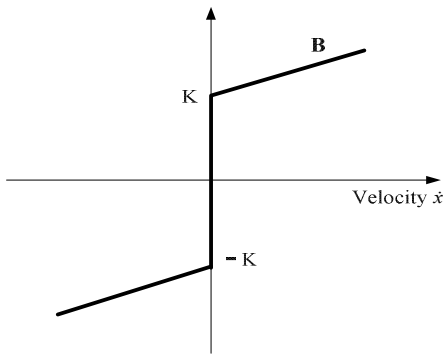

Fig. 28. b) Non-linear friction with Coulomb, Viscous (CV model) and Static components (CVS model)

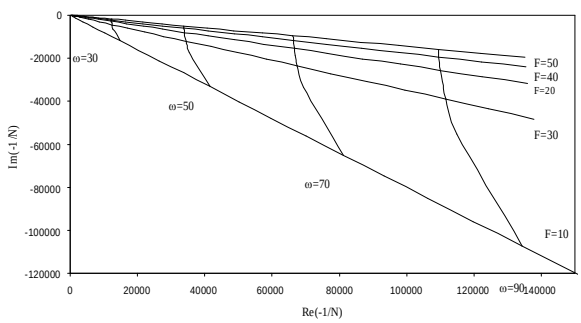

Fig. 29. Polar plot of $-1/N(F,\omega)$ for the system subjected to nonlinear friction (CV model) and input forces F = {10, 20, 30, 40, 50} N

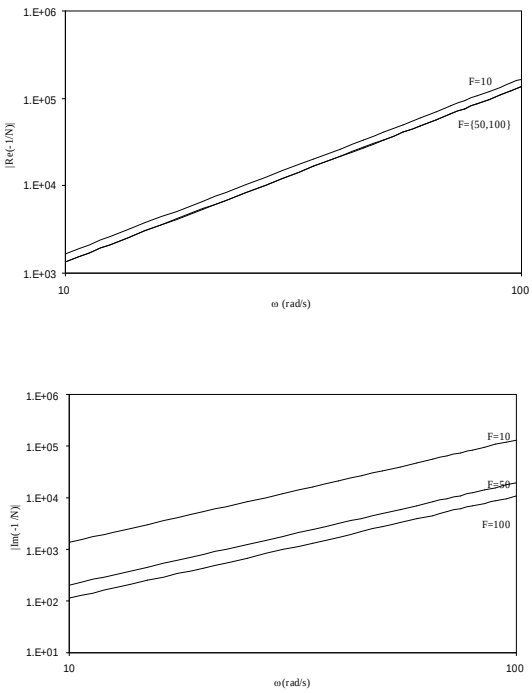

Fig 30. Log-log plots of Re{−1/N} and Im{−1/N} *vs*. the exciting frequency ω for *F* = {10, 50, 100} N, with de CV model.

In Fig. 31 it is depicted the harmonic content of the output signal $x(t)$ for input forces of $F = 10$ N and $F = 50$ N. From this charts we conclude that the output signal has a half - wave symmetry, because the harmonics of even order are negligible. Moreover, the fundamental component of the output signal is the most important one, while the amplitude of the high order harmonics decays significantly. Therefore, we can conclude that, for the friction CV model, the DF method leads to a good approximation.

In order to gain further insight into the system nature, we repeat the experiment for different mass values M = {0.10, 0.25, 0.50, 1.0, 2.0, 3.0, 5.0, 7.0} Kg. The results shows that the value of Re{−1/N} and Im{−1/N} fluctuate for different M values.

To study the relation between Re{−1/N} and Im{−1/N} *versus* F and M, we approximate the numerical results through power functions:

$$\mathrm{Re}\{-1/N\} = a\,\omega^{b}\,,\ \mathrm{Im}\{-1/N\} = c\,\omega^{d} \tag{25}$$

Figure 32 illustrates the variation of the $\{a, b, c, d\}$ parameters with F and M. The $\{a, b, c, d\}$ parameters can also be approximated by heuristic analytical expressions, namely:

$$\begin{aligned} a &= \alpha F/(F-\beta) \\ b &\approx 2.0 \\ c &= \chi F/(F-\delta)^{\varepsilon} \\ d &= -\rho \ln(F) + \eta \end{aligned} \tag{26}$$

where F is the input force and $\{\alpha, \beta, \chi, \delta, \varepsilon, \rho, \eta\}$ are parameters that depend on the mass M. We conclude that the parameters β and δ seems similar to K. Moreover, Re{−1/N} and Im{−1/N} have distinct relationships with ω, namely integer and fractional order dependences. The second case is of utmost importance because it establishes a link towards the area of fractional calculus [18, 42, 43] and it properties of dynamical memory.

The results encourage further studies of nonlinear systems in a similar perspective and the analysis of limit cycle prediction.

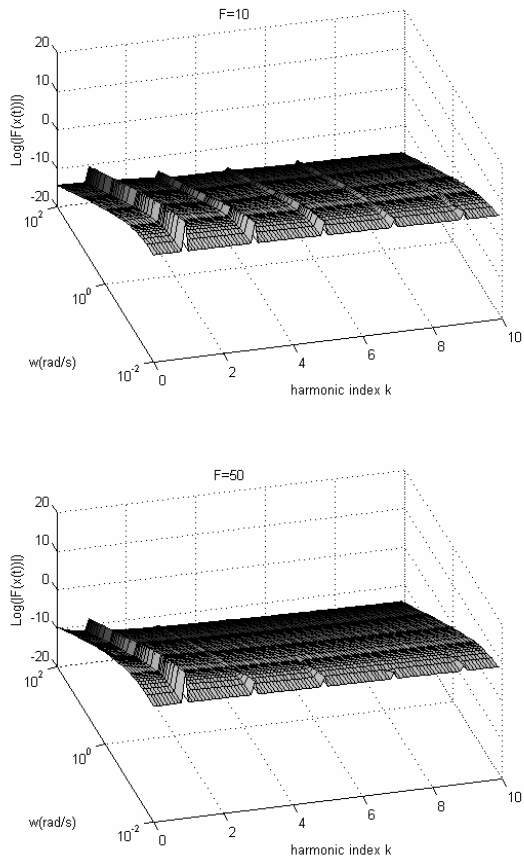

Fig. 31. Fourier transform of the output position *x*(*t*), over 50 cycles for the CV model, *vs*. the exciting frequency ω and the harmonic frequency index *k* for input forces *F* = 10 N and *F* = 50 N

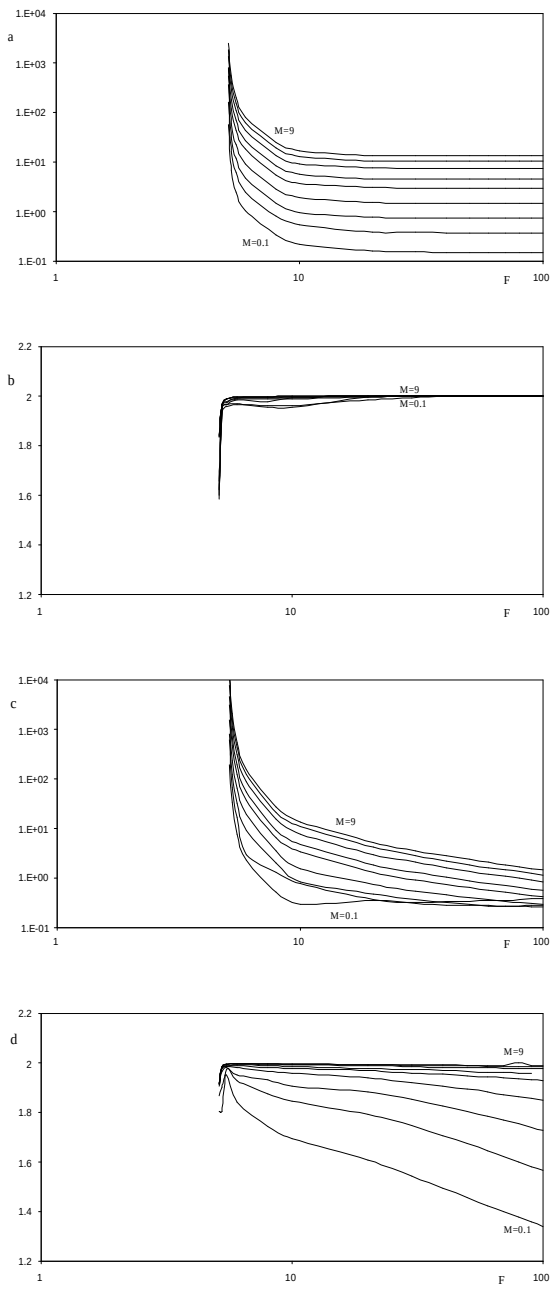

Fig. 32. Variation of the {*a*, *b*, *c*, *d*} parameters versus *F* and *M* = {0.1, 0.25, 0.5, 1, 2, 3, 5, 7, 9} Kg, in the CV model

7. FRACTIONAL ORDER FOURIER SPECTRA IN ROBOTIC MANIPULATORS WITH VIBRATIONS

This section presents a fractional calculus (FC) perspective in the study of the robotic signals captured during an impact phase of the manipulator. In the experiment is used a steel rod flexible link. To test impacts, the link consists on a long, thin, round, flexible steel rod clamped to the end-effector of the manipulator. The robot motion is programmed in a way such that the rod moves against a rigid surface. During the motion of the manipulator the clamped rod is moved by the robot against a rigid surface. An impact occurs and several signals are recorded with a sampling frequency of $f_s = 500$ Hz. In order to analyze the vibration and impact phenomena an acquisition system was developed [44]. The instrumentation system acquires signals from multiple sensors that capture the axis positions, mass accelerations, forces and moments and electrical currents in the motors. Afterwards, an analysis package, running off-line, reads the data recorded by the acquisition system and examines them.

Due to space limitations only some of the signals are depicted. A typical time evolution of the electrical currents of robot axis motors is shown in Fig. 33 corresponding to: (*i*) the impact of the rod on a rigid surface and (*ii*) without impact [45]. In this example, the signals present clearly a strong variation at the instant of the impact that occurs, approximately, at $t = 4$ sec.

In order to study the behavior of the signal Fourier transform, a trendline can be superimposed over the spectrum based on a power law approximation:

$$\left|\mathrm{F}\{f(t)\}\right| \approx c\omega^{m} \tag{27}$$

where F{} is Fourier operator, c is a constant, ω is the frequency and m is the slope.

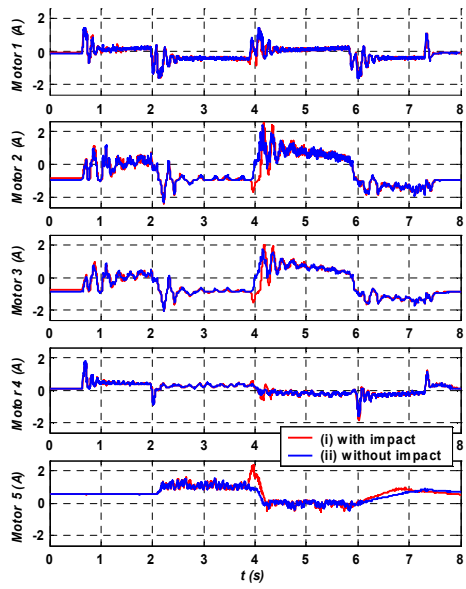

Fig. 33. Electrical currents of robot axis motors

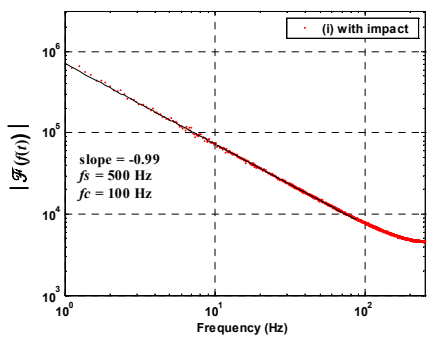

Fig. 34. Spectrum of the axis 1 position

Figure 34 shows the amplitude of the Fast Fourier Transform (FFT) of the axis 1 position signal. The trendline (27) leads to a slope $m = -0.99$ revealing, clearly, the integer order behavior. The others position signals were studied, revealing also an integer behavior, both under impact and no impact conditions.

Figure 35 shows the amplitude of the FFT of the electrical current for the axis 3 motor. The spectrum was also approximated by trendlines in a frequency range larger than one decade. These trendlines (Fig. 34) have slopes of $m = -1.52$ and $m = -1.51$ under impact (*i*) and without impact (*ii*) conditions, respectively. The lines present a fractional order behavior in both cases. The others axis motor currents were studied, as well. Some of them, for a limited frequency range, present also fractional order behavior while others have a complicated spectrum difficult to approximate by one trendline.

Figure 36 shows, as example, the spectrum of the F_z force. This spectrum is not so well defined in a large frequency range. All force/moments spectra present identical behavior and, therefore, it is difficult to define accurately the behavior of the signals.

Finally, Fig. 37 depicts the spectrum of the signal captured from the accelerometer 1 located at the rod free-end of the beam. Like the spectrum from the other accelerometer located at the rod clamped-end, this spectrum is spread and complicated. Therefore, it is difficult to define accurately the slope of the signal and consequently its behavior in terms of integer or fractional system.

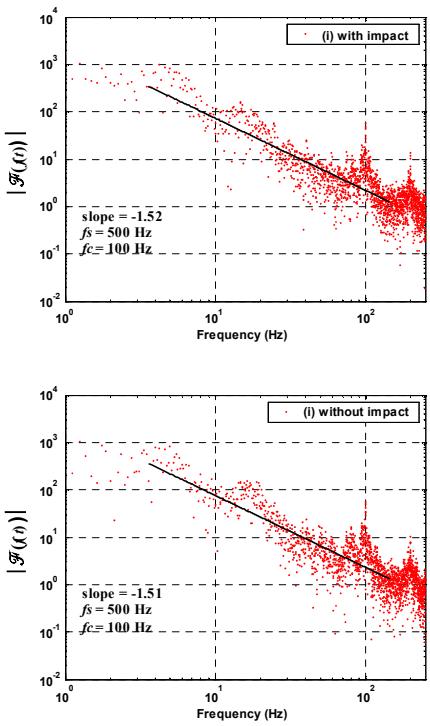

Fig. 35. Spectrum of the axis 3 motor current

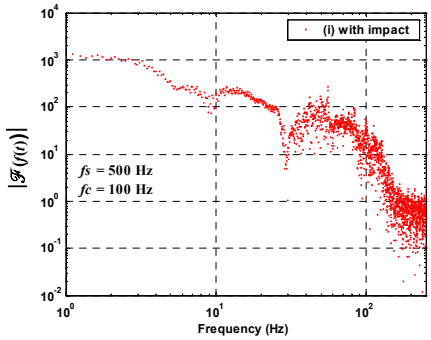

Fig. 36. F_z force spectrum with impact

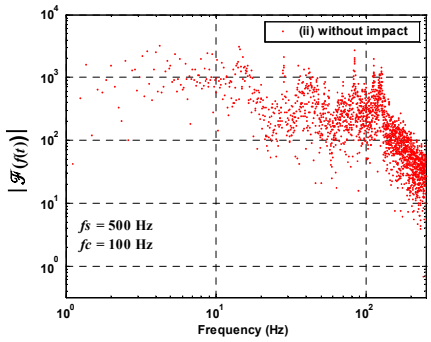

Fig. 37. Acceleration spectrum of the rod free-end without impact

As shown in the examples, the Fourier spectrum of several signals, captured during an impact phase of the manipulator, presents a non integer behavior. On the other hand, the feedback fractional order systems, due to the success in the synthesis of real noninteger differentiator and the emergence of fractional-order controllers [9], have been designed and applied to control a variety of dynamical processes [46]. Therefore the study presented here can assist in the design of the control system to be used in eliminating or reducing the effect of vibrations.

8. POSITION/FORCE CONTROL OF A ROBOTIC MANIPULATOR

Raibert and Craig [47] introduced the concept of force control based on the hybrid algorithm and, since then, several researchers developed those ideas and proposed other schemes [48].

There are two basic methods for force control, namely the hybrid position/ force and the impedance schemes. The first method separates the task into two orthogonal sub-spaces corresponding to the force and the position controlled variables. Once established the subspace decomposition two independent controllers are designed. The second method [48] requires the definition of the arm mechanical impedance. The impedance accommodates the interaction forces that can be controlled to obtain an adequate response.

The dynamical equation of a n dof robot is:

$$\boldsymbol{\tau} = \mathbf{H}(\mathbf{q})\ddot{\mathbf{q}} + \mathbf{C}(\mathbf{q},\dot{\mathbf{q}}) + \mathbf{G}(\mathbf{q}) - \mathbf{J}^{\mathbf{T}}(\mathbf{q})\mathbf{F} \tag{28}$$

where τ is the $n \times 1$ vector of actuator torques, $\mathbf{q}$ is the $n \times 1$ vector of joint coordinates, $\mathbf{H}(\mathbf{q})$ is the $n \times n$ inertia matrix, $\mathbf{C}(\mathbf{q},\dot{\mathbf{q}})$ is the $n \times 1$ vector of centrifugal/Coriolis terms and $\mathbf{G}(\mathbf{q})$ is the $n \times 1$ vector of gravitational effects. The $n \times m$ matrix $\mathbf{J}^{\mathrm{T}}(\mathbf{q})$ is the transpose of the Jacobian matrix of the robot and $\mathbf{F}$ is the $m \times 1$ vector of the force that the (m-dimensional) environment exerts in the robot gripper.

$$\mathbf{H}(\mathbf{q}) = \begin{bmatrix} (m_1+m_2)r_1^2 + m_2 r_2^2 + 2m_2 r_1 r_2 C_2 + J_{1m} + J_{1g} & m_2 r_2^2 + m_2 r_1 r_2 C_2 \\ m_2 r_2^2 + m_2 r_1 r_2 C_2 & m_2 r_2^2 + J_{2m} + J_{2g} \end{bmatrix} \tag{29a}$$

$$\mathbf{C}(\mathbf{q},\dot{\mathbf{q}}) = \begin{bmatrix} -m_2 r_1 r_2 S_2 \dot{q}_2^{\,2} - 2m_2 r_1 r_2 S_2 \dot{q}_1 \dot{q}_2 \\ m_2 r_1 r_2 S_2 \dot{q}_1^{\,2} \end{bmatrix} \tag{29b}$$

$$\mathbf{G}(\mathbf{q}) = \begin{bmatrix} g(m_1 r_1 C_1 + m_2 r_1 C_1 + m_2 r_2 C_{12}) \\ g m_2 r_2 C_{12} \end{bmatrix} \tag{29c}$$

$$\mathbf{J}^{\mathbf{T}}(\mathbf{q}) = \begin{bmatrix} -r_1 S_1 - r_2 S_{12} & r_1 C_{11} + r_2 C_{12} \\ -r_2 S_{12} & r_2 C_{12} \end{bmatrix} \tag{29d}$$

where $C_{ij} = \cos(q_i + q_j)$ and $S_{ij} = \sin(q_i + q_j)$.

The numerical values adopted for the 2R robot [49] are $m_1 = 0.5$ kg, $m_2 = 6.25$ kg, $r_1 = 1.0$ m, $r_2 = 0.8$ m, $J_{1\mathrm{m}} = J_{2\mathrm{m}} = 1.0$ kgm^2 and $J_{1\mathrm{g}} = J_{2\mathrm{g}} = 4.0$ kgm^2.

The constraint plane is determined by the angle θ (Fig. 38) and the contact displacement x_{c} of the robot gripper with the constraint surface is modeled through a linear system with a mass M, a damping B and a stiffness K with dynamics:

$$F_c = M\ddot{x}_c + B\dot{x}_c + Kx_c \tag{30}$$

In order to study the dynamics and control of one robot we adopt the position/force hybrid control with the implementation of the integer order and fractional-order algorithms [5, 6, 32, 51]. The system performance and robustness is analyzed in the time domain. The effect of dynamic backlash and flexibility is also investigated.

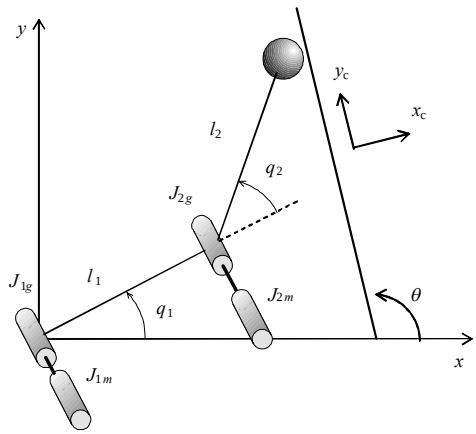

Fig. 38. The 2*R* robot and the constraint surface

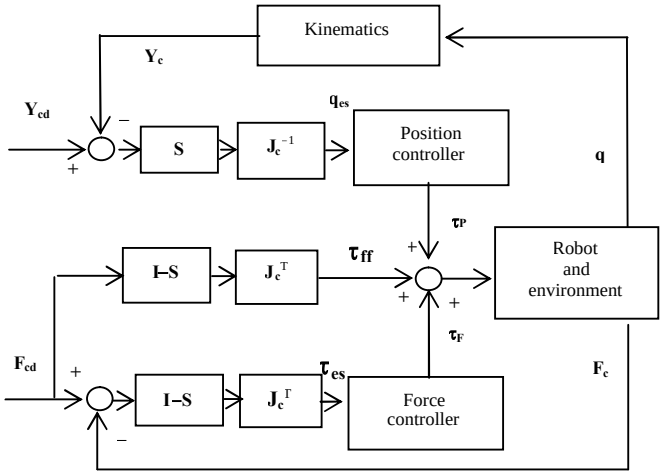

Fig. 39. The position/force hybrid controller

8.1. The Hybrid Controller

The structure of the position/force hybrid control algorithm is depicted in Fig. 39. The diagonal $n \times n$ selection matrix $\mathbf{S}$ has elements equal to one (zero) in the position (force) controlled directions and $\mathbf{I}$ is the $n \times n$ identity matrix. In this paper the y_{c} (x_{c}) cartesian coordinate is position (force) controlled, yielding:

$$\mathbf{S} = \begin{bmatrix} 0 & 0 \\ 0 & 1 \end{bmatrix}, \ \mathbf{J_c}(\mathbf{q}) = \begin{bmatrix} -r_1 C_{\theta 11} - r_2 C_{\theta 12} & -r_2 C_{\theta 12} \\ r_1 S_{\theta 11} + r_2 S_{\theta 12} & r_2 S_{\theta 12} \end{bmatrix} \tag{31}$$

where $C_{\theta ij} = \cos(\theta - q_i - q_j)$ and $S_{\theta ij} = \sin(\theta - q_i - q_j)$.

8.2. Controller Performances

This section analyzes the system performance both for ideal transmissions and robots with dynamic phenomena at the joints, such as backlash and flexibility. Moreover, we compare the response of *FO* and the *PD*: $C_{\mathrm{P}}(s) = K_p + K_d\, s$ and *PI*: $C_{\mathrm{F}}(s) = K_p + K_i\, s^{-1}$ controllers, in the position and force loops.

Both algorithms were tuned by trial and error having in mind getting a similar performance in the two cases. The resulting parameters were *FO*: $\{K_{\mathrm{P}},\alpha_{\mathrm{P}}\} \equiv \{10^5, 1/2\}$, $\{K_{\mathrm{F}},\alpha_{\mathrm{F}}\} \equiv \{10^3, -1/5\}$ and *PD*/*PI*: $\{K_p,K_d\} \equiv \{10^4, 10^3\}$, $\{K_p,K_i\} \equiv \{10^3, 10^2\}$ for the position and force loops, respectively. Moreover, it is adopted the operating point $\{x,y\} \equiv \{1,1\}$, a constraint surface with parameters $\{\theta,M,B,K\} \equiv \{\pi/2, 10^3, 1.0, 10^2\}$ and a controller sampling frequency $f_{\mathrm{c}} = 1$ kHz.

In order to study the system dynamics we apply, separately, rectangular pulses, at the position and force references, that is, we perturb the references with $\{\delta y_{\mathrm{cd}}, \delta F_{\mathrm{cd}}\} = \{10^{-1}, 0\}$ and $\{\delta y_{\mathrm{cd}}, \delta F_{\mathrm{cd}}\} = \{0, 10^{-1}\}$.

Figures 40 and 41 depict the time response of the 2*R* robot under the action of the *FO* and the *PD*/*PI* controllers for ideal transmissions at the joints.

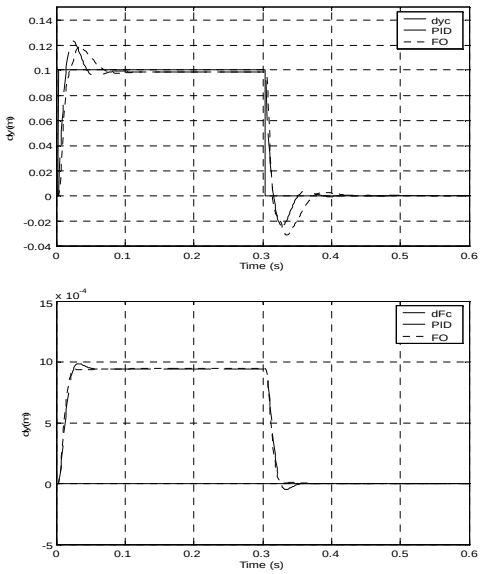

Fig. 40. Time response for the 2*R* robot with ideal transmission at the joints under the action of the *FO* and *PD*/*PI* controllers for a pulse perturbation at the robot position reference

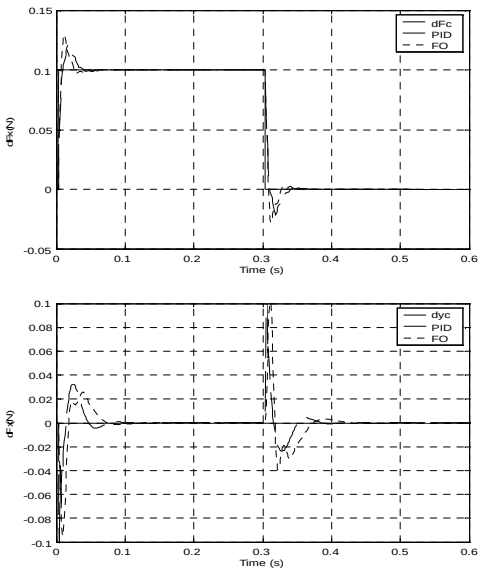

Fig. 41. Time response for the 2*R* robot with ideal transmission at the joints under the action of the *FO* and *PD*/*PI* controllers for a pulse perturbation at the robot force reference

In a second phase (Fig. 42 and 43) we analyze the response of a 2*R* robot with dynamic backlash at the joints. For the *i*th joint gear, with clearance h_i, the backlash reveals impact phenomena between the inertias, which obey the principle of conservation of momentum and the Newton law:

$$\dot{q}_i' = \frac{\dot{q}_i\left(J_{ii} - \varepsilon J_{im}\right) + \dot{q}_{im} J_{im}\left(1+\varepsilon\right)}{J_{ii} + J_{im}} \tag{32a}$$

$$\dot{q}_{im}' = \frac{\dot{q}_i J_i\left(1+\varepsilon\right) + \dot{q}_{im}\left(J_{im} - \varepsilon J_{ii}\right)}{J_{ii} + J_{im}} \tag{32b}$$

where $0 \le \varepsilon \le 1$ defines the type of impact ($\varepsilon = 0$ inelastic impact, $\varepsilon = 1$ elastic), $\dot{q}_i'$ and $\dot{q}_{im}'$ are the inertias velocities of the joint and motor after the collision, and t J_{ii} and J_{im} stand for the link and motor *i*th joint inertias. In the simulations is adopted $h_i = 1.8\ 10^{-4}$ rad and $\varepsilon_i = 0.8$ (i = 1,2).

In a third phase (Fig. 44 and 45) it is studied the case of compliant joints, where the dynamic model corresponds to (28) augmented by the equations:

$$\boldsymbol{\tau} = \mathbf{J}_{\mathbf{m}}\ddot{\mathbf{q}}_{\mathbf{m}} + \mathbf{B}_{\mathbf{m}}\dot{\mathbf{q}}_{\mathbf{m}} + \mathbf{K}_{\mathbf{m}}\left(\mathbf{q}_{\mathbf{m}} - \mathbf{q}\right) \tag{33a}$$

$$\mathbf{K}_{\mathbf{m}}\left(\mathbf{q}_{\mathbf{m}} - \mathbf{q}\right) = \mathbf{J}\left(\mathbf{q}\right)\ddot{\mathbf{q}} + \mathbf{C}\left(\mathbf{q}, \dot{\mathbf{q}}\right) + \mathbf{G}\left(\mathbf{q}\right) \tag{33b}$$

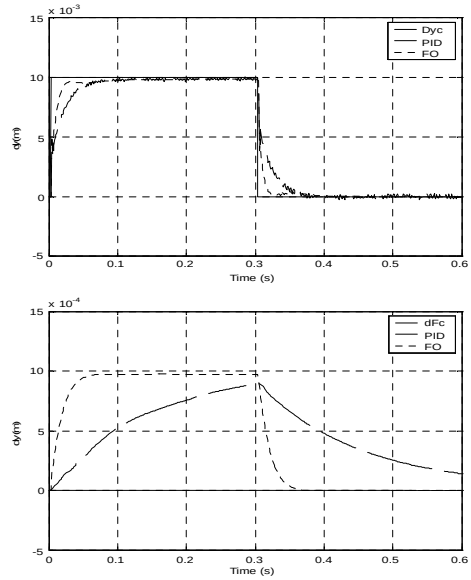

Fig. 42. Time response for 2*R* robot with dynamic backlash at the joints under the action of the *FO* and *PD*/*PI* controllers for a pulse perturbation at the robot position reference.

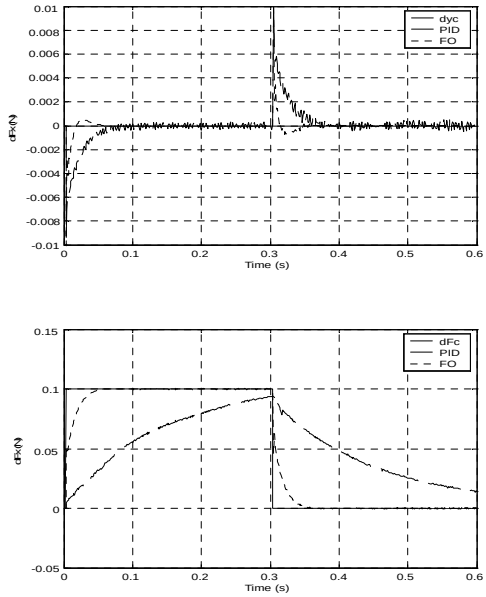

Fig. 43. Time response for 2*R* robot with dynamic backlash at the joints under the action of the *FO* and *PD*/*PI* controllers for a pulse perturbation at the robot force reference.

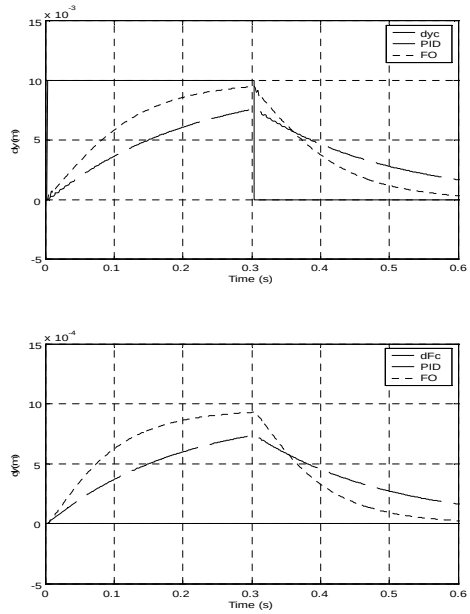

Fig. 44. Time response for 2*R* robot with flexibility at the joints under the action of the *FO* and *PD*/*PI* controllers for a pulse perturbation at the robot position reference.

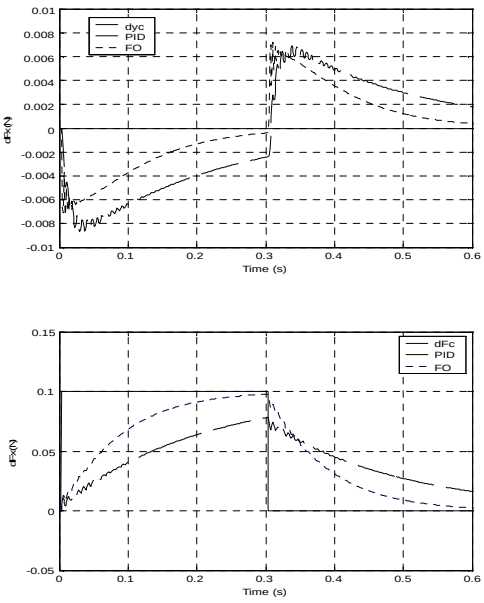

Fig. 45. Time response for 2*R* robot with flexibility at the joints under the action of the *FO* and *PD*/*PI* controllers for a pulse perturbation at the robot force reference.

where $\mathbf{J_m}$, $\mathbf{B_m}$ and $\mathbf{K_m}$ are the $n \times n$ diagonal matrices of the motor and transmission inertias, damping and stiffness, respectively. In the simulations we adopt $K_{mi} = 2\ 10^6$ Nm rad^{-1} and $B_{mi} = 10^4$ Nms rad^{-1} (i = 1,2).

The time responses (Tables 1 and 2), namely the percent overshoot *PO%*, the steady-state error e_{ss}, the peak time T_p and the settling time T_s, reveal that, although tuned for similar performances in the first case, the *FO* is superior to the *PD/PI* in the cases with dynamical phenomena at the robot joints.

Table 1. Time response characteristics for a perturbation δy_{cd}.

joint		*PO%*	e_{ss}	T_p	T_s
ideal	*PID*	23.48%	$99\ 10^{-3}$	0.122	0.013
	FO	18.98%	$79\ 10^{-3}$	0.033	0.018
backlash	*PID*	0.37%	$2.1\ 10^{-3}$	0.383	0.080
	FO	0.36%	$1.4\ 10^{-4}$	0.302	0.118
flexible	*PID*	2.28%	$3.9\ 10^{-3}$	0.403	1.502
	FO	1.80%	$1.4\ 10^{-3}$	0.302	3.004

Table 2. Time response characteristics for a perturbation δF_{cd}.

joint		*PO%*	e_{ss}	T_p	T_s
ideal	*PID*	22.04%	$1.3\ 10^{-3}$	0.083	0.091
	FO	29.54%	$1.3\ 10^{-3}$	0.089	0.093
backlash	*PID*	5.98%	$9.9\ 10^{-2}$	0.402	0.405
	FO	0.86%	$9.9\ 10^{-2}$	0.079	0.043
flexible	*PID*	3.28%	$9.9\ 10^{-2}$	0.602	0.602
	FO	1.82%	$9.9\ 10^{-2}$	0.450	0.450

9. POSITION/FORCE CONTROL OF TWO ARMS WORKING IN COOPERATION

Two robots carrying a common object are a logical alternative for the case in which a single robot is not able to handle the load. The choice of a robotic mechanism depends on the task or the type of work to be performed and, consequently, is determined by the position of the robots and by their dimensions and structure.

In general, the selection is done through experience and intuition; nevertheless, it is important to measure the manipulation capability of the robotic system [52] that can be useful in the robot operation. In this perspective it was proposed the concept of kinematic manipulability [53] and its generalization by including the dynamics [54] or, alters natively, the statistical evaluation of manipulation [55]. Other related aspects such as the coordination of two robots handling objects, collision avoidance and free path planning have been also investigated [56]. With two cooperative robots the resulting interaction forces have to be accommodated and consequently, in addition to position feedback, force control is also required to accomplish adequate performances [57].

We consider two 2*R* cooperating manipulators with identical dimensions (Fig. 46). The contact of the robot gripper with the load is modeled through a linear system with a mass *M*, a damping *B* and a stiffness *K* (Fig. 47).

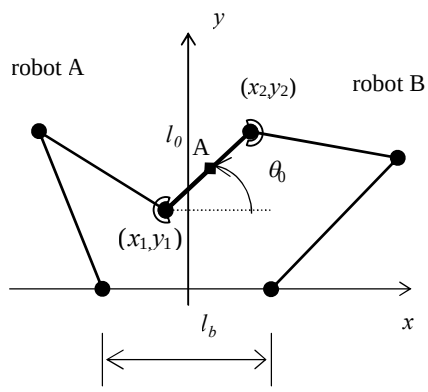

Fig. 46. The 2*R* dual arm robot and the constraint surface

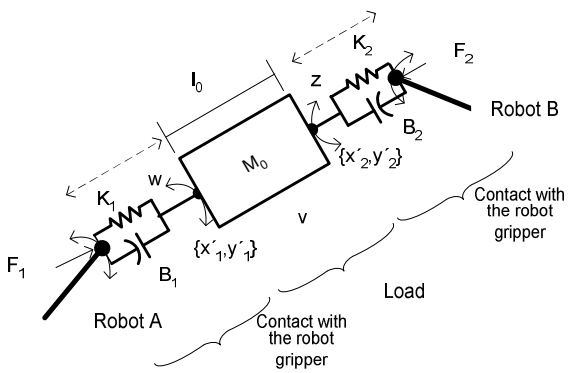

Fig. 47. The contact between the robot gripper and the object

The controller architecture (Fig. 48) is inspired on the impedance and compliance schemes. Therefore, we establish a cascade of force and position algorithms as internal an external feedback loops, respectively, where $\mathbf{x_d}$ and $\mathbf{F_d}$ are the payload desired position coordinates and contact forces.

9.1. Controller Performances

This section analyzes the system performance both for robots ideal transmissions and robots with dynamic phenomena at the joints, such as backlash and flexibility. Moreover, we compare the response of *FO* and classical algorithms namely *PD*: $C_P(s) = K_p\,(1 + T_d\,s)$ and *PI*: $C_F(s) = K_F\,[1 + (T_i\,s)^{-1}]$, in the position and force loops, respectively. Both algorithms were tuned by trial and error having in mind getting a similar performance in the two cases. The resulting parameters were *FO*: $\{K_P,\alpha_P\} \equiv \{10^4, 1/2\}$, $\{K_F,\alpha_F\} \equiv \{2,-1/5\}$ and *PD/PI*: $\{K_p,K_d\} \equiv \{10^4,10^2\}$, $\{K_p,K_i\} \equiv \{10,10^4\}$ for the position and force loops, respectively. Moreover, it is adopted the operating point, the center of the object A $\equiv \{x,y\} \equiv \{0,1\}$ and a object surface with parameters$\{\theta,M,B_j,K_j\} \equiv \{0,10,1.0,10^3\}$.

In order to study the system dynamics we apply, separately, small amplitude rectangular pulses, at the position and force references. Therefore, we perturb the references with $\delta x_d = 10^{-3}$, $\delta y_d = 10^{-3}$, $\delta Fx_d = 1.0$, $\delta Fy_d = 1$. and we analyze the system performance in the time domain.

To evaluate the performance of the proposed algorithms we compare the response for robots with dynamical phenomena at the joints. In all experiments the controller sampling frequency is $f_c = 10$ kHz for the operating point A of the object and a contact force of each gripper of $\{Fx_j,Fy_j\} \equiv \{0.5,5\}$ *Nm* for the *j*th (j = 1, 2) robot.

Figure 49 depicts the time response of the robot A, under the action of the *FO* and the *PD/PI* algorithms, for robots with ideal transmissions at the joints.

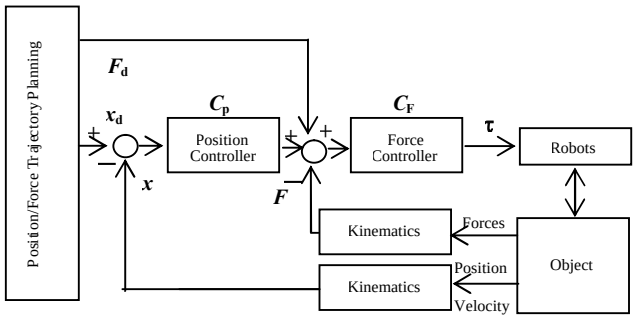

Fig. 48. The position/force cascade controller.

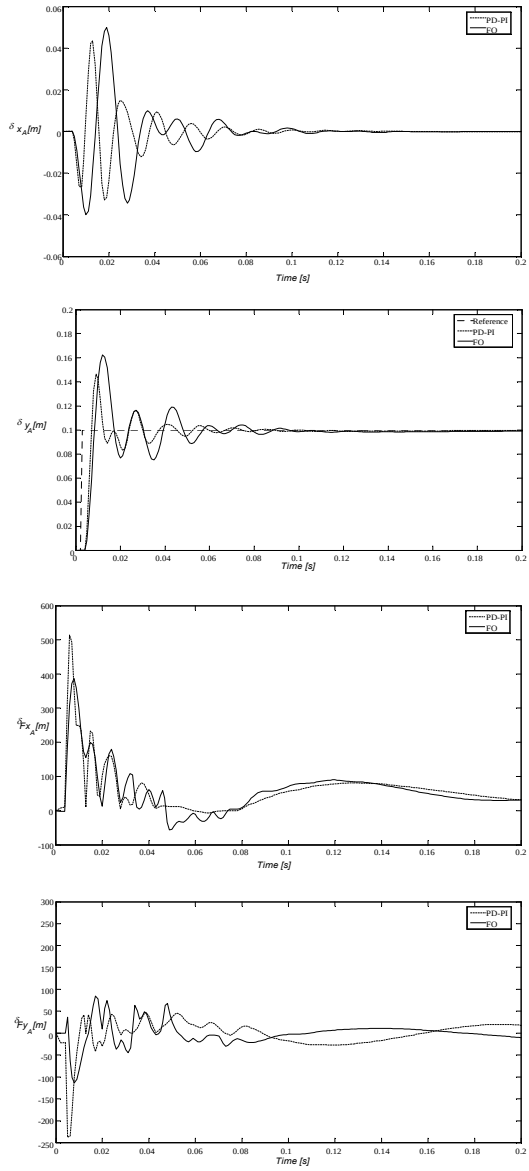

Fig. 49. The time response of robots with ideal joints under the action of the *FO* and the *PD–PI* algorithms for a pulse perturbation at the robot A position reference $\delta y_d = 10^{-3}$ m and a payload $M = 1$ kg, $B_i = 1$ Ns/m and $K_i = 10^3$ N/m.

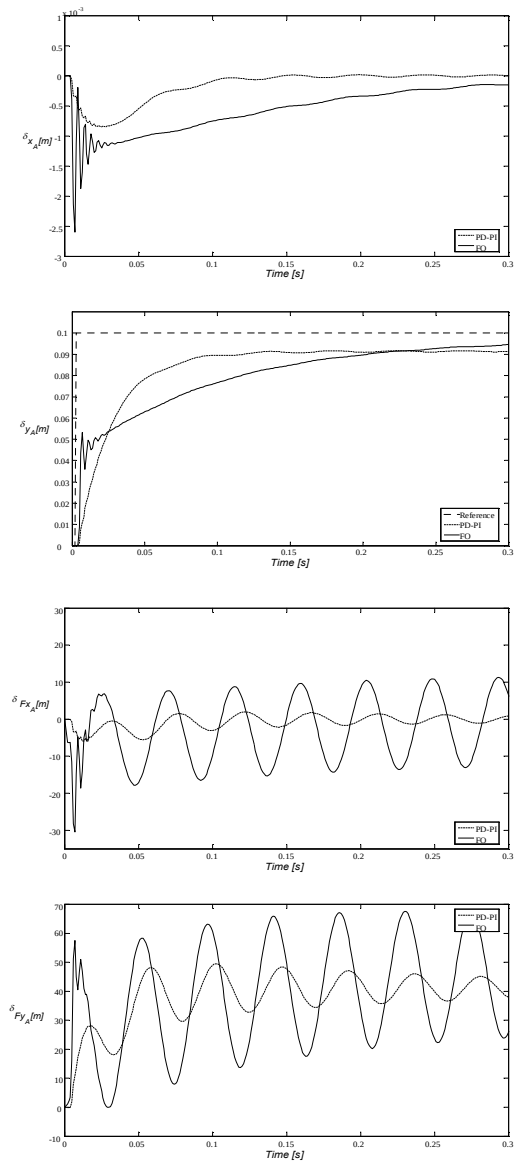

Fig. 50. Time response of robots with joints having backlash under the action of the *FO* and the *PD−PI* algorithms, for a pulse perturbation at the robot A position reference $\delta y_d = 10^{-3}$ m and a payload $M = 1$ kg, $B_i = 1$ Ns/m and $K_i = 10^3$ N/m

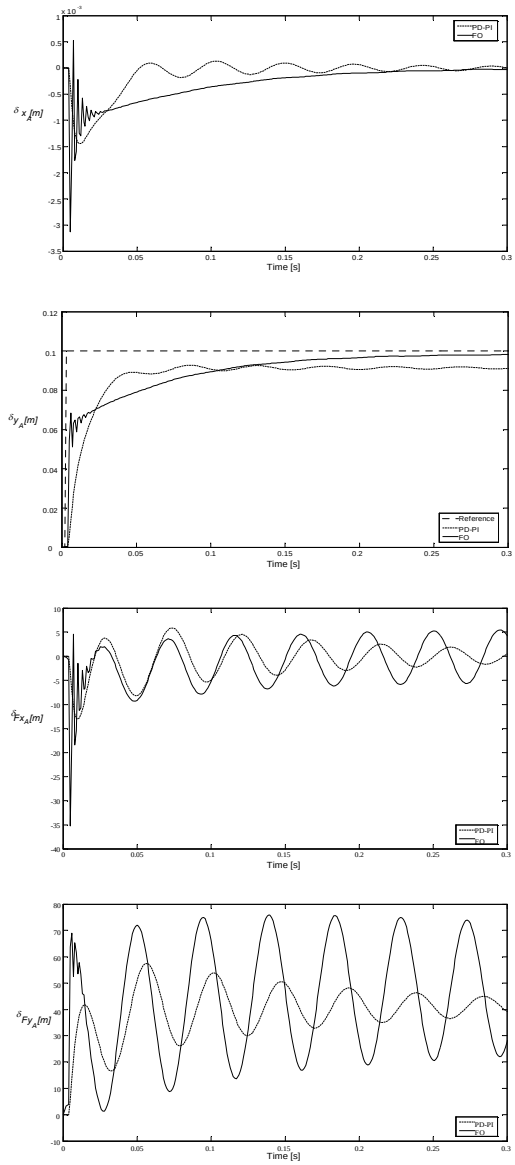

Fig. 51. Time response of robots with joints having backlash under the action of the *FO* and the *PD−PI* algorithms, for a pulse perturbation at the robot A position reference $\delta y_d = 10^{-3}$ m and a payload $M = 1$ kg, $B_i = 1$ Ns/m and $K_i = 10^3$ N/m

In Figs. 50 and 51 we analyze the response of robots with dynamic backlash and dynamic flexibility at the joints.

The time responses (Tables 3-6), namely the percent overshoot *PO%*, the steady-state error e_{ss}, the peak time T_p and the settling time T_s, reveal that, although tuned for similar performances in the first case, the *FO* is superior to the *PD/PI* in the cases with dynamical phenomena at the robot joints.

Table 3. Time response characteristics for a perturbation δx_d the robot A position reference.

Joint		*PO%*	e_{ss}	T_p	T_s
Ideal	*PID*	33.89	$9.8\ 10^{-4}$	$17\ 10^{-3}$	$70\ 10^{-2}$
	FO	25.39	$8.3\ 10^{-4}$	$9\ 10^{-3}$	$50\ 10^{-2}$
Backlash	*PID*	4.5	$5.3\ 10^{-3}$	$17\ 10^{-3}$	$31\ 10^{-3}$
	FO	1.05	$2.2\ 10^{-4}$	$13\ 10^{-3}$	$30\ 10^{-3}$
Flexible	*PID*	4.87	$10\ 10^{-2}$	$35\ 10^{-3}$	$71\ 10^{-3}$
	FO	2.51	$2.2\ 10^{-3}$	$33\ 10^{-3}$	$60\ 10^{-2}$

Table 4. Time response characteristics for a perturbation δy_d the robot A position reference.

Joint		*PO%*	e_{ss}	T_p	T_s
Ideal	*PID*	40.6	$9.7\ 10^{-4}$	$23\ 10^{-2}$	$70\ 10^{-2}$
	FO	25.87	$4.7\ 10^{-4}$	$9\ 10^{-1}$	$45\ 10^{-2}$
Backlash	*PID*	9.5	$9.6\ 10^{-3}$	$66\ 10^{-2}$	$91\ 10^{-2}$
	FO	9.7	$9.7\ 10^{-3}$	$80\ 10^{-3}$	$90\ 10^{-3}$
Flexible	*PID*	9.6	$9.7\ 10^{-3}$	$98\ 10^{-2}$	$98\ 10^{-2}$
	FO	8.8	$2.2\ 10^{-3}$	$93\ 10^{-3}$	$93\ 10^{-2}$

Table 5. Time response characteristics for a perturbation $\delta F x_d$ at the robot A force reference.

Joint		*PO%*	e_{ss}	T_p	T_s
Ideal	*PID*	−78.54	$102\ 10^{-2}$	$11\ 10^{-3}$	$23\ 10^{-3}$
	FO	−90.32	$94\ 10^{-2}$	$99\ 10^{-3}$	$199\ 10^{-3}$
backlash	*PID*	−89.85	$93\ 10^{-2}$	$10\ 10^{-2}$	$20\ 10^{-2}$
	FO	−92.32	$93\ 10^{-2}$	$27\ 10^{-2}$	$55\ 10^{-2}$
Flexible	*PID*	−89.51	$94\ 10^{-2}$	$5.6\ 10^{-2}$	$11\ 10^{-2}$
	FO	−91.76	$93\ 10^{-2}$	$23\ 10^{-2}$	$47\ 10^{-2}$

Table 6. Time response characteristics for a perturbation δFy_d at the robot A force reference.

joint		*PO%*	e_{ss}	T_p	T_s
ideal	*PID*	−78.96	$10\ 10^{-1}$	$14\ 10^{-3}$	$29\ 10^{-3}$
	FO	−90.69	$9.4\ 10^{-2}$	$99\ 10^{-3}$	$199\ 10^{-3}$
backlash	*PID*	−90.63	$93\ 10^{-2}$	$23\ 10^{-2}$	$46\ 10^{-2}$
	FO	−92.01	$93\ 10^{-2}$	$72\ 10^{-2}$	$145\ 10^{-2}$
flexible	*PID*	−90.67	$93\ 10^{-2}$	$14\ 10^{-2}$	$29\ 10^{-2}$

10. HEAT DIFFUSION

The heat diffusion is governed by a linear one-dimensional partial differential equation (PDE) of the form:

$$\frac{\partial u}{\partial t} = k\frac{\partial^2 u}{\partial x^2} \tag{34}$$

where k is the diffusivity, t is the time, u is the temperature and x is the space coordinate. The system (34) involves the solution of a PDE of parabolic type for which the standard theory guarantees the existence of a unique solution [59].

For the case of a planar perfectly isolated surface we usually apply a constant temperature U_0 at $x = 0$ and analyzes the heat diffusion along the horizontal coordinate x. Under these conditions, the heat diffusion phenomenon is described by a non-integer order model:

$$U(x,s) = \frac{U_0}{s}G(s) \quad G(s) = e^{-x\sqrt{\frac{s}{k}}} \tag{35}$$

where x is the space coordinate, U_0 is the boundary condition and $G(s)$ is the system transfer function.

In our study, the simulation of the heat diffusion is performed by adopting the Crank-Nicholson implicit numerical integration based on the discrete approximation to differentiation as [58-60]:

$$\begin{aligned} -ru[j+1,i+1] + (2+r)u[j+1,i] - ru[j+1,i-1] = \\ = ru[j,i+1] + (2-r)u[j,i] + u[j,i-1] \end{aligned} \tag{36}$$

where $r = k\Delta t(\Delta x^2)^{-1}$, $\{\Delta x, \Delta t\}$ and $\{i, j\}$ are the increments and the integration indices for space and time, respectively.

10.1. Control Strategies

The generalized PID controller $G_c(s)$ has a transfer function of the form:

$$G_c(s) = K\left[1 + \frac{1}{T_i s^{\alpha}} + T_d s^{\beta}\right] \tag{37}$$

where α and β are the orders of the fractional integrator and differentiator, respectively. The constants K, T_i and T_d are correspondingly the proportional gain, the integral time constant and the derivative time constant.

Clearly, taking $(\alpha, \beta) = \{(1, 1), (1, 0), (0, 1), (0, 0)\}$ we get the classical {PID, PI, PD, P} controllers, respectively.

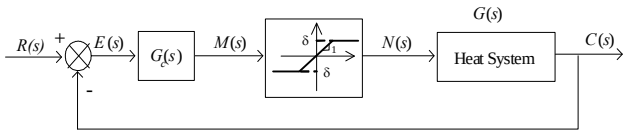

Fig. 52. Closed-loop system with PID controller $G_c(s)$

The $PI^{\alpha}D^{\beta}$ controller is more flexible and gives the possibility of adjusting more carefully the closed-loop system characteristics.

In the next two sub-sections, we analyze the system of Fig. 52 by adopting the classical integer-order PID and a fractional PID^{β}, respectively.

10.2. PID Tuning Using the Ziegler-Nichols Rule

In this sub-section we analyze the closed-loop system with a conventional PID controller given by the transfer function (37) with $\alpha = \beta = 1$. Usually, the PID parameters (K, T_i, T_d) are tuned by using the so-called Ziegler-Nichols open loop (ZNOL) method [60]. The ZNOL heuristics are based on the approximate first-order plus dead-time model:

$$\hat{G}(s) = \frac{K_p}{\tau s + 1}e^{-sT} \tag{38}$$

For the heat system, the resulting parameters are $\{K_p, \tau, T\} = \{0.52, 162, 28\}$ leading to the PID constants $\{K, T_i, T_d\} = \{18.07, 34.0, 8.5\}$.

A step input is applied at $x = 0.0$ m and the closed-loop response $c(t)$ is analyzed for $x = 3.0$ m, without actuator saturation (Fig. 53). We verify that the system with a PID controller, tuned through the ZNOL heuristics, does not produce satisfactory results giving a significant overshoot ov and a large settling time t_s namely $\{t_s, t_p, t_r, ov(\%)\} \equiv \{27.5, 44.8, 12.0, 68.56\}$, where t_p represents the peak time and t_r the rise time. We analyze two indices that measure the response error, namely the integral square error (ISE) and the integral time square error (ITSE) criteria defined as:

$$\text{ISE} = \int_0^{\infty}\left[r(t) - c(t)\right]^2 dt \tag{39}$$

$$\text{ITSE} = \int_0^{\infty} t\left[r(t) - c(t)\right]^2 dt \tag{40}$$

We can use other performance criteria such as the integral absolute error (IAE) or the integral time absolute error (ITAE); however, in the present case the ISE and the ITSE criteria have produced the best results and are adopted in the study.

In this case, the PID reveals the following values for parameters (ISE, ITSE) = (27.53, 613.97).

The poor results indicate again that the method of tuning may not be the most adequate for the control of the heat system.

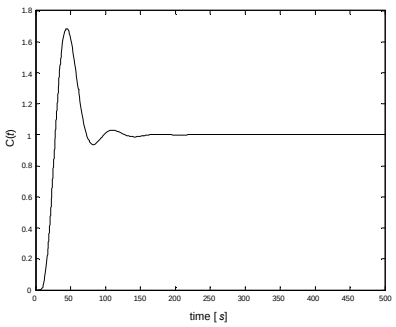

Fig. 53. Step responses of the closed-loop system for the PID controller and $x = 3.0$ m

In fact, the inherent fractional dynamics of the system lead us to consider other configurations. In this perspective, we propose the use of fractional controllers tuned by the minimization of the indices ISE and ITSE.

10.3 PID$^{\beta}$ Tuning Using Optimization Indices

In this sub-section we analyze the closed-loop system under the action of the PID$^{\beta}$ controller given by the transfer function (37) with $\alpha = 1$ and $0 \le \beta \le 1$. The fractional derivative term $T_d s^{\beta}$ in (37) is implemented through a 4th-order Padé discrete rational transfer function. It is used a sampling period of $T = 0.1$ s.

The PID$^{\beta}$ controller is tuned by the minimization of an integral performance index. For that purpose, we adopt the ISE and ITSE criteria.

A step reference input $R(s) = 1/s$ is applied at $x = 0.0$ m and the output $c(t)$ is analyzed for $x = 3.0$ m, without actuator saturation. The heat system is simulated for 3000 seconds. Fig. 54 illustrates the variation of the fractional PID parameters (K, T_i, T_d) as function of the order's derivative β, for the ISE and the ITSE criteria. The dots represent the values corresponding to the classical PID addressed in the previous section.

The curves reveal that for $\beta < 0.4$ the parameters (K, T_i, T_d) are slightly different, for the two ISE and ITSE criteria, while for $\beta \ge 0.4$ they lead to almost similar values. This fact indicates a large influence of a weak order derivative on system's dynamics.

To further illustrate the performance of the fractional-order controllers a saturation nonlinearity is included in the closed-loop system of Fig. 52 and inserted in series with the output of the controller $G_c(s)$. The saturation element is defined as:

$$n(m) = \begin{cases} m, & |m| < \delta \\ \delta \operatorname{sign}(m), & |m| \ge \delta \end{cases} \tag{41}$$

The controller performance is evaluated for $\delta = \{20, \ldots, 100\}$ and $\delta = \infty$ which corresponds to a system without saturation. We use the same fractional-PID parameters obtained without considering the saturation nonlinearity.

Figures 55 and 56 show the step responses of the closed-loop system and the corresponding controller output, for the PID$^{\beta}$ tuned in the ISE and ITSE perspectives for $\delta = 10$ and $\delta = \infty$, respectively. The controller parameters $\{K, T_i, T_d, \beta\}$ correspond to the minimization of those indices leading to the values ISE: $\{K, T_i, T_d, \beta\} \equiv \{3, 23, 90.6, 0.875\}$ and ITSE: $\{K, T_i, T_d, \beta\} \equiv \{1.8, 17.6, 103.6, 0.85\}$.

The step responses reveal a large diminishing of the overshoot and the rise time when compared with the integer PID, showing a good transient response and a zero steady-state error. The PID$^{\beta}$ leads to better results than the classical PID controller tuned through the ZNOL rule. These results demonstrate the effectiveness of the fractional algorithms when used for the control of fractional-order systems. The step response and the controller output are also improved when the saturation level δ is diminished.

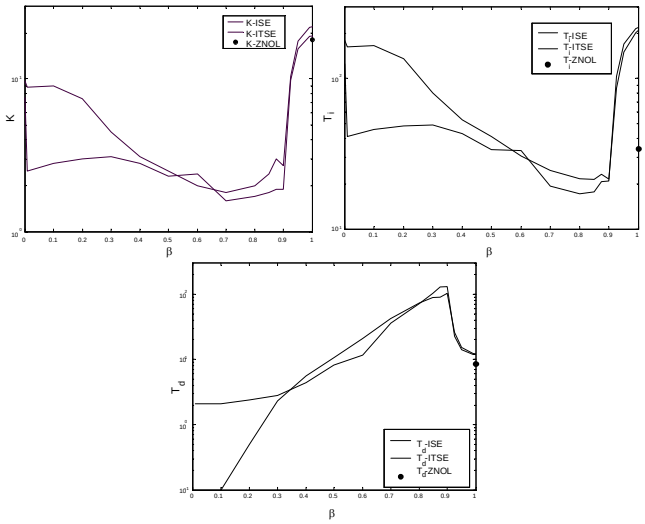

Fig. 54. The PID$^{\beta}$ parameters (K, Ti, Td) versus β for the ISE and ITSE criteria. The dot represents the PID-ZNOL.

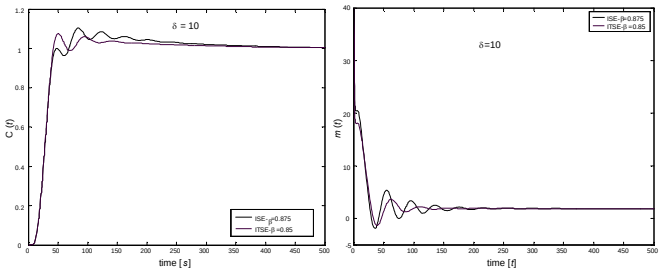

Fig. 55. Step responses of the closed-loop system and the controller output for the ISE and the ITSE indices, with a PID$^{\beta}$ controller, $\delta = 10$ and $x = 3.0$ m.

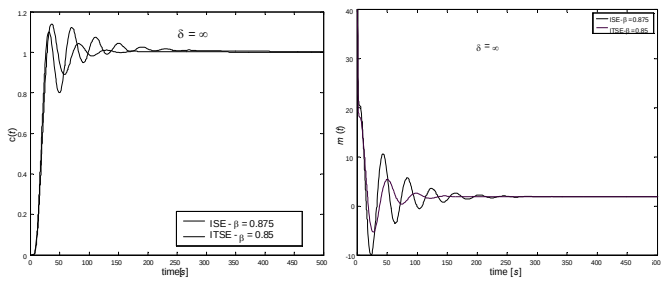

Fig. 56. Step responses of the closed-loop system and the controller output for the ISE and the ITSE indices, with a PID$^{\beta}$ controller, $\delta = \infty$ and $x = 3.0$ m.

Figure 57 depicts the ISE and ITSE indices for $0 \le \beta \le 1$, when $\delta = \{20, ..., 100\}$ and $\delta = \infty$. We verify the existence of a minimum for $\beta = 0.875$ and $\beta = 0.85$ for the ISE and ITSE cases, respectively. Furthermore, the higher the δ the lower the value of the index.

Figures 58 and 59 show the variation of the settling time t_s, the peak time t_p, the rise time t_r, and the percent overshoot ov(%), for the closed-loop response tuned through the minimization of the ISE and the ITSE indices, respectively.

In the ISE case t_s, t_p e t_r diminish rapidly for $0 \le \beta \le 0.875$, while for $\beta > 0.875$ the parameters increase smoothly. For the ITSE we verify the same behavior for $\beta = 0.85$. On the other hand, ov(%) increases smoothly for $0 \le \beta \le 0.7$, while for $\beta > 0.7$ it decreases very quickly, both for the ISE and the ITSE indices.

In conclusion, for $0.85 \le \beta \le 0.875$ we get the best controller tuning, superior to the performance revealed by the classical integer-order scheme.

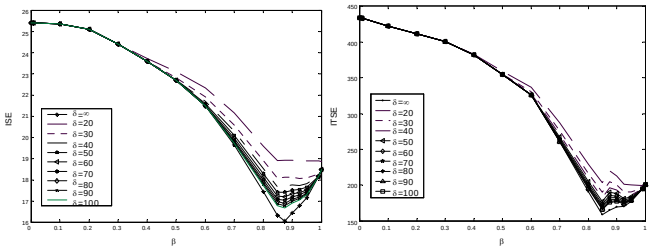

Fig. 57. ISE and ITSE versus $0 \le \beta \le 1$ for $\delta = \{20, ..., 100\}$ and $\delta = \infty$.

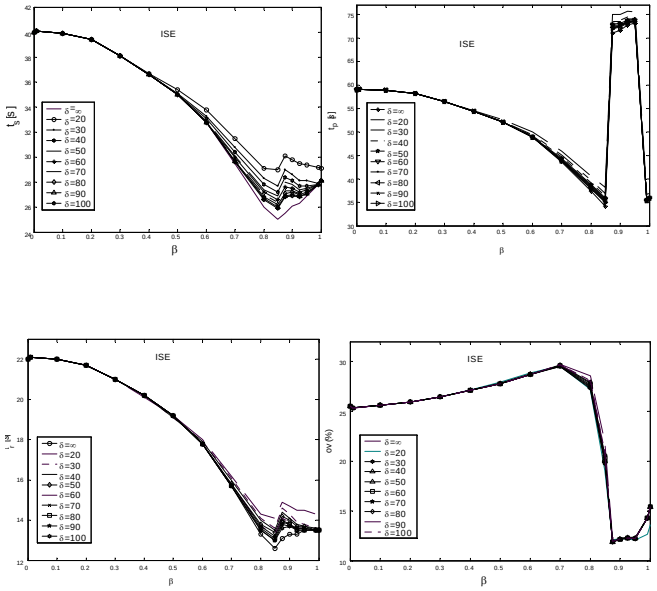

Fig. 58. Parameters t_s, t_p, t_r, ov(%) for the step responses of the closed-loop system for the ISE indice, with a PID$^\beta$ controller, when $\delta = \{20, ..., 100\}$ and $\delta = \infty$, $x = 3.0$ m.

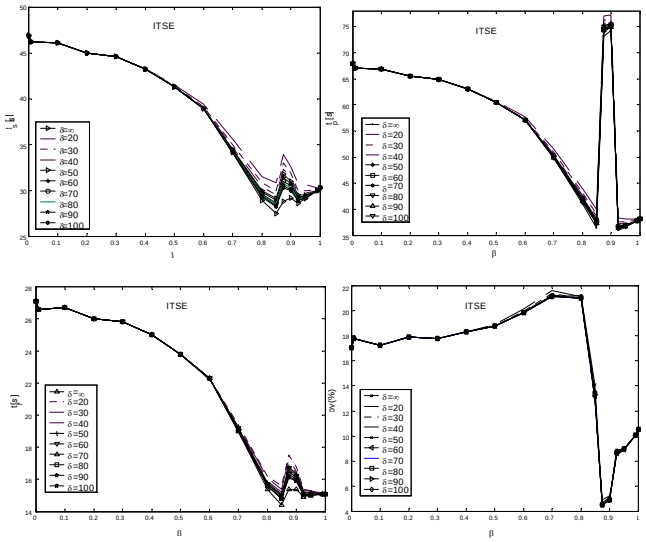

Fig. 59. Parameters t_s, t_p, t_r, ov(%) for the step responses of the closed-loop system for the ITSE indice, with a PID$^\beta$ controller, when $\delta = \{20, ..., 100\}$ and $\delta = \infty$, $x = 3.0$ m.

11. ELECTRICAL IMPEDANCE OF FRUITS

In an electrical circuit the voltage $u(t)$ and the current $i(t)$ can be expressed as a function of time t:

$$u(t) = U_0 \cos(\omega t) \tag{42}$$

$$i(t) = I_0 \cos(\omega t + \phi) \tag{43}$$

where U_0 and I_0 are the amplitudes of the signals, ω is the frequency and ϕ is the current phase shift. The voltage and current can be expressed in complex form as:

$$u(t) = \mathrm{Re}\left\{U_0 e^{j(\omega t)}\right\} \tag{44}$$

$$i(t) = \mathrm{Re}\left\{I_0 e^{j(\omega t + \phi)}\right\} \tag{45}$$

Consequently, the electrical impedance $Z(j\omega)$ is:

$$Z(j\omega) = \frac{U(j\omega)}{I(j\omega)} = Z_0 e^{j\phi} \tag{46}$$

A brief reference about the constant phase elements (CPE) and Warburg impedance is presented here due to their application in the work. In fact, to model an electrochemical phenomenon it is often used a CPE because the surface is not homogeneous [61-62]. So, with a CPE:

$$Z(j\omega) = \frac{1}{(j\omega)^\alpha C} \tag{47}$$

C is the capacitance, with units $[m^{-2/\alpha}\, kg^{-1/\alpha}\, s^{(\alpha+3)/\alpha}\, A^{2/\alpha}]$, and α is a parameter that can change between 0 and 1, being an ideal capacitor for $\alpha = 1$.

On the other hand, in electrochemical systems with diffusion, the impedance is modeled by the so-called Warburg element [62-64]. The Warburg element arises from one-dimensional diffusion of an ionic species to the electrode. If the impedance is under an infinite diffusion layer, the Warburg impedance is:

$$Z(j\omega) = \frac{R}{(j\omega)^{0.5} C} \tag{48}$$

where R is the diffusion resistance. If the diffusion process has finite length, the Warburg element becomes:

$$Z(j\omega) = R\frac{\tanh(j\omega\tau)^{0.5}}{(\tau)^{0.5}} \tag{49}$$

with $\tau = \delta^2 / D$, where R is the diffusion resistance, τ is the diffusion time constant, δ is the diffusion layer thickness and D is the diffusion coefficient.

11.1. Study of Fractional Order Electrical Impedances

The structure of fruits and vegetables have cells that are sensitive to heat, pressure and other stimuli. These systems constitute electrical circuits exhibiting a complex behaviour. Bearing these facts in mind, in our work we study the electrical impedance for several botanical elements, under the point of view of fractional order systems.

We apply sinusoidal excitation signals $v(t)$, to the botanical system, for several distinct frequencies ω (Fig. 60) and the impedance $Z(j\omega)$ is measured based on the resulting voltage $u(t)$ and current $i(t)$. Moreover, we measure the environmental temperature, the weight, the length and width of all botanical elements. This criterion helps us to understand how these factors influence $Z(j\omega)$.

In this study we develop several different experiments for evaluating the variation of the impedance $Z(j\omega)$ with the amplitude of the input signal V_0, for different electrode lengths of penetration inside the element Δ, the environmental temperature T, the weights W and the dimension D.

The value of R is changed for each experiment, in order to adapt the values of the voltage and current to the scale of the measurement device.

We start by analyzing the impedance for an amplitude of input signal of $V_0 = 10$ volt, a constant adaptation resistance $R_a = 15$ kΩ, applied to one *Solanum Tuberosum* (potato), with an weight $W = 1.24\ 10^{-1}$ kg, environmental temperature $T = 26.5$ degree Celsius, dimension $D = 7.97\ 10^{-2} \times 5.99\ 10^{-2}$ m, and the electrode length penetration $\Delta = 2.1\ 10^{-2}$ m.

Figure 61 presents the Bode diagrams for $Z(j\omega)$. The results reveal that the system has a fractional order impedance. In fact, approximating the experimental results in the amplitude Bode diagram through a power function namely by $|Z(j\omega)| = a\omega^{-b}$, we obtain $(a, b) = (4.91\ 10^3, 0.0598)$, at the low frequencies, and $(a, b) = (7.94\ 10^5, 0.5565)$, at the high frequencies.

It is interesting to compare the polar diagram and the admittance loci for *RLC*, series or parallel, circuits. We verify that our systems have similarities with the *RC* parallel circuit and, therefore, we conclude that this vegetable has proprieties similar to a kind of capacitor. In order to analyze the system linearity we evaluate $Z(j\omega)$ for different amplitudes of input systems, namely, $V_0 = \{5, 15, 20\}$ volt, maintaining constant the adaptation resistance $R_a = 15$ kΩ.

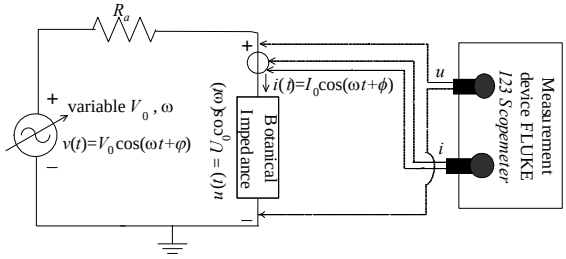

Fig. 60. Electrical circuit for the measurement of the botanical impedance $Z(j\omega)$

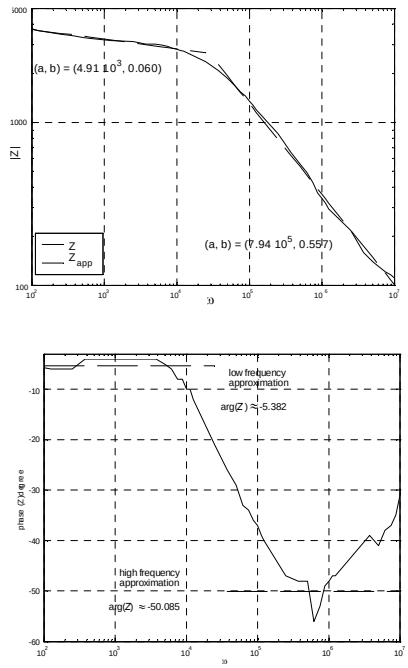

Fig. 61. Bode diagrams of the impedance $Z(j\omega)$ for the potato

The impedance $Z(j\omega)$ has a fractional order and this characteristic does not change significantly with the variation of input signal amplitude (Table 7). Therefore, we can conclude that this system has a linear characteristic.

In a second experiment, we vary the length Δ of the electrode penetration inside the potato, and we evaluate its influence upon the value of the impedance. Therefore, we adjust the electrode to $\Delta = 1.42\ 10^{-2}$ m, with $V_0 = 10$ volt and adaptation resistance $R_a = 5$ kΩ, leading to $|Z(j\omega)|$ approximations $(a, b) = (5.48\ 10^3, 0.0450)$, at the low frequencies, and $(a, b) = (1.00\ 10^6, 0.5651)$, at the high frequencies. With these results, we conclude that the length of wire inside the potato does not change significantly the values of the fractional orders. Also the linearity was again confirmed.

The last experiment with the potato is related with the variation of environmental temperature. In this case, we use the first potato and the same conditions of first experience, but with an temperature $T = 25.7$ degree Celsius. The amplitude impedance $|Z(j\omega)|$ has the values: $(a, b) = (8.91\ 10^3, 0.0555)$, at the low frequencies, and $(a, b) = (7.10\ 10^5, 0.5010)$, at the high frequencies. Once more we verify the small variation of the fractional order.

Table 7. Comparison of the values of $|Z(j\omega)| \approx a\omega^{-b}$ for different amplitudes of the input signal.

Amplitude (volt)	low ω		high ω	
	a	*b*	*a*	*b*
5	$4.79\ 10^{3}$	0.062	$6.52\ 10^{5}$	0.542
10	$4.91\ 10^{3}$	0.060	$7.94\ 10^{5}$	0.557
15	$4.54\ 10^{3}$	0.054	$5.66\ 10^{5}$	0.530
20	$4.65\ 10^{3}$	0.055	$5.86\ 10^{5}$	0.530

Another issue that may influence the results is the weight. Therefore, we apply an input signal with amplitude $V_0 = 10$ volt, adaptation resistance $R_a = 15$ kΩ, with environmental temperature $T = 26.5$ degree Celsius, and electrode penetration $\Delta = 2.1\ 10^{-2}$ m to another potato with dimension $D = 7.16\ 10^{-2} \times 3.99\ 10^{-2}$ m, weight $W = 5.89\ 10^{-2}$ kg. The asymptotic results for $|Z(j\omega)|$ are $(a, b) = (7.17\ 10^{3}, 0.0546)$, at the low frequencies and $(a, b) = (2.00\ 10^{6}, 0.5990)$, at the high frequencies. Again, this experience does not reveal significant variations in the fractional order while the linearity is also confirmed.

In conclusion, the impedance does not change significantly with the factors analyzed. In this line of thought, we organize similar experiments with other vegetables and fruits.

The results correspond to experiments adopting an amplitude of input signal $V_0 = 10$ volt and an electrode penetration $\Delta = 2.1\ 10^{-2}$ m. Similar experiments are developed for several fruits. Table 8 presents the characteristics of the vegetables and fruits respectively.

Table 8. Characteristics of the vegetables and fruits

Vegetable or Fruit / Specie	Weight (kg)	Length (m)	Width (m)
Carrot / *Daucus Carota L.*	$8.85\ 10^{-2}$	$1.55\ 10^{-1}$	$3.39\ 10^{-2}$
Garlic / Allium sativum *L*.	$2.99\ 10^{-3}$	$1.38\ 10^{-2}$	$6.00\ 10^{-3}$
Onion / *Allium cepa L.*	$8.33\ 10^{-2}$	$5.86\ 10^{-2}$	$5.77\ 10^{-2}$
Potato / *Solanum tuberosum*	$1.24\ 10^{-1}$	$7.97\ 10^{-2}$	$5.99\ 10^{-2}$
Pimento / *Capsicum annuum*	$1.30\ 10^{-1}$	$1.23\ 10^{-1}$	$8.20\ 10^{-2}$
Tomato/*Lycopersicom esculentum*	$1.46\ 10^{-1}$	$5.57\ 10^{-2}$	$6.88\ 10^{-2}$
Turnip / *Brassica napobrassica*	$7.90\ 10^{-2}$	$7.26\ 10^{-2}$	$5.43\ 10^{-2}$
Apple / *Malus domestica*	$1.39\ 10^{-1}$	$6.36\ 10^{-2}$	$7.15\ 10^{-2}$
Banana / *Musa ingens*	$1.11\ 10^{-1}$	$1.49\ 10^{-1}$	$3.42\ 10^{-2}$
Kiwi / *Actinidia deliciosa*	$8.95\ 10^{-2}$	$6.52\ 10^{-2}$	$5.50\ 10^{-2}$
Lemon / *Citrus × limon*	$1.66\ 10^{-1}$	$9.19\ 10^{-2}$	$6.58\ 10^{-2}$
Orange / *Citrus sinensis*	$1.53\ 10^{-1}$	$6.69\ 10^{-2}$	$6.98\ 10^{-2}$
Pear / *Pyrus communis*	$9.72\ 10^{-2}$	$6.51\ 10^{-2}$	$5.63\ 10^{-2}$

Figure 62 depicts Re $\{Z(j\omega)\}$ and Im $\{Z(j\omega)\}$ for some of the vegetables and fruits under study, and the corresponding approximation values. In these experiences, the adaptation resistance R_a is changed for each case.

The results reveal that $Z(j\omega)$ has distinct characteristics according with the frequency range. For low frequencies, the impedance is approximately constant, but for high frequencies, it is clearly of fractional order.

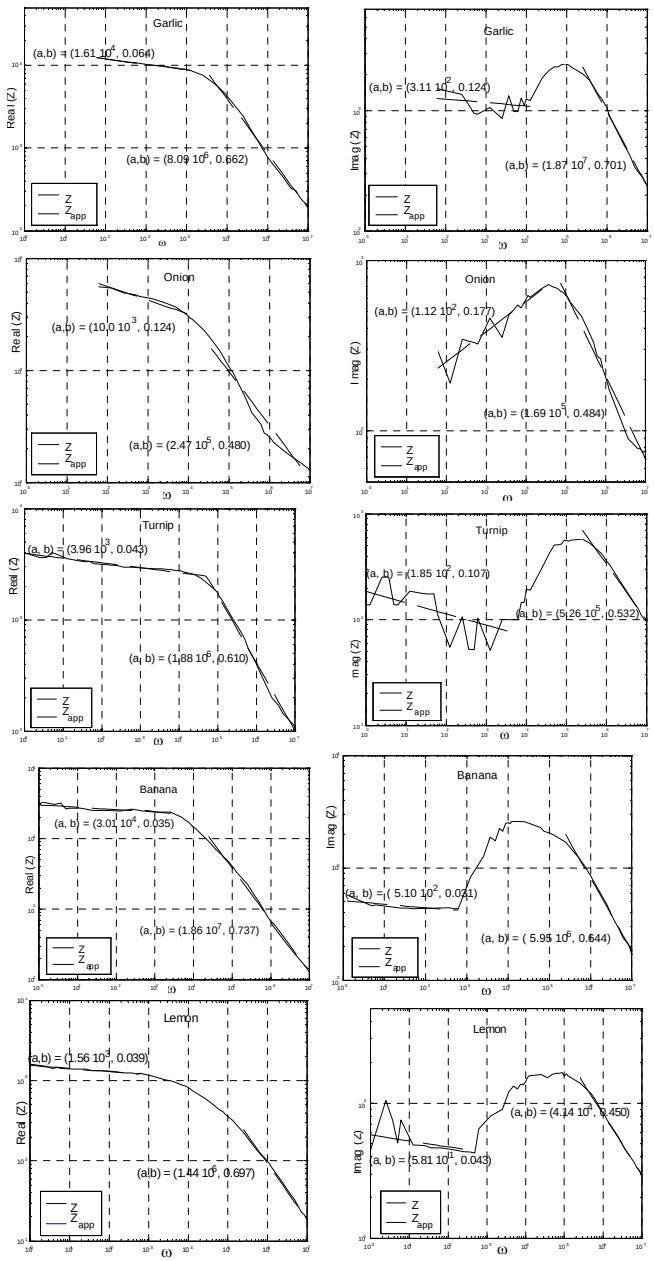

Fig. 62. Diagrams of real Re $[Z(j\omega)]$ and imaginary Im $[Z(j\omega)]$ parts of the electrical impedance for several vegetables and fruits: garlic (with $R_a = 15.0$ kΩ), onion (with $R_a = 2.7$ kΩ), turnip (with $R_a = 2.2$ kΩ), banana (with $R_a = 5.5$ kΩ) and lemon (with $R_a = 750$ Ω)

11.2. The Impedance Model

In the previous section we verified that it is difficult to find a model for $Z(j\omega)$ within the whole frequencies range. In this section, we apply the circuit of Fig. 63, often adopted in the area of electrochemistry, where R_0 and R_1 are resistances and *CPE* is given in (47).

The numerical values of R_0, R_1, C and α for the different impedances are shown in Table 9.

The results reveal a very good fit for several vegetables and fruits. Fig. 64 presents the polar diagrams for the garlic, potato, tomato, kiwi and pear. It is clear that adopting circuits with more components, and other configuration, we can have better approximations. Therefore, in future development we will study new circuits for modeling the impedance of other materials.

Recent research focus on the implementation of fractional order capacitances, often called fractances. Patents and commercial products are presently available, opening promising areas of application in electronics and control [62].

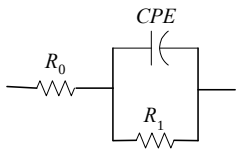

Fig. 63. The Randles circuit

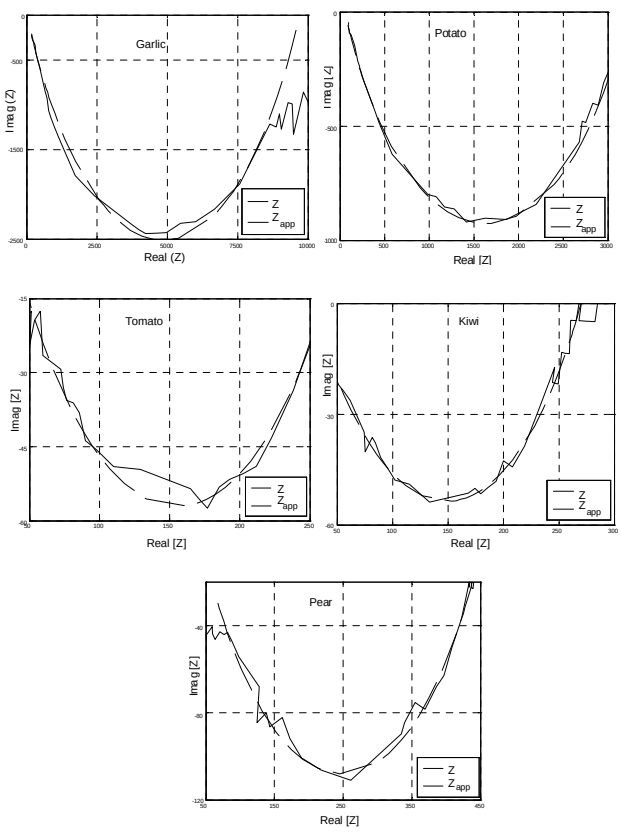

Fig 64. Polar diagrams of the impedance $Z(j\omega)$ for several vegetables and fruits: garlic, potato tomato, kiwi and pear

Table 9. Values of the elements of the Randles circuit for the garlic, potato, tomato, kiwi and pear.

Vegetable / fruits	R_0 [Ω]	R_1 [Ω]	C	α
Garlic	1	$9.7\ 10^3$	$1.81\ 10^{-7}$	0.609
Potato	57	$3.15\ 10^3$	$2.40\ 10^{-7}$	0.677
Tomato	35.04	240.30	$5.00\ 10^{-6}$	0.565
Kiwi	28.04	242.00	$7.67\ 10^{-6}$	0.531
Pear	44.04	409.00	$1.14\ 10^{-6}$	0.619

This article follows an alternative strategy, studying natural living systems instead of technological artificial elements. Consequently, it points out interesting new directions towards the design of devices capable of measuring how mature is the fruit and vegetable, or to give an estimative of its life span for storage purposes.

12. IMPLEMENTATION OF THE FRACTIONAL POTENTIAL

The classical expressions for the electrical potential φ of a single charge, a dipole, a quadrupole, an infinite filament carrying a charge λ per unit length, two opposite charged filaments, and a planar surface with charge density σ reveal the relationship $\varphi \sim r^{-3}, r^{-2}, r^{-1}, \ln r, r$ (where r is the distance to the measuring point) corresponding to an integer-order differential relationship. Such state of affairs, motivated several authors to propose its generalization to fractional multipoles that produce a potential $\varphi \sim r^{-\alpha}, \alpha \in \Re$. Nevertheless, besides the abstract manipulation of mathematical expressions, the truth is that there is no practical method, and physical interpretation, for establishing the fractional potential [65].

We start by re-evaluating the potential produced at point (x,y) by a straight filament with finite length l and charge q:

$$\varphi = \frac{1}{4\pi\varepsilon_0}\frac{q}{l}\ln\left\{\frac{y+\frac{1}{2}l+\sqrt{x^2+\left(y+\frac{1}{2}l\right)^2}}{y-\frac{1}{2}l+\sqrt{x^2+\left(y-\frac{1}{2}l\right)^2}}\right\}+C \qquad (50)$$

It is well-known that for $x \to \infty$ we have $\varphi \to (q/4\pi\varepsilon_0)x^{-1}+C$ and, with $y = 0$, for $x \to 0$ we have $\varphi \to [q/(2\pi\varepsilon_0 l)]\ln(1/x)+C$. These limit cases correspond to a single charge and to an infinite filament.

We verify that expression (50) changes smoothly between the two limit cases. Therefore, we can have an intermediate fractional-order relationship as long as we restrict to a limited working range. This means that standard integer-order potential relationships have a global nature while fractional-order potentials have a local nature possible to capture only in a restricted region. This conclusion leads to an approximation scheme based on a recursive placement of integer-order functions.

In this line of thought, we developed a one-dimensional GA that places recursively n charges q_i ($i = 0, \ldots, (n-1)/2$,

n–odd; i = 1, …, n/2, n–even) at the symmetrical positions $\pm x_i$, with exception of $x_0 = 0$ that corresponds to the centre of the n-array of charges where there is a single charge q_0.

Our goal is to compare the desired reference potential $\varphi_{ref} = kx^{\alpha}$, with the approximate potential φ_{app}, resulting from a number n of charges q_i located at x_i, given by:

$$\begin{cases} \varphi_{app} = \dfrac{q_0}{|x|} + \displaystyle\sum_{i=1}^{\frac{n-1}{2}} \dfrac{q_i}{4\pi\varepsilon_0}\left(\dfrac{1}{|x-x_i|} + \dfrac{1}{|x+x_i|}\right), & n \text{ odd} \\ \varphi_{app} = \displaystyle\sum_{i=1}^{\frac{n}{2}} \dfrac{q_i}{4\pi\varepsilon_0}\left(\dfrac{1}{|x-x_i|} + \dfrac{1}{|x+x_i|}\right), & n \text{ even} \end{cases} \tag{51}$$

The experiments consist on executing the GA, for generating a combination of positions and charges that lead to an electrical potential with fractional slope similar to the desire reference potential. The values of GA parameters are: population number P = 40, crossover C(%) = 85.0%, mutation M(%) = 1.0%, elitist strategy ES(%) = 10.0% and a maximum number of generations G = 100. The optimization fitness function corresponds to the minimization of the error:

$$..J = \sum_{k=1}^{m} \left(\ln\left|\varphi_{app}/\varphi_{ref}\right|\right)^2, \quad \min_i(J), \quad i = 0,1,\ldots,n-1 \tag{52}$$

where m is the number of sampling points along the x-axis.

In the present case, we consider a log-log perspective, but its modification for a lin-lin case is straightforward.

For example, Fig. 65 shows φ_{app} for an approximation with n = 5 charges, when $\varphi_{ref} = 1.0x^{-1.5}$ and $0.2 < x < 0.8$.

After 32 iterations the GA leads to q_{0A} = –0.489 [volt], q_{1A} = 0.920 [volt] and q_{2A} = –0.077 [volt] (with scale factor $\times (4\pi\varepsilon_0)^{-1}$), at x_{0A} = 0.0 [m], $x_{1A} = \pm 0.147$ [m] and $x_{2A} = \pm 0.185$ [m], respectively.

The results show a good fit between the two functions. Executing the GA several times we verify that it is possible to find more than one 'good' solution. For a given application, a superior precision may be required and, in that case, a larger number of charges must be used. In this line of thought, we study the precision of this method for different number of charges, namely from n = 1 up to n = 10 charges.

Figure 65 depicts the minimum, maximum and average of J versus n, to achieve a valid solution for a statistical sample of 10 GA executions. This chart confirms that we have a better precision the larger the number of charges. Also, the results reveal the requirement of a larger number of iterations when the number of charges increases, and consequently a larger calculation time.

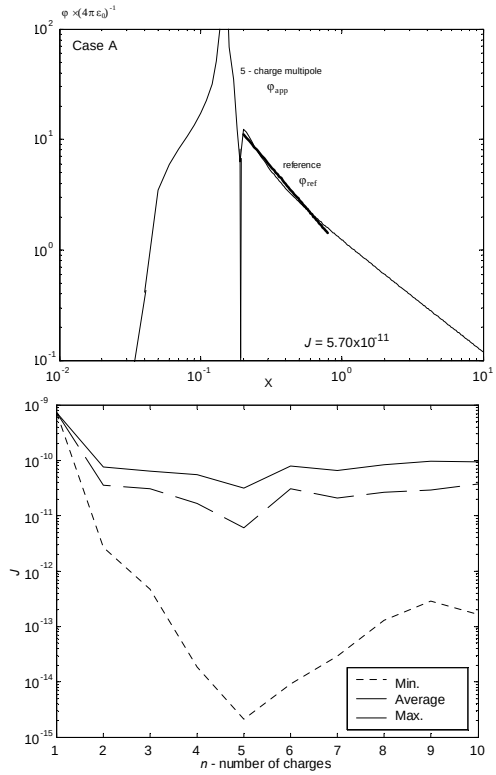

Fig. 65. Comparison of the electric potential φ_{app} and $\varphi_{ref} = 1.0x^{-1.5}$ [volt] *vs.* x for $0.2 < x < 0.8$ [m] and n = 5 and the corresponding approximation error J *vs.* number charges n.

We verify also that the position of the charges varies significantly with the number of charges used in the approximation. Therefore, pattern of the charge *versus* the location is not clear and its comparison with a fractal recursive layout is still under investigation.

13. STOCK PRICING DYNAMICS

In this section are studied daily records of international stock prices [66, 67] using the Fourier transform and the Pseudo Phase Plane (*PPP*). It is analysed the unpredictability based on the power law of the decay of the Fourier transform. Several examples show the evidence that the S&P 500 Stock market is a persistent process, with long-run memory effects.

13.1. Spectral Analysis of Market Indices

Several signals $x_i(t)$, $i \in \aleph$, ranging from 7910 trading-days in the same time period, were selected from the pool of the 500 biggest companies in US.

The Fourier transform is a mathematical tool [68] well adapted for analyzing the dynamics of the financial indices. The Fourier spectra $F\{x_i(t)\}$ reveal a power decay that can be approximated by:

$$|F\{x_i(t)\}| \approx c\ \omega^m,\ i \in \aleph,\ c,m \in \Re \tag{53}$$

Figures 66 and 67 show the time series for three cases, and the corresponding Fourier transform with the approximation formula (1) that characterizes the decay slope, respectively. Table 10 depicts the ticker of the financial index and the corresponding spectral slopes *m*.

In Fig. 67 are also displayed the values of R^2, the square of the correlation factor between $ln(\omega)$ and $ln|F\{x\}|$, that reflects the degree of statistical association of the pair of variables.

Figure 68 shows the relation between *m* and R^2, revealing that this association is almost functional.

Table 10. Characteristics of five financial indices

Ticker	*m*	dim_{PPP}	*d*
F0	–0.7790	1.463	1062
HPQ0	–0.8849	1.435	697
SUN0	–1.003	1.642	545
CTL0	–1.108	1.379	919
ECL0	–1.223	1.415	1043

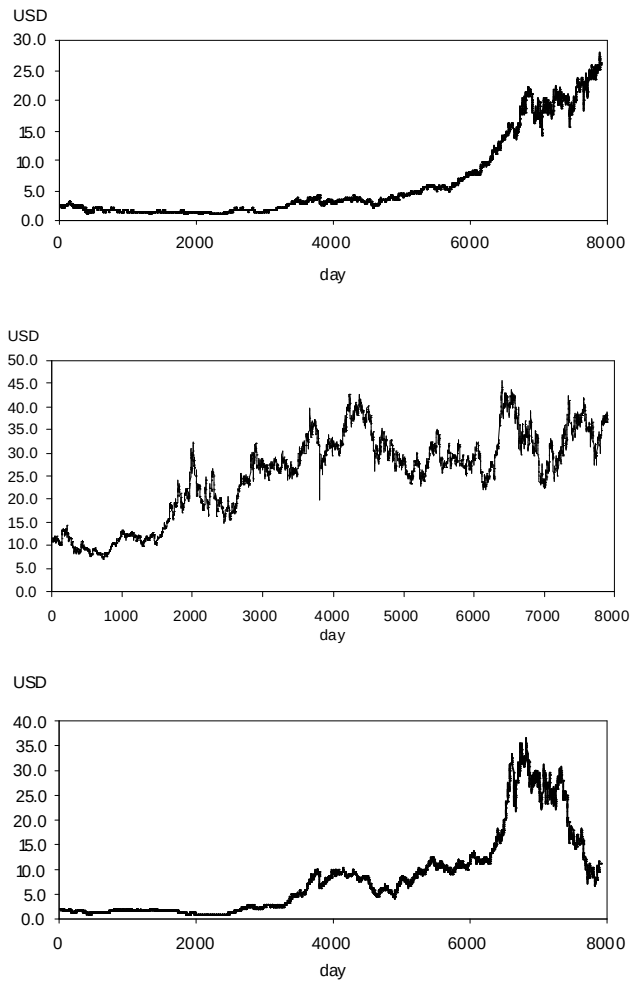

Fig. 66. Plots of the time series of the financial indices ECL0, SUN0 and F0

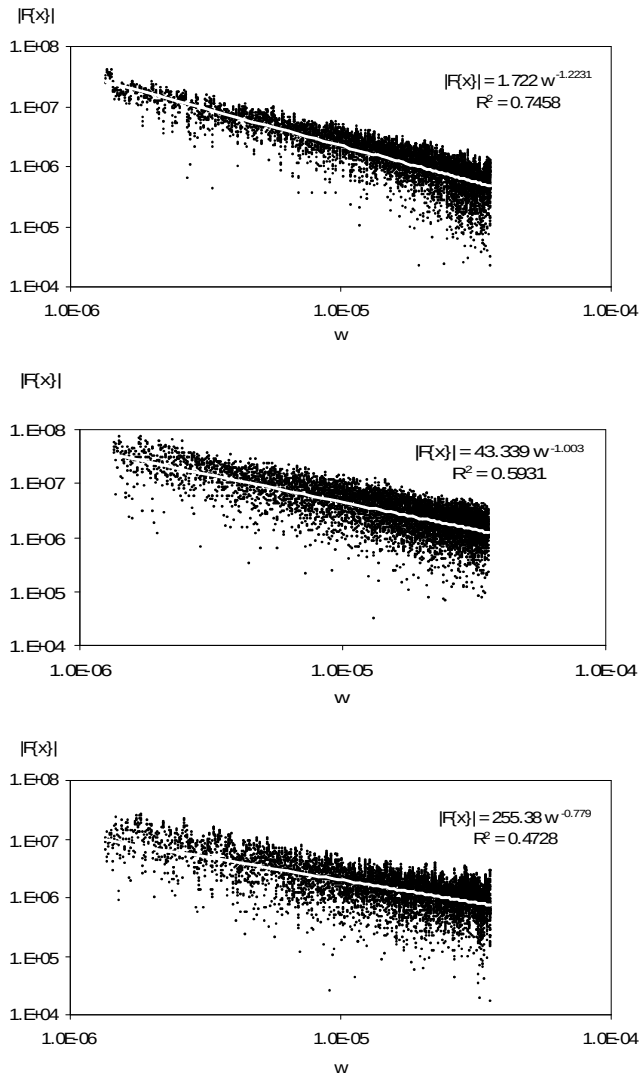

Fig. 67. Plots of the Fourier transform of the financial indices ECL0, SUN0 and F0

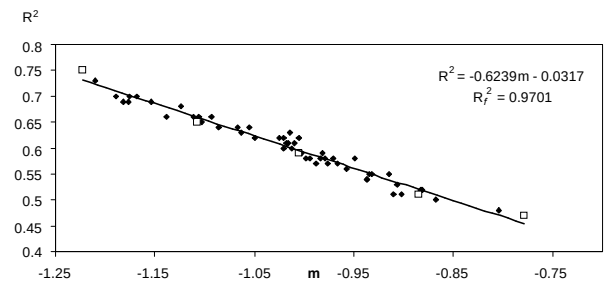

Fig. 68. Plot of the decay slope *m versus* the correlation coefficient R^2 of the previous charts of the Fourier transform for several financial indices. The square marks represent the position of the five specific tickers under study

13.2. Pseudo Phase Plane Analysis

The *PPP* is a tool that makes easier the study of the time series dynamics by its representation in a 2D space [69, 70]. Once a delay *d* is selected the *PPP* is a plot of the points:

$$P_d = \{(x_t, x_{t+d}) \in R^2 : t = 0,1,\cdots, N-d,\ 0 < d < N\} \qquad (54)$$

A process, based on information theory, to determine the delay d that provides the best candidate for periodicity was proposed by [70, 71]. Several experiments revealed that an alternative, but simpler, way for selecting the delay is based in detecting the first contrasting minimum in the autocorrelation function (*ACF*) witch can be defined by the expression:

$$ACF(d) = \sum_{t=d}^{n}(x_t - \bar{x})(x_{t+d} - \bar{x}) \Big/ \sum_{t=d}^{n}(x_t - \bar{x})^2 \qquad (55)$$

As a drawback, this equivalent process must be done with the user supervision because, sometimes, due to the noise embedded in some financial signals the first minimum proposed by the computer program is not sufficient clear, and therefore must be seen as a false minimum.

In Fig. 69 are plotted the *ACF*s of three signals showing the first contrasting minima. The resulting *PPP*s are also represented and their fractal dimension dim_{PPP} is calculated.

The results reveal that the delay d, required for the *PPP* representation, and the fractal dimension dim_{PPP} [72] have a minimum and a maximum, respectively, when $m = -1$. A preliminary analysis indicates that this behavior is related with the unpredictable of the time series and to the nature of phenomena similar to biased random walks. A deeper understanding of the fractional or integer value of d, the fractal characteristics of the *PPP* and the signal predictability needs to be further explored.

Table 10 suggests a relationship between m, dim_{PPP} and d. These characteristics are clearly depicted in Fig. 71.

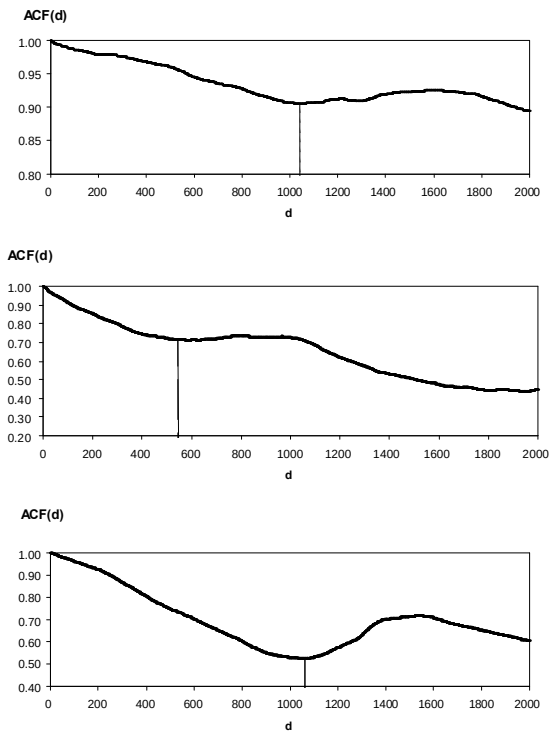

Fig. 69. Plots of the *ACF* for the financial indices ECL0, SUN0 and F0

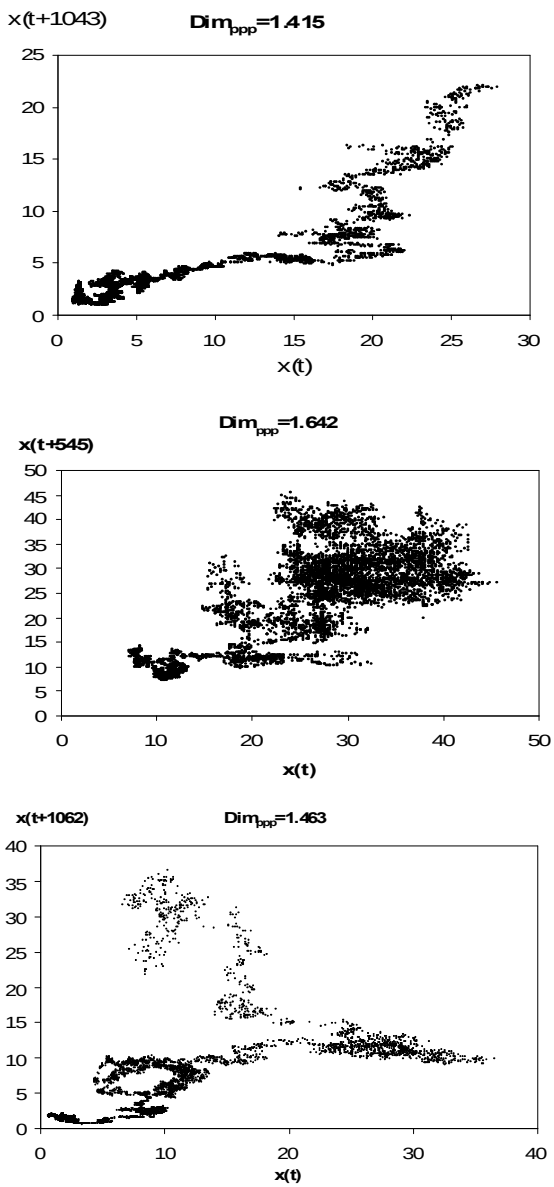

Fig. 70. Plot of the *PPP* for the financial indices ECL0, SUN0 and F0.

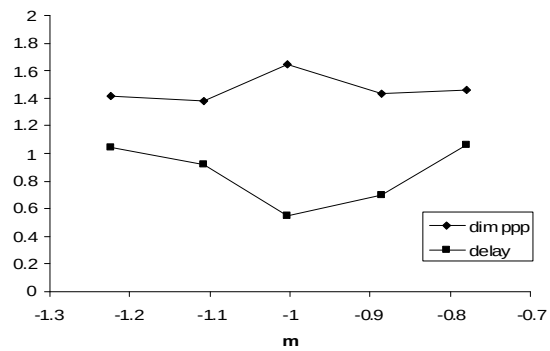

Fig. 71. Plots of dim_{PPP} and d *versus* m.

14. DYNAMICS IN A PARTICLE SWARM OPTIMIZATION ALGORITHM

This section studies the fractional dynamics during the evolution of a Particle Swarm Optimization (PSO) algorithm. Some swarm initial particles are randomly changed for stimulating the system response, and its effect is compared with a reference situation. The perturbation effect in the PSO evolution is observed in the perspective of the time behavior of the fitness of the best particle. The dynamics is investigated through the median of a sample of experiments, while adopting the Fourier analysis for describing the phenomena. The influence of the PSO parameters upon the global dynamics is also observed by performing several experiments for distinct values and parameters.

14.1. PSO Algorithm

The particle swarm optimization algorithm was proposed originally by Kennedy and Eberhart [73]. This optimization technique is inspired in the way swarms (*e.g.*, flocks of birds, schools of fishes, herds) elements move in a synchronized way as a defensive tactic. An analogy is established between a particle and an element of swarm. The particle movement is characterized by two vectors representing its current position x and velocity v (Fig. 72).

14.2. The optimization System

This section presents the problem used in the study of the *optimization* PSO dynamic system. The objective function consists on minimizing the Easom function (56) [74]. This function has two parameter and the optimum function is located at $f(x_1,x_2)|_{\text{opt}}$=-1.0. The variables consist in x_1, $x_2 \in [-100,100]$ and the algorithm uses real code to represent the swarm.

$$f(x_1,x_2) = -\cos(x_1)\cos(x_2)\,\mathrm{e}^{-(x_1-\pi)^2-(x_2-\pi)^2} \qquad (56)$$

A 50-population PSO is executed during 5000 generations under $\phi_1 = \phi_2 = 1.5$.

The influence of several factors can be analyzed in order to study the dynamics of the PSO [76], particularly the inertia factor I or the ϕ_i constants, $i = \{1, 2\}$. This effect can vary according to the type of population size, fitness function, and generation number used in the PSO. In this work, it is changed randomly one particle of the initial population. The influence of the inertia parameter is studied by performing tests for the values $I = \{0.4, 0.5, \ldots, 0.8\}$. The fitness evolution of the best global particle is taken as the output signal.

Initialize Swarm
repeat
  forall particles *do*
    Calculate fitness f
  end
  forall particles *do*
    $v_{t+1} = I\, v_t + \phi_1(b-x) + \phi_2(g-x)$
    $x_{t+1} = x_t + v_{t+1}$
  end
until stopping criteria

Fig. 72. Particle Swarm Optimization

14.3. The PSO Dynamics

The PSO system is stimulated by perturbing the initial population, namely by replacing one particle by a one new generated randomly. The corresponding swarm population fitness modification Δf is evaluated. The test condition remains unchanged during all the experiments. Therefore, the variation of the resulting PSO swarm fitness perturbation during the evolution can be viewed as the output signal that varies during the successive iterations. This analysis is evaluated using several experiments with different perturbation that replace the same particle in the population. All the other particles remain unchanged.

In this perspective, a perturbation input signal is created in the initial population when the replacement is performed. The output signal consists in the difference between the population fitness with and without the initial perturbation, that is $\Delta f(T) = f_{\text{pert}}(T) - \mathrm{f}(T)$.

Once having de Fourier description of the output signals it is possible to calculate the corresponding normalized transfer function (2) for particle replacement n_{r}.

$$H(\mathrm{j}w) = \frac{F\{\delta f_i(T)\}(\mathrm{j}w)}{F\{\delta p_{m\,i}(T)\}(\mathrm{j}w=0)} \qquad (57)$$

After repeating for all seeds a `representative' transfer function is obtained by using the median of the statistical sample [75] of n experiments for inertial term of I. In fig. 2 are depicted the transfer functions for $I = 0.4$ up to $I = 0.8$.

After repeating for all seeds a `representative' transfer function is obtained by using the median of the statistical sample [75] of n experiments (see Fig. 73). The medians of the transfer functions calculated previously (*i.e.*, for each real and imaginary part and for each frequency) are taken as the final part of the numerical transfer function $H(\mathrm{j}w)$.

Therefore, the median of the numerical system transfer functions, Fig. 73, is approximated by analytical expressions with gain $k = 1$, one pole $a \in \Re^+$ of fractional order $\alpha \in \Re^+$, and a time delay T, given by (58) (see Fig.74).

$$G_I(\mathrm{j}w) = \frac{k\,\mathrm{e}^{-T}}{\left(\dfrac{\mathrm{j}w}{a}+1\right)^{\alpha}} \qquad (58)$$

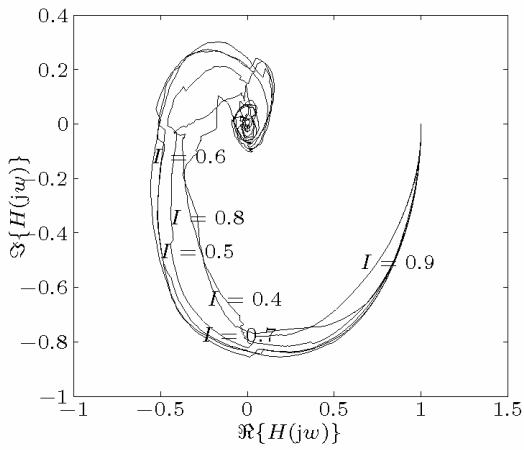

Fig. 73. Median transfer function $H(\mathrm{j}w)$, $n_{\mathrm{r}} = \{4,5,\ldots 8\}$

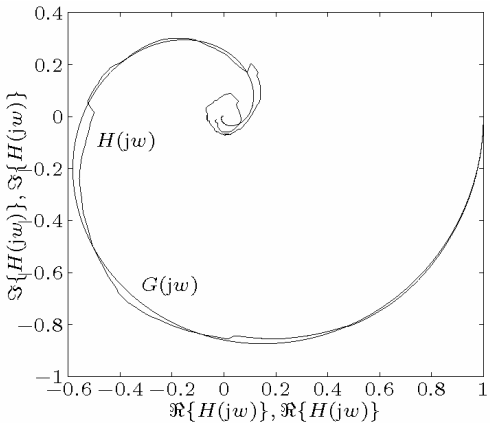

Fig. 74. Polar diagram for {*H*(j*w*), *G*(j*w*)}, *I* = 0.6

For evaluating the influence of the inertia parameter I are performed several simulations ranging from $I = 0.4$ up to $I = 0.8$. The parameters of $\{a, \alpha, T\}$ are depicted in Fig. 75.

The results reveal that the transfer function parameters $\{a, \alpha, T\}$ have some dependence with the inertia coefficient I. It can be observed that the parameters of transfer function have a maximum values at $I = 0.6$.

By enabling the zero/pole order to vary freely, we get non-integer values for α, while the adoption of an integer-order transfer function would lead to a larger number of zero/poles to get the same quality in the analytical fitting to the numerical values. The `requirement' of fractional-order models in opposition with the classical case of integer models is a well-known discussion and even nowadays final conclusions are not clear since it is always possible to approximate a fractional frequency response through an integer one as long as we make use of a larger number of zeros and poles. Nevertheless, in the present experiments there is a complementary point of view towards FC.

This section analyzed the signal propagation and the dynamic phenomena involved in the time evolution of a swarm. The study was established on the basis of the Easom function optimization. While PSO schemes have been extensively studied, the influence of perturbation signals over the operating conditions is not well known.

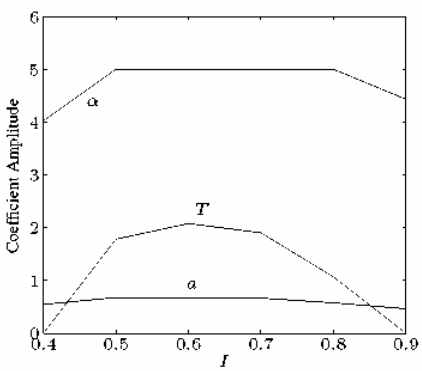

Fig. 75. Parameters (a, α, T) of G(jw)

Bearing these ideas in mind, the fractional calculus perspective calculus was introduced in order to develop simple, but comprehensive, approximating transfer functions of non-integer order.

15. CIRCUIT SYNTHESIS USING EVOLUTIONARY ALGORITHMS

In recent decades evolutionary computation (EC) techniques have been applied to the design of electronic circuits and systems, leading to a novel area of research called Evolutionary Electronics (EE) or Evolvable Hardware (EH). EE considers the concept for automatic design of electronic systems. Instead of using human conceived models, abstractions and techniques, EE employs search algorithms to develop implementations not achievable with the traditional design schemes, such as the Karnaugh or the Quine-McCluskey Boolean methods.

Several papers proposed designing combinational logic circuits using evolutionary algorithms and, in particular, genetic algorithms (GAs) [77, 78] and hybrid schemes such as the memetic algorithms (MAs) [79].

Particle swarm optimization (PSO) constitutes an alternative evolutionary computation technique, and this paper studies its application to combinational logic circuit synthesis. Bearing these ideas in mind, the organization of this section is as follows. Sub-section 15.1 presents a brief overview of the PSO. Sub-section 15.2 describes the PSO based circuit design, while sub-section 15.3 exhibits the simulation results.

15.1. Particle Swarm Optimization

In the literature about PSO the term 'swarm intelligence' appears rather often and, therefore, we begin by explaining why this is so.

Non-computer scientists (ornithologists, biologists and psychologists) did early research, which led into the theory of particle swarms. In these areas, the term 'swarm intelligence' is well known and characterizes the case when a large number of individuals are able of accomplish complex tasks. Motivated by these facts, some basic simulations of swarms were abstracted into the mathematical field. The usage of swarms for solving simple tasks in nature became an intriguing idea in algorithmic and function optimization.

Eberhart and Kennedy were the first to introduce the PSO algorithm [80], which is an optimization method inspired in the collective intelligence of swarms of biological populations, and was discovered through simplified social model simulation of bird flocking, fishing schooling and swarm theory.

In the PSO, instead of using genetic operators, as in the case of GAs, each particle (individual) adjusts its flying according with its own and its companions experiences. Each particle is treated as a point in a D-dimensional space and is manipulated as described below in the original PSO algorithm:

$$v_{id} = v_{id} + c_1 rand()(p_{id} - x_{id}) + c_2 Rand()(p_{gd} - x_{id}) \quad (59a)$$

$$x_{id} = x_{id} + v_{id} \quad (59b)$$

where c_1 and c_2 are positive constants, *rand*() and *Rand*() are two random functions in the range [0,1], $X_i = (x_{i1}, x_{i2},\ldots, x_{iD})$ represents the *i*th particle, $P_i = (p_{i1}, p_{i2},\ldots, p_{iD})$ is the best previous position (the position giving the best fitness value) of the particle, the symbol *g* represents the index of the best particle among all particles in the population, and $V_i = (v_{i1}, v_{i2},\ldots, v_{iD})$ is the rate of the position change (velocity) for particle *i*.

Expression (59) represents the flying trajectory of a population of particles. Equation (59a) describes how the velocity is dynamically updated and equation (59b) the position update of the "flying" particles. Equation (59a) is divided in three parts, namely the momentum, the cognitive and the social parts. In the first part the velocity cannot be changed abruptly: it is adjusted based on the current velocity. The second part represents the learning from its own flying experience. The third part consists on the learning group flying experience [81].

The first new parameter added into the original PSO algorithm is the inertia weigh. The dynamic equation of PSO with inertia weigh is modified to be:

$$\begin{aligned} v_{id} = w v_{id} &+ c_1 rand()(p_{id} - x_{id}) + \\ &+ c_2 Rand()(p_{gd} - x_{id}) \end{aligned} \quad (60a)$$

$$x_{id} = x_{id} + v_{id} \quad (60b)$$

where *w* constitutes the inertia weigh that introduces a balance between the global and the local search abilities. A large inertia weigh facilitates a global search while a small inertia weigh facilitates a local search.

Another parameter, called constriction coefficient *k*, is introduced with the hope that it can insure a PSO to converge. A simplified method of incorporating it appears in equation (61), where *k* is function of c_1 and c_2 as it is presented in equation (62).

$$v_{id} = k\begin{bmatrix} v_{id} + c_1 rand(\ )(p_{id} - x_{id}) + \\ + c_2 Rand()(p_{gd} - x_{id}) \end{bmatrix} \quad (61a)$$

$$x_{id} = x_{id} + v_{id} \quad (61b)$$

$$k = 2\left(2 - \phi - \sqrt{\phi^2 - 4\phi}\right)^{-1} \quad (62)$$

where $\phi = c_1 + c_2$, $\phi > 4$.

There are two different PSO topologies, namely the global version and the local version. In the global version of PSO, each particle flies through the search space with a velocity that is dynamically adjusted according to the particle's personal best performance achieved so far and the best performance achieved so far by all particles. On the other hand, in the local version of PSO, each particle's velocity is adjusted according to its personal best and the best performance achieved so far within its neighborhood. The neighborhood of each particle is generally defined as topologically nearest particles to the particle at each side.

PSO is an evolutionary algorithm simple in concept, easy to implement and computationally efficient. Figs. 76-78 present a generic EC algorithm, a hybrid algorithm, more precisely a MA and the original procedure for implementing the PSO algorithm, respectively.

The different versions of the PSO algorithms are: the real-value PSO, which is the original version of PSO and is well suited for solving real-value problems; the binary version of PSO, which is designed to solve binary problems; and the discrete version of PSO, which is good for solving the event-based problems. To extend the real-value version of PSO to binary/discrete space, the most critical part is to understand the meaning of concepts such as trajectory and velocity in the binary/discrete space.

Kennedy and Eberhart [80] use velocity as a probability to determine whether x_{id} (a bit) will be in one state or another (zero or one). The particle swarm formula of equation (59a) remains unchanged, except that now p_{id} and x_{id} are integers in [0.0,1.0] and a logistic transformation $S(v_{id})$ is used to accomplish this modification. The resulting change in position is defined by the following rule:

$$if\ \left[rand() < S(v_{id})\right] \quad then\ x_{id} = 1; \quad else\ x_{id} = 0 \quad (63)$$

where the function $S(v)$ is a sigmoid limiting transformation and *rand*() is a random number selected from a uniform distribution in the range [0.0,1.0].

1. Initialize the population
2. Calculate the fitness of each individual in the population
3. Reproduce selected individuals to form a new population
4. Perform evolutionary operations such as crossover and mutation on the population
5. Loop to step 2 until some condition is met

Fig. 76. Evolutionary computation algorithm

1. Initialize the population
2. Calculate the fitness of each individual in the population
3. Reproduce selected individuals to form a new population
4. Perform evolutionary operations such as crossover and mutation on the population
5. Apply a local search algorithm
5. Loop to step 2 until some condition is met

Fig. 77. Memetic algorithm

1. Initialize population in hyperspace
2. Evaluate fitness of individual particles
3. Modify velocities based on previous best and global (or neighborhood) best
4. Terminate on some condition
5. Go to step 2

Fig. 78. Particle swarm optimization process

15.2. PSO based circuit design

We adopt a PSO algorithm to design combinational logic circuits. A truth table specifies the circuits and the goal is to implement a functional circuit with the least possible complexity. Four sets of logic gates have been defined, as shown in Table 11, being *Gset 2* the simplest one (*i.e.*, a RISC-like set) and *Gset 6* the most complex gate set (*i.e.*, a CISC-like set). Logic gate named WIRE means a logical no-operation.

In the PSO scheme the circuits are encoded as a rectangular matrix **A** ($row \times column = r \times c$) of logic cells as represented in Fig. 79.

Three genes represent each cell: *<input1><input2><gate type>*, where *input1* and *input2* are one of the circuit inputs, if they are in the first column, or one of the previous outputs, if they are in other columns. The gate type is one of the elements adopted in the gate set. The chromosome is formed with as many triplets as the matrix size demands (*e.g.*, triplets = $3 \times r \times c$). For example, the chromosome that represents a 3×3 matrix is depicted in Fig. 80.

The initial population of circuits (particles) has a random generation. The initial velocity of each particle is initialized with zero. The following velocities are calculated applying equation (60a) and the new positions result from using equation (60b). In this way, each potential solution, called particle, flies through the problem space. For each gene is calculated the corresponding velocity. Therefore, the new positions are as many as the number of genes in the chromosome. If the new values of the input genes result out of range, then a re-insertion function is used. If the calculated gate gene is not allowed a new valid one is generated at random. These particles then have memory and each one keeps information of its previous best position (*pbest*) and its corresponding fitness. The swarm has the pbest of all the particles and the particle with the greatest fitness is called the global best (*gbest*).

Table 11. Gate sets.

Gate Set	Logic gates
Gset 2	{AND,XOR,WIRE}
Gset 3	{AND,OR,XOR,WIRE}
Gset 4	{AND,OR,XOR,NOT,WIRE}
Gset 6	{AND,OR,XOR,NOT,NAND,NOR,WIRE}

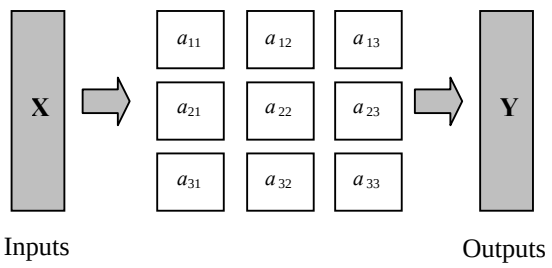

Fig. 79. A 3×3 matrix representing a circuit with input *X* and output *Y*

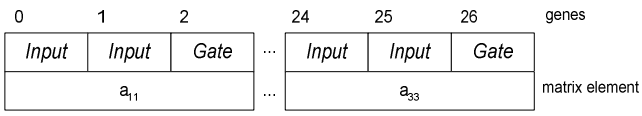

Fig. 80. Chromosome for the 3×3 matrix of Fig. 79

The basic concept of the PSO technique lies in accelerating each particle towards its *pbest* and *gbest* locations with a random weighted acceleration. However, in our case we also use a kind of mutation operator that introduces a new cell in 10% of the population. This mutation operator changes the characteristics of a given cell in the matrix. Therefore, the mutation modifies the gate type and the two inputs, meaning that a completely new cell can appear in the chromosome.

To run the PSO we have also to define the number P of individuals to create the initial population of particles. This population is always the same size across the generations, until reaching the solution.

The calculation of the fitness function F_s in (64) has two parts, f_1 and f_2, where f_1 measures the functionality and f_2 measures the simplicity. In a first phase, we compare the output Y produced by the PSO-generated circuit with the required values Y_R, according with the truth table, on a bit-per-bit basis. By other words, f_1 is incremented by one for each correct bit of the output until f_1 reaches the maximum value f_{10}, that occurs when we have a functional circuit. Once the circuit is functional, in a second phase, the algorithm tries to generate circuits with the least number of gates. This means that the resulting circuit must have as much genes *<gate type>* ≡ *<wire>* as possible. Therefore, the index f_2, that measures the simplicity (the number of null operations), is increased by *one* (*zero*) for each *wire* (*gate*) of the generated circuit, yielding:

$$f_{10} = 2^{ni} \times no \tag{64a}$$

$$f_1 = f_1 + 1 \text{ if } \{\text{bit } i \text{ of } \mathbf{Y}\} = \{\text{bit } i \text{ of } \mathbf{Y_R}\}, \quad i = 1, \ldots, f_{10} \tag{64b}$$

$$f_2 = f_2 + 1 \text{ if } gate\ type = wire \tag{64c}$$

$$F_s = \begin{cases} f_1, & F_s < f_{10} \\ f_1 + f_2, & F_s \geq f_{10} \end{cases} \tag{64d}$$

where *ni* and *no* represent the number of inputs and outputs of the circuit.

The concept of dynamic fitness function F_d results from an analogy between control systems and the GA case, where we master the population through the fitness function. The simplest control system is the proportional algorithm; nevertheless, there can be other control algorithms, such as, for example, the proportional and the differential scheme.

In this line of thought, expression (64) is a static fitness function F_s and corresponds to using a simple proportional algorithm. Therefore, to implement a proportional-derivative

evolution the fitness function needs a scheme of the type [82]:

$$F_d = F_s + KD^{\mu}[F_s] \tag{65}$$

where $0 \leq \mu \leq 1$ is the differential fractional-order and $K \in \Re$ is the 'gain' of the dynamical term.

15.3. Experiments and results

A reliable execution and analysis of an EC algorithm usually requires a large number of simulations to provide a reasonable assurance that the stochastic effects are properly considered. Therefore, in this study are developed n = 20 simulations for each case under analysis.

The experiments consist on running the three algorithms {GA, MA, PSO} to generate a typical combinational logic circuit, namely a 2-to-1 multiplexer (*M2-1*), a 1-bit full adder (*FA1*), a 4-bit parity checker (*PC4*) and a 2-bit multiplier (*MUL2*), using the fitness scheme described in (64) and (65). The circuits are generated with the gate sets presented in Table 11 and P = 3000, w = 0.5, c_1 = 1.5 and c_2 = 2.

Figure 81 depict the standard deviation of the number of generations to achieve the solution *S(N) versus* the average number of generations to achieve the solution *Av(N)* for the algorithms {GA, MA, PSO}, the circuits {*M2-1*, *FA1*, *PC4*, *MUL2*} and the gate sets {2, 3, 4, 6}. In these figure, we can see that the *MUL2* circuit is the most complex one, while the *PC4* and the *M2-1* are the simplest circuits. It is also possible to conclude that *Gset 6* is the less efficient gate set for all algorithms and circuits.

Figure 81 reveals that the plots follow a power law:

$$S(N) = a[Av(N)]^b \quad a, b \in \Re \tag{66}$$

Table 12 presents the numerical values of the parameters (a, b) for the three algorithms.

In terms of $S(N)$ *versus* $Av(N)$, the MA algorithm presents the best results for all circuits and gate sets. In what concerns the other two algorithms, the PSO is superior (inferior) to the GA for complex (simple) circuits.

Figure 82 depict the average processing time to obtain the solution $Av(PT)$ *versus* the average number of generations to achieve the solution $Av(N)$ for the algorithms {GA, MA, PSO}, the circuits {*M2-1, FA1, PC4, MUL2*} and the gate sets {2, 3, 4, 6}. When analysing these charts it is clear that the PSO algorithm demonstrates to be around ten times faster than the MA and the GA algorithms.

These plots follow also a power law:

$$Av(PT) = c[Av(N)]^d \quad c, d \in \Re \tag{67}$$

Table 12. The Parameters (a, b) and (c, d).

Algorithm	*a*	*b*	*c*	*d*
GA	0.0365	1.602	0.1526	1.1734
MA	0.0728	1.2602	0.2089	1.3587
PSO	0.2677	1.1528	0.0141	1.1233

Table 12 shows parameters (c, d) and we can see that the PSO algorithm has the best values.

Figures 83 and 84 depict the standard deviation of the number of generations to achieve the solution $S(N)$ and the average processing time to obtain the solution $Av(PT)$, respectively, *versus* the average number of generations to achieve the solution $Av(N)$ for the PSO algorithm using F_d, the circuits {*M2-1, FA1, PC4, MUL2*} and the gate sets {2, 3, 4, 6}. We conclude that F_d leads to better results in particular for the *MUL2* circuit and for the $Av(PT)$.

Figures 85 and 86 present a comparison between F_s and F_d.

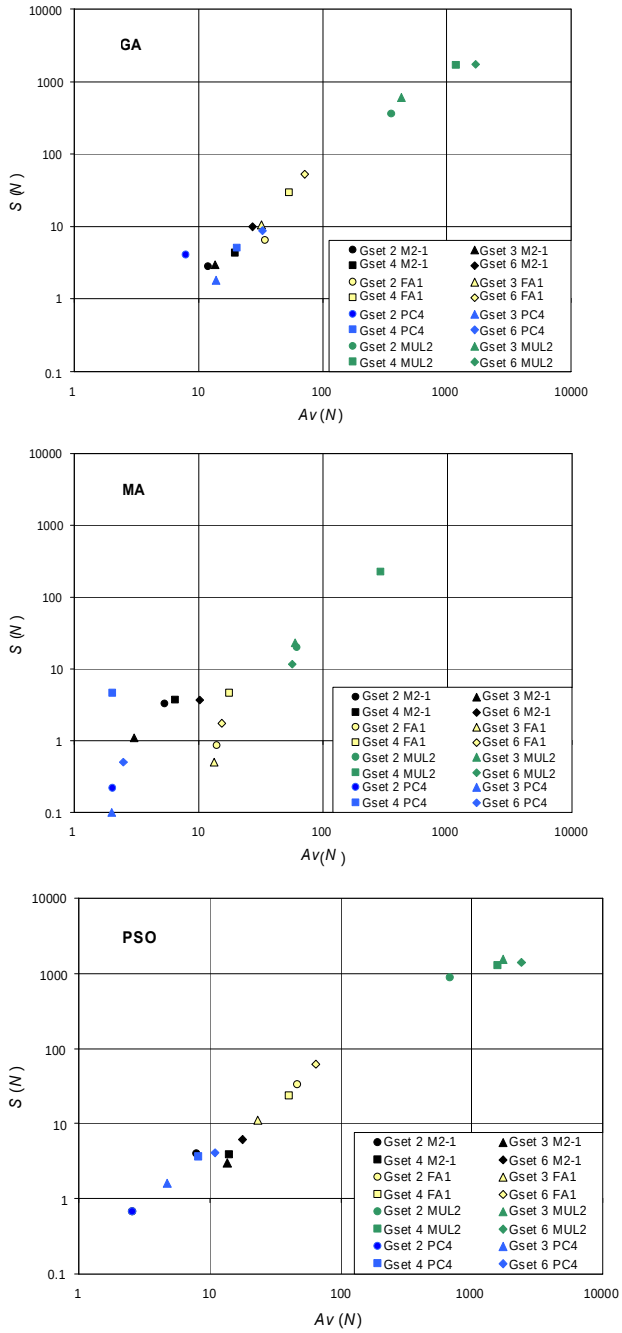

Fig. 81. $S(N)$ *versus* $Av(N)$ with P = 3000 and F_s for the GA, the MA and the PSO algorithms

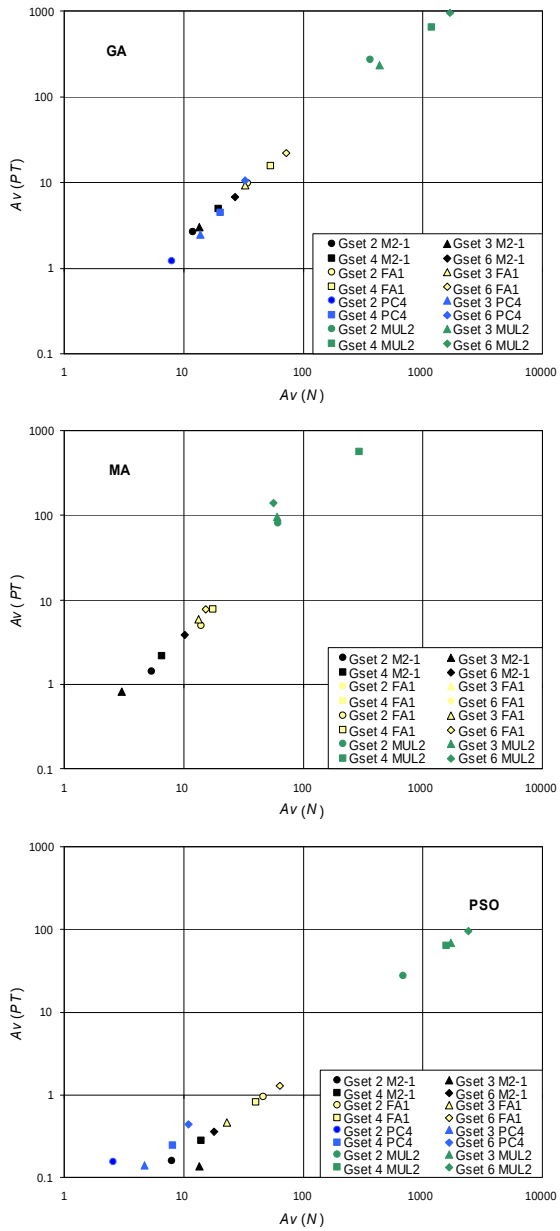

Fig. 82. ***Av*(*PT*) *versus Av*(*N*) with *P* = 3000 and F_s for the GA, the MA and the PSO algorithms**

In terms of *S*(*N*) *versus Av*(*N*) it is possible to say that the MA algorithm presents the best results. Nevertheless, when analysing Fig. 82, that shows *Av*(*PT*) *versus Av(N)* for reaching the solutions, we verify that the PSO algorithm is very efficient, in particular for the more complex circuits.

The PSO based algorithm for the design of combinational circuits follows the same profile as the other two evolutionary techniques presented in this paper.

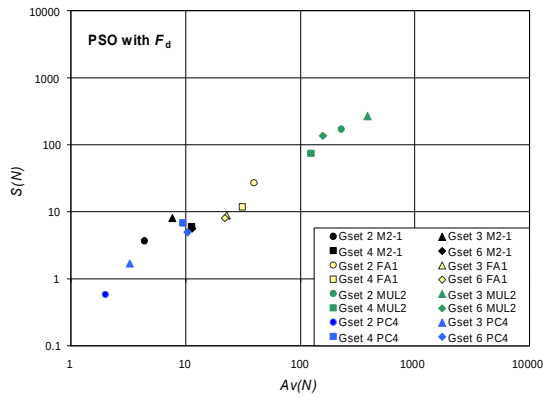

Fig. 83. ***S*(*N*) *versus Av*(*N*) for the PSO algorithm, *P* = 3000 and F_d**

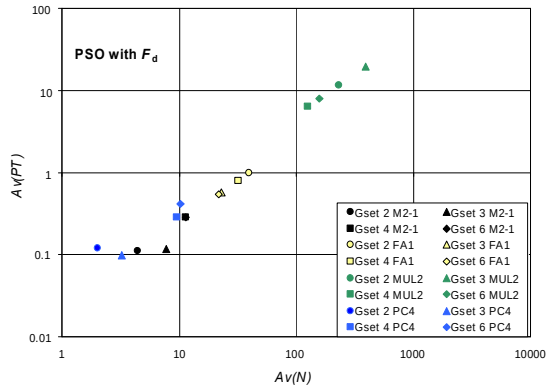

Fig. 84. ***Av*(*PT*) *versus Av*(*N*) for the GA, *P* = 3000 and F_d**

Adopting the study of the *S(N) versus Av(N)* for the three evolutionary algorithms, the MA algorithm presents better results over the GA and the PSO algorithms. However, in what concerns the processing time to achieve the solutions the PSO outcomes clearly the GA and the MA algorithms. Moreover, applying the F_d the results obtained are improved further in all gate sets and in particular for the more complex circuits.

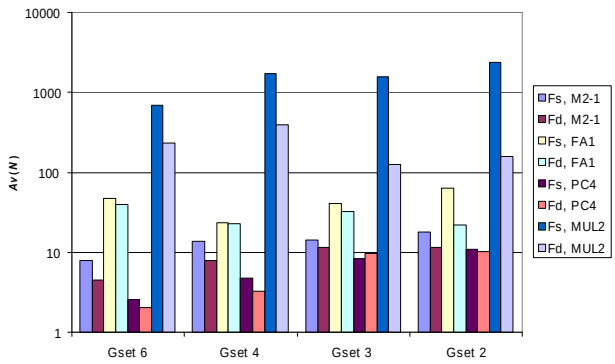

Fig. 85. ***Av*(*N*) for the PSO algorithm, *P* = 3000 using F_s and F_d**

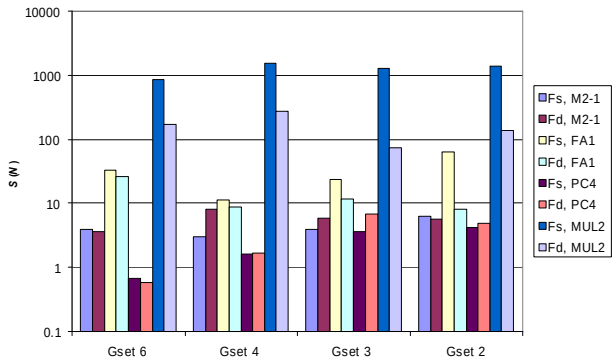

Fig. 86. $S(N)$ for the PSO algorithm, $P = 3000$ using F_s and F_d

16. CONCLUSIONS

We have presented several applications of the FC concepts. It was demonstrated the advantages of using the FC theory in different areas of science and engineering. In fact, this paper studied a variety of different physical systems, namely:

- tuning of PID controllers using fractional calculus concepts;
- fractional PD^{α} control of a hexapod robot;
- simulation and dynamical analysis of freeway traffic systems;
- fractional dynamics in the trajectory control of redundant manipulators;
- describing function of systems with nonlinear friction
- fractional order Fourier spectra in robotic manipulators with vibrations;
- position/force control of a robotic manipulator;
- position/force control of two arms working in cooperation;
- heat diffusion;
- electrical impedance of fruits;
- implementation of the fractional potential;
- stock pricing dynamics;
- dynamics in a particle swarm optimization algorithm;
- circuit synthesis using evolutionary algorithms.

The results demonstrate the importance of Fractional Calculus in the modeling and control of many systems and motivate for the development of new applications.

REFERENCES

[1] K. B. Oldham, J. Spanier, *The Fractional Calculus*, Academic Press, New York, 1974.

[2] K. S. Miller, B. Ross, *An Introduction to the Fractional Calculus and Fractional Differential Equations*, Wiley & Sons, New York, 1993.

[3] I. Podlubny, *Fractional Differential Equations*, Academic Press, San Diego, 1999.

[4] R. Hilfer, *Applications of Fractional Calculus in Physics*, World Scientific, Singapore, 2000.

[5] A. Oustaloup, *La Commande CRONE: Commande Robuste d'Ordre Non Entier*, Editions Hermès, Paris, 1991.

[6] A. Oustaloup, *La Dérivation Non Entière: Théorie, Synthèse et Applications*, Editions Hermès, Paris, 1995.

[7] R. S. Barbosa, J. A. T. Machado, and I. M. Ferreira, "PID Controller Tuning Using Fractional Calculus Concepts," FCAA-Journal of Fractional Calculus & Applied Analysis Vol. 7, No. 2, pp. 119-134, 2004.

[8] H. W. Bode, Network *Analysis and Feedback Amplifier Design*, Van Nostrand, New York, 1945.

[9] R. S. Barbosa, J. A. T. Machado, and I. M. Ferreira, "Tuning of PID Controllers Based On Bode's Ideal Transfer Function," Nonlinear Dynamics, Kluwer, Vol. 38, Nos. 1-4, pp. 305-321, December 2004.

[10] M. F. Silva, J. A. T. Machado, and A. M. Lopes, "Comparison of Fractional and Integer Order Control of an Hexapod Robot", Proceedings of the VIB 2003 – ASME Int. 19th Biennial Conference on Mechanical Vibration and Noise, USA, 2003.

[11] M. F. Silva, J. A. T. Machado, and I. S. Jesus, "Modelling and Simulation of Walking Robots With 3 dof Legs", Proceedings of the MIC 2006 – The 25th IASTED International Conference on Modelling, Identification and Control, pp. 271 – 276, Lanzarote, Spain, 2006.

[12] M. F. Silva, J. A. T. Machado, and A. M. Lopes, "Position / Force Control of a Walking Robot," MIROC – Machine Intelligence and Robot Control Vol. 5, pp. 33 – 44, 2003.

[13] M. F. Silva, J. A. T. Machado, "Fractional Order PDα Joint Control of Legged Robots," Journal of Vibration and Control – Special Issue on "Modeling and Control of Artificial Locomotion Systems" Vol. 12; No. 12; pp. 1483 – 1501, 2006.

[14] L. Figueiredo, J. Machado, and J. Ferreira, "Simulation and Dynamical Analysis of Freeway Traffic", Proceedings of the IEEE international Conference on Systems, Man and Cybernetics, pp. 3607-3612, Washington D.C., USA, 2003.

[15] L. Figueiredo, J. Machado, and J. Ferreira, "A System Approach to the Analysis of Traffic Dynamics", Proceedings of the IEEE International Conference on Networking, Sensing and Control, pp. 249-254, Taipei, Taiwan, 2004.

[16] J. F. Gabbard, *Car-Following Models*, Concise Encyclopedia of Traffic and Transportation Systems, M. Papageorgiou Ed., Pergamon Press, New York, 1991.

[17] L. Figueiredo, J. Machado, J. Ferreira, "Dynamical Analysis of Freeway Traffic," IEEE Transactions on Intelligent Transportation Systems Vol. 5, No. 4, ISSN: 1524-9050, pp. 259-266, 2004.

[18] J. A. Tenreiro Machado, "A probabilistic Interpretation of the Fractional-Order differentiation,"

FCAA - Journal of Fractional Calculus & Applied Analysis Vol. 6, No. 1, pp. 73-80, 2003.

[19] L. Figueiredo, J. T. Machado, "Dynamics of Freeway Traffic", Proceedings of the 8th IEEE Intelligent Transportation Systems Conference, Vienna, Austria, 2005.

[20] E. Sahin Conkur, and Rob Buckingham, "Clarifying the Definition of Redundancy as Used in Robotics," Robotica, Vol. 15, pp. 583-586, 1997.

[21] S. Chiaverini, "Singularity-Robust Task-Priority Redundancy Resolution for Real Time Kinematic Control of Robot Manipulators," IEEE Trans. Robotics Automation Vol. 13, pp. 398-410, 1997.

[22] C.A Klein, C. C Huang, "Review of Pseudoinverse Control for Use With Kinematically Redundant Manipulators," IEEE Trans. Syst. Man, Cyber, Vol. 13, pp. 245-250, 1983.

[23] T. Yoshikawa, *Foundations of Robotics: Analysis and Control*, MIT Press, 1988.

[24] R Rodney Roberts, Anthony Maciejewski, "Singularities, Stable Surfaces and Repeatable Behavior of Kinematically Redundant manipulators," International Journal of Robotics Research Vol. 13, pp. 70-81, 1994.

[25] John Bay, "Geometry and Prediction of Drift-free trajectories for Redundant Machines Under Pseudoinverse Control," International Journal of Robotics Research Vol. 11, pp. 41-52, 1992.

[26] Y. Nakamura, *Advanced Robotics: Redundancy and Optimization*, Addinson-Wesley, 1991.

[27] Keith L. Doty, C. Melchiorri and C. Bonivento, "A Theory of Generalized Inverses Applied to Robotics," International Journal of Robotics Research Vol. 12, pp. 1-19, 1993.

[28] Bruno Siciliano, "Kinematic Control of Redundant Robot Manipulators: A Tutorial," Journal of Intelligent and Robotic Systems Vol. 3, pp. 201-212, 1990.

[29] W.J.Chung, Y. Youm, and W. K. Chung, "Inverse Kinematics of Planar Redundant Manipulators via Virtual Links with Configuration Index," J. of Robotic Systems Vol. 11, pp. 117-128, 1994.

[30] Sanjeev Seereeram, John T. Wen, "A Global Approach to Path Planning for Redundant Manipulators," IEEE Trans. Robotics Automation, Vol. 11, pp. 152-159, 1995.

[31] Fernando Duarte, J. A. Tenreiro Machado, "Chaotic Phenomena and Fractional-Order Dynamics in the Trajectory Control of Redundant Manipulators," Nonlinear Dynamics, Kluwer, Vol. 29, Nos. 1-4, pp. 315-342, 2002.

[32] J. Tenreiro Machado, "Analysis and design of fractional-order digital control systems," SAMS - Journal Systems Analysis-Modelling-Simulation Vol. 27, pp. 107-122, 1997.

[33] J. Tenreiro Machado, "Discrete-Time Fractional-Order Controllers," FCAA J. of Fractional Calculus & Applied Analysis, Vol. 4, pp. 47–66, 2001.

[34] Maria da Graça Marcos, Fernando B. M. Duarte, and J. A. Tenreiro Machado, "Complex Dynamics in the Trajectory Control of Redundant Manipulators," Nonlinear Science and Complexity, World Scientific, pp. 134-143, 2007.

[35] B. Armstrong, B. Amin, "PID Control in the presence of Static Friction: A Comparison of Algebraic and Describing Function Analysis," Automatica Vol 32 , No. 5, pp. 679-692, 1996.

[36] D. A. Haessig, Jr., B. Friedland, "On the Modelling and Simulation of Friction," ASME Journal of Dynamic Systems, Measurement and Control Vol. 113, No. 3, pp. 354-362, 1991.

[37] D. Karnopp, "Computer Simulation of Stick-Slip Friction in Mechanical Dynamic Systems," ASME Journal of Dynamic System, Measurement and Control Vol. 107, No. 1, pp. 100-103, 1985.

[38] C. S. Cox, "Algorithms for Limit Cycle Prediction: A Tutorial Paper," Int. Journal of Electrical Eng Education Vol 24, No. 2, pp. 165-182, 1987.

[39] A. Azenha, J. T. Machado, "On the Describing Function Method and Prediction of Limit Cycles in Nonlinear Dynamical Systems," J. Syst. Analysis-Modelling-Simulation Vol. 33, pp. 307-320, 1998.

[40] R. Barbosa and J. T. Machado, "Describing Function Analysis of Systems with Impacts and Backlash," Nonlinear Dynamics Vol. 29, No 1-4, pp. 235–250, 2002.

[41] R. Barbosa, J. T. Machado and I. Ferreira, "Describing Function Analysis of Mechanical Systems with Nonlinear Friction and Backlash Phenomena", Proceedings of the 2nd IFAC Workshop on Lagrangian and Hamiltonian Methods for Non Linear Control, pp. 299-304, Sevilla, Spain, 2003.

[42] F. Duarte and J. T. Machado, "Describing Function Method in Nonlinear Friction", Proceedings of the IEEE, 1st International Conference on Electrical Engineering,, Coimbra, Portugal, 2005.

[43] F. Duarte, J. T. Machado, "Fractional Dynamics in the Describing Function Analysis of Nonlinear Friction", Proceedings of the 2nd IFAC Workshop on Fractional Differentiation and its Applications, Porto, Portugal, 2006.

[44] Miguel F. M Lima, J.A. Tenreiro Machado, and Manuel Crisóstomo, "Experimental Set-Up for Vibration and Impact Analysis in Robotics," WSEAS Trans. on Systems, Issue 5, Vol. 4, pp. 569-576, May 2005.

[45] Miguel F. M Lima, J.A. Tenreiro Machado, and Manuel Crisóstomo, "Fractional Order Fourier Spectra In Robotic Manipulators With Vibrations", Second IFAC Workshop on Fractional Differentiation and its Applications, Porto, Portugal, 2006.

[46] Oustaloup, Alain, Xavier Moreau, and Michel Nouillant, "From fractal robustness to non integer approach in vibration insulation: the CRONE suspension", Proceedings of the 36th Conference on Decision & Control, San Diego, California, USA, December 1997.

[47] M. H. Raibert, J. J. Craig, "Hybrid Position/Force Control of Manipulators, " ASME Journal of Dynamic Systems, Measurement, and Control Vol. 102, No. 2, pp. 126-133, 1981.

[48] N. Hogan, "Impedance control: An Approach to Manipulation, Parts I-Theory, II-Implementation, III-Applications," ASME J. of Dynamic Systems, Measurement and Control Vol. 107, No. 1, pp. 1 –24, 1985.

[49] O. Khatib, "A Unified Approach for Motion and Force Control of Robot Manipulators: The Operational Space Formulation," IEEE Journal of Robotics and Automation Vol. 3, No. 1, pp. 43-53, 1987.

[50] B. Siciliano, L. Villani, "A Force/Position Regulator for Robot Manipulators without Velocity Measurements," IEEE Int. Conf. on Robotics and Automation, USA, 1996.

[51] N. M. Fonseca Ferreira, J. A. Tenreiro Machado, "Fractional-Order Hybrid Control of Robotic Manipulator", 11th IEEE Int. Conf. on Advanced Robotics, Coimbra, Portugal, 2003.

[52] Y. C. Tsai, A. H Soni, "Accessible Region and Synthesis of Robot Arms," ASME J. Mech. Design Vol. 103, pp. 803–811,1981.

[53] T. Yoshikawa, "Manipulability of Robotic Mechanisms," The Int. J. Robotics Research Vol. 4, pp. 3-9, 1985.

[54] H. Asada, "A Geometrical Representation of Manipulator Dynamics and its Application to Arm Design," ASME J. Dynamic Syst. Meas., Contr. Vol. 105, pp. 131–142, 1983.

[55] J. A. T. Machado, A. M. Galhano, "A Statistical and Harmonic Model for Robot Manipulators", Proceedings of the IEEE Int. Conf. on Robotics and Automation, New Mexico, USA, 1997.

[56] Y. Nakamura, K. Nagai, and T. Yoshikawa, "Dynamics and Stability in Coordination of Multiple Robotic Mechanisms," Int. Journal of Robotics Research Vol. 8, pp. 44–61, 1989.

[57] N. M. Fonseca Ferreira, J. T. Machado, and J. Boaventura Cunha, "Fractional-Order Position/Force Robot Control", Proceedings of the 2nd IEEE Int. Conference on Computational Cybernetics, pp. 126-133, Vienna, Austria, 2004.

[58] R. Courant and D. Hilbert, *Methods of Mathematical Physics, Partial Differential Equations*, Wiley Interscience II, New York, 1962.

[59] J. T. Machado, Isabel Jesus, J. B. Cunha, and J. K. Tar, "Fractional Dynamics and Control of Distributed Parameter Systems," Intelligent Systems at the Service of Mankind Vol. 2, pp. 295-305, 2006.

[60] Isabel S. Jesus, Ramiro S. Barbosa, J. A. Tenreiro Machado, and J. Boaventura Cunha, "Strategies for the Control of Heat Diffusion Systems Based on Fractional Calculus", Proceedings of the IEEE Int. Conf. on Computational Cybernetics, Estonia, 2006.

[61] Evgenij Barsoukov, J. Ross Macdonald, *Impedance Spectroscopy, Theory, Experiment, and Applications*. John Wiley & Sons, Inc, 2005.

[62] I. S. Jesus, J. A. Tenreiro Machado, J. Boaventura Cunha, and Manuel F. Silva, "Fractional Order Electrical Impedance of Fruits and Vegetables", Proceedings of the 25th IASTED International Conference on Modeling, Identification and Control - MIC 2006,. Spain, February 2006.

[63] A. K. Jonscher, *Dielectric Relaxation in Solids*, Chelsea Dielectric Press, London, 1993.

[64] Samavati Hirad, Ali Hajimiri, Arvin R. Shahani, Gitty N. Nasserbakht, and Thomas H. Lee, "Fractal Capacitors,". IEEE Journal of Solid-State Circuits Vol. 33, No. 12, pp. 2035-2041, 1998.

[65] I. S. Jesus, J. A. T. Machado, and J. B. Cunha, "Application of Genetic Algorithms to the Implementation of Fractional Electromagnetic Potentials", Proceedings of the Fifth International Conference on Engineering Computational Technology - ECT 2006, Civil-Comp Press, Las Palmas de Gran Canaria, Spain; September 2006.

[66] E.E. Peters, *Chaos and Order in Capital Market: A new view of cycles, prices and market volatility*, Wiley Finance Editions New York, 1996.

[67] J. A. Ramirez, M. Cisneros, C. Ibarra-Valdez, and A. Soriano, "Multifractal Hurst analysis of crude oil prices", Physica A Vol. 313, No. 3, ,pp. 651-670, October 2002.

[68] H. P Szu, *Applied Fourier Analysis*, University of Evansville, Harcourt Brace Jovanovitch, Publishers, New York, 1984.

[69] L. S. Liebovitch, *Fractals and Chaos Simplified for the Life Sciences*, Oxford University Press, inc, 1998.

[70] B.F. Feeny, "Fractional Derivatives Applied to Phase Space Reconstruction," J. of Nonlinear Dynamics Vol. 38, Nos. 1-2, December 2004.

[71] L. Trendafilova and H. van Brussel, "Nonlinear Dynamics tools for the motion Analysis and condition monitoring of Robot Joints," J. Mech. Systems and Signal Processing Vol. 15, No. 6, pp. 1141-1164, November 2001.

[72] K. Falconer, *Fractal Geometry Mathematical Foundation and Applications*, John Wiley & Sons, 2003.

[73] J. Kennedy, R. C. Eberhart, "Particle Swarm Optimization", Proceedings of the 1995 IEEE International Conference on Neural Networks, volume 4, pp. 1942-1948, Perth, Australia, IEEE Service Center, Piscataway, NJ, 1995.

[74] F. V. den Bergh, A. P. Engelbrecht, "A Study of Particle Swarm Optimization Particle Trajectories," Inf. Sci. Vol. 176, No. 8, pp. 937-971, 2006.

[75] J. A. Tenreiro Machado, A. M. S. F. Galhano, "A Statistical Perspective to the Fourier Analysis of Mechanical Manipulators," Journal Systems Analysis-Modelling-Simulation Vol. 33, pp. 373-384, 1998.

[76] E. J. Solteiro Pires, J. A. Tenreiro Machado, and P. B. de Moura Oliveira, "Dynamical Modelling of a Genetic Algorithm," Signal Processing Vol. 86, No. 10, pp. 2760-2770, 2006.

[77] S. J. Louis, Rawlins, and G. J. Designer, "Genetic Algorithms: Genetic Algorithms in Structure Design", Proceedings. of the Fourth Int. Conference on Genetic Algorithms, 1991.

[78] D. E. Goldberg, *Genetic Algorithms in Search Optimization and Machine Learning*, Addison-Wesley, 1989.

[79] Cecília Reis, J. A. Tenreiro Machado, and J. Boaventura Cunha, "An Evolutionary Hybrid Approach in the Design of Combinational Digital Circuits," WSEAS Transactions on Systems Vol. 4, Issue 12, pp. 2338-2345, December 2005.

[80] J. Kennedy, R. C. Eberhart, "Particle Swarm Optimization", Proceedings of the IEEE International Conference Neural Networks, pp. 1942-1948, November 1995.

[81] Y. Shi, R. C. Eberhart, "A Modified Particle Swarm Optimizer," Proceedings of the 1998 International Conf. on Evolutionary Computation, pp. 69-73, May 1998.

[82] C. Reis, J. Machado, and J. Cunha, "Evolutionary Design of Combinational Circuits Using Fractional-Order Fitness", Proceedings of the Fith EUROMECH Nonlinear Dynamics Conference, pp. 1312–1321, 2005.